UCLouvain

École polytechnique de Louvain

Structural Strength Evaluation and Comparison of Laminated Ferromagnetic Pole Structures in Magnetic Gears, Using 3D-FEM

Authors : Guillaume **Topet**
Supervisors : Bruno **Dehez**
Readers : Issam **Doghri** ,Christophe **Degreef** and Virginie **Kluyskens**
Academic year 2018–2019
ingénieur civil électromécanicien
Master [120]

Abstract

Magnetic gears have experienced growing investigation by the scientific community for the recent decades. Indeed, the coaxial magnetic gears represent a serious alternative for the present conventional mechanical gears. The performances of coaxial magnetic gears, in term of torque density capability, has effectively reached the scale of the mechanical counterpart. Furthermore, they possess some additional features, that might be of great interest for several applications. Indeed, the torque transmission is now made possible using contactless rotors since the torque is now transmitted using magnetism laws.

In the actual state of the researches, many of the engineers that worked on magnetic gears mentioned the importance of the structural resistance of the ferromagnetic pole pieces. However, very few tried to bring an answer.

Acknowledgements

During this Master thesis, the capability of adapting the vision and the objectives in function of the research's advancements has been required all along this project. That surely is the one fundamental principle of research.

In the first place, I would like to thank my supervisor, Professor Bruno Dehez who's devotion and disponibility have been very helpful and motivating all along the thesis.

I can also give an important mention to his PhD. student Christophe Degreef and his associate Virginie Kluyskens, who were very disponible and who's advice's and work were also very helpful for the purpose of this thesis.

I am also very thankful for the Professor Issam Doghri and his Phd. student Colin Laville, who gave me key advises for the handling of the new objectives and the change of field of work.

I would like to thank the readers of my thesis, including my mother, my friends Laurent Bua and Nathan Coppin, my girlfriend Chloé Kenda, his father Benoît Kenda and his wife Florence Moureau.

I would like to give a general thank to all those who shared a part of my life during this thesis.

Finally, I would like to thank my family, especially my father and my mother for allowing me to access the University and all the opportunities that comes with it.

Contents

1 Introduction **5**
- 1.1 Magnetic gear's emergence and fundamental principles . . . 5
- 1.2 Magnetic gears, definition and main types . . . 7

2 State of the Art **10**
- 2.1 Coaxial Magnetic Gear, constitutive equations . . . 10
- 2.2 Space harmonic analysis, reduction factor and transmitted torque . . . 12
- 2.3 Magnetic leak, end-effect and iron losses . . . 14
- 2.4 Permanent magnets configurations . . . 18
  - 2.4.1 Halbach arrays . . . 19
  - 2.4.2 Consequent poles . . . 22
  - 2.4.3 Optimal Permanent Magnet Arrangement . . . 23
- 2.5 Modulating Ring . . . 25
  - 2.5.1 Pole-pieces shape factor . . . 25
  - 2.5.2 Stationary pole-pieces supporting structures . . . 27
- 2.6 State of the Art : conclusion . . . 29

3 Design **30**
- 3.1 Objectives and specifications . . . 30
- 3.2 Cinematic design . . . 32
  - 3.2.1 Held modulating ring("stator") . . . 33
  - 3.2.2 Held High-speed Rotor . . . 33
  - 3.2.3 Held Low-speed Rotor . . . 33
- 3.3 Morphological diagram, literature synthesis . . . 34
- 3.4 Conclusion and Objectives . . . 36

4 Theoretical approach **37**
- 4.1 Problem definition . . . 37
- 4.2 Hypothesis . . . 38
- 4.3 Simple and higher order lamination theory . . . 39
- 4.4 Magnetic gear parameters . . . 41
- 4.5 Ferromagnetic pole pieces parameters . . . 42
  - 4.5.1 Section properties . . . 43
  - 4.5.2 Material properties . . . 43
- 4.6 Maxwell Stress Tensor . . . 44

5 3D - Finite Element Method **47**
- 5.1 Model description . . . 47
  - 5.1.1 Boundary Conditions . . . 47
- 5.2 Contact surface . . . 48
  - 5.2.1 Master - slave interaction . . . 48
  - 5.2.2 Normal Behavior . . . 49
  - 5.2.3 Friction model(Tangential behavior) . . . 50
- 5.3 Force and contact interfaces distribution . . . 52
- 5.4 Resolution method . . . 54

6 Results **56**
6.1 Equivalent Spring stiffness . . . 56
6.2 Torsional twist, no-slip region and equivalent beam validation . . . 60
6.3 Stall region . . . 63
6.4 Transient region, stack influence . . . 64
6.5 Radial bending . . . 66
6.6 Tangential bending . . . 67
6.7 Optimization structures . . . 68
6.7.1 Torsional twist . . . 70
6.7.2 Radial distortion . . . 71
6.7.3 Tangential distortion . . . 72
6.7.4 Summary of the optimized structures . . . 72

7 Conclusion and further recommendations **73**
7.1 Results summary . . . 73
7.2 Limitations of the Results . . . 73
7.3 Recommendations . . . 74

A Comsol designs **79**

B Preliminary Abaqus designs **81**

C Equivalent Elastic Constants **83**

D Correction method **85**

1 Introduction

Since the recent decades, the interest concerning the magnetic gears, has been growing exponentially. Indeed, recent works showed that magnetic gear could achieve comparable torque transmission density as conventional mechanical gears. In fact, magnetic gears interested a few engineers for more than one century. The potential benefits of the magnetic gears were already well understood. Of course, the ability of performing contactless power transmission could represent in some applications, a considerable improvement. This one feature of magnetic gears allows according to [1] :

- Reduced acoustic noise and vibration
- No tooth wear
- Reduced/no maintenance
- Improved reliability
- Precise peak torque transmission capability
- Overload protection
- Physical Input and output isolation

In this thesis, the first objective was to design and implement a prototype of such a gear. The conception began with a simple specification of what is expected from the magnetic gear and how to achieve it. Following this, a design procedure as been started with the cinematic design. But, while still searching for new improvements path to bring to the magnetic gear, it has been found that the consistency of the researches concerning the structural rigidity of the modulating ring was poor. This was inlighted during the implementation of a morphological diagram confronting the different solutions of modulating ring configurations. This is why, before going deeper into the design process, it has been judged more profitable for the researches, to switch the direction of the present investigation to dedicate this thesis to the modulating ring structural rigidity.

Since it is a complicated structure, composed of laminated ferromagnetic materials and that the performance is greatly influenced by the air-gap length between the rotors, the implementation of this part of the gear, represents an important challenge. The structural evaluations have been implemented using 3D Finite Element Method(3D-FEM) by the means of Comsol^{TM}and Abaqus^{TM}.

1.1 Magnetic gear's emergence and fundamental principles

The first concept of a magnetic gear with the purpose of transmitting power, has been brought and patented by Charles G. Armstrong, in the early 20th century, with "The power transmitting device"[2]. The concept is illustrated in the figure (1). He gave in this letter, the basis of a new "gear-tool" generation. This device, instead of employing common mechanical teeth, with which the power transmission is insured by contact friction, would create a magnetomotive torque through the reluctance variation of the magnetic circuit[3], following the Hopkinson's law. One wheel, the "driven wheel", consisted of a simple ferromagnetic wheel

with a periodic disposition of teeth, to create a magnetic circuit, which would be closed, by a "driving wheel". The driving wheel would be made of electrified coils that provides the magnetic flux to the circuit, and then produces the torque coupling between the two wheels. The coils/reluctance system will be later changed to the profit of permanent magnets(PM), for the sake of simplicity and to withdraw the Joule losses present in the coils[4].

In the magnetic circuit theory, the expression of the magnetomotive force follows the Hopkinson's analogy, which involves the the magnetic flux ϕ and reluctance R.

Hopkinson's analogy :

$$\mathcal{F} = \mathcal{R} \cdot \phi \tag{1}$$

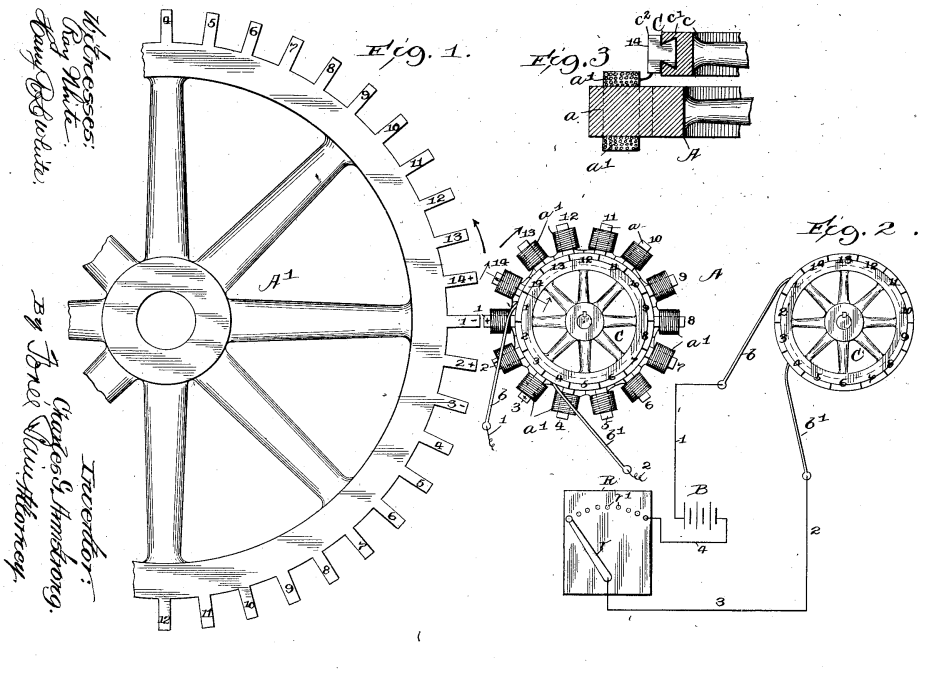

Figure 1: "The power transmitting device", Charles G. Armstrong, 1901

The first fully permanent magnet(PM) mounted gearing machine appeared nearly 40 years latter. The improved machine was the work of the U.S inventor H.T Faus[4]. The patent claims the first implementation of a PM magnetic gear with diverse topologies.

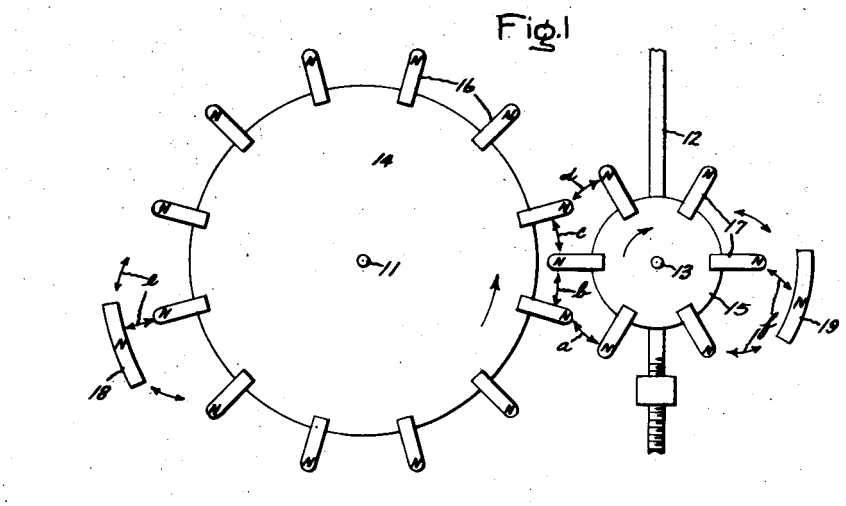

Figure 2: "The magnet gearing" employing permanent magnets, H.T Faus, 1941

Later in the 80's, improved versions of the magnetic gear were released, employing ferrite magnets, with much better utilization of the magnetic circuit[5]. Nevertheless, the magnetic gears were, till recent decades, with very few topology configurations, mostly spur gears and external gears. Which are actually converted conventional mechanical gears into magnetic gears. These configurations had a very bad exploitation of the magnetic circuit, with a little portion of the magnetic flux used at the same moment. The rest of the flux being interfering with the main flux. This results with very weak torque density ($< 5[kNm/m^3]$), and poor efficiency (less than 35%)[6].

We can draw the ascertainment, that despite all the potential improvements proposed by this new device, until the last few decades, the investigations and the interest over the magnetic gears had been very modest.

The interest has been revived in 2001, by the innovating paper proposed by K. Atallah and D. Howe[1], in which they present a new " flux-modulating topology magnetic gear", employing two concentric permanent magnet stages and an intermediate ferromagnetic ring, composed with teeth segments. The low reluctance ferromagnetic teeth, also called pole-pieces or modulating ring, acts as a guiding track for the magnetic flux in order to modulate the magnetic space harmonics emanating from both permanent magnet rotors. The modulated magnetic flux can further meet up on the same fundamental harmonic and generate reluctant torque. These variations raised the torque density to more then $40[kNm/m^3]$ with an efficiency of more than 95%. This made the magnetic gear, a potential reasonable and competitive alternative for the actual mechanical gear.

1.2 Magnetic gears, definition and main types

Before going deeper into the explanation of the actual diversity of topology/technology employed for the magnetic gears, let us just give a simple definition, inspired from the first important discoveries, of what a magnetic gear is. The definition will encompass all the possible machines that would match it's definition.

A magnetic gear is a device that uses magnetic coupling trough permanent magnets or electrified coils, to reproduce the same action as conventional mechanical gears. By means, they transmit mechanical power through rotation/translation of a prime mover in order to move a secondary mover. The purpose being to operate a reduction of the torque/speed between the two movers. They are two main families of magnetic gears, converted magnetic gears[2], and flux modulating magnetic gear [1].

The flux modulating magnetic gears contain already several sub-branches of configurations that are depicted in figure 3, following the classification made by P.M. Tlali, R-J. Wang and S. Gerber[7]. This classification includes Coaxial Magnetic Gears(CMG), that implies radial magnetic flux. Axial magnetic gears involves as the name suggests axial magnetic field. Finally linear magnetic gears involve a longitudinal distribution of the field and transmit torque through a translative motion. The focus will be kept on the coaxial magnetic gears in this thesis. The two other configurations, even though they might be relevant in some applications, won't be considered.

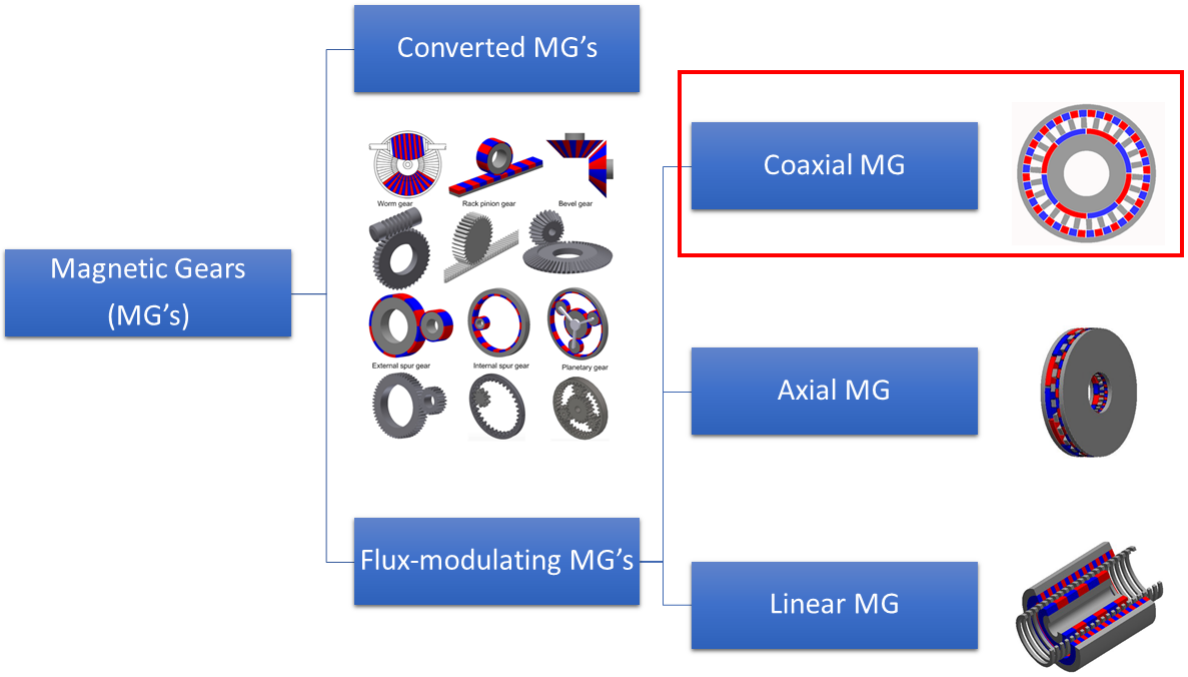

Figure 3: Magnetic Gears types. In red, the CMG. Inspired from [8]

As defined previously, the CMG is a radially coupled magnetic gear that consists in a superposition of 3 cylinders that are rotating on the same axis. Both the inner and outer rotors are mounted with periodically alternated permanent magnets. The PM's will create a number of magnetic pole pairs. The alternated field from outer and inner rotor allows the magnetic linkage between both rotors, depending on the harmonic space. The mediator between the inner and outer rotors, also commonly called "stator" (even if it can actually, in some configurations, act as a rotor instead of the inner/outer cylinders) is composed of a number of ferromagnetic pole-pieces. Those pole-pieces will operate a modulation of the

outer/inner magnetic field with the purpose to change the space harmonic of each fields in order to match the inner/outer magnetic field. Which in turn creates the coupling force.

2 State of the Art

The creation of the new configuration, brought in 2001[1], gave a glimpse of a potential new gear, that in time might be marketable to an industrial-scale. This new magnetic gear as been gradually more investigated[7]. New improvements have been added to the initial CMG, and the following chapter will try to evaluate those new improvements by the analysis of the actual publications, in order to define a new path of improvement for the futur researches.

2.1 Coaxial Magnetic Gear, constitutive equations

The fundamental operation of the coaxial magnetic gear, is the magnetic coupling between the inner and the outer rotor, employing the space harmonic modulation of the magnetic field. With the same number of magnetic poles and without any intervention of the modulating ring, the gear would have a reduction factor of $G_r = \frac{\Omega_o}{\Omega_i}$ equal to 1. The origin of the variation of the reduction factor comes from inequal number of outer and inner pair of poles and the modulation of the magnetic field by the ferromagnetic alternated poles at the stator. This can be understood by an analysis of the space harmonic of the magnetic flux density distribution coming from one of the PM rotor through the modulating ring [1].

The radial and tangential flux density distributions, as well as the modulating action of the ferromagnetic teeth, for a coaxial magnetic gear, is shown in the paper by K.Atallah and D.Howe[1],and is expressed as follow :

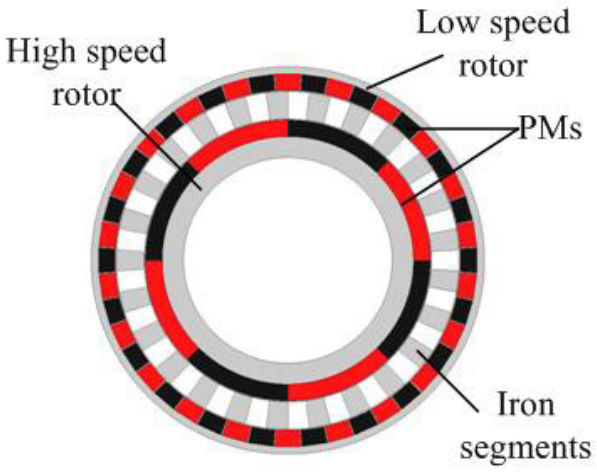

Figure 4: Coaxial Magnetic gear as proposed in [1]

$$B_r(r,\theta) = \underbrace{\Big(\sum_{m=1,3,5} b_{rm}(r)\, \cos\big(mp(\theta-\omega_r t) + mp\theta_0\big) \Big)}_{\text{flux density without ferromagnetic pole-pieces}} \times \underbrace{\Big(\lambda_{ro}(r) + \sum_{j=1,2,3,..} \lambda_{rj}(r)\, cos(jn_s(\theta-\Omega_s t\Big)}_{\text{modulation function}} \quad (2)$$

$$B_\theta(r,\theta) = \underbrace{\Big(\sum_{m=1,3,5} b_{\theta m}(r)\, \sin\big(mp(\theta-\omega_r t) + mp\theta_0\big) \Big)}_{\text{flux density without ferromagnetic pole-pieces}} \times \underbrace{\Big(\lambda_{\theta o}(r) + \sum_{j=1,2,3,..} \lambda_{\theta j}(r)\, cos(jn_s(\theta-\Omega_s t\Big)}_{\text{modulation function}} \quad (3)$$

with the following parameters :

- p and n_s, the number of paire of pôle at one of the PM rotor(either inner or outer) and the steel pole pieces.
- Ω_r and Ω_s, the angulaire speed of one of the PM rotor and the steel pole pieces.
- $b_{rm}\, b_{\theta m}$ and $\lambda_{rj}\, \lambda_{\theta j}$, the Fourrier coefficients of the flux distribution and the modulation function associated to the radial and tangential components.

From 2.1 and 2.1, the developed forms of the magnetic fields density distribution are obtained.

$$\begin{aligned} B_r(r,\theta) &= \lambda_{r0} \sum_{m=1,3,5} b_{rm}\, \cos\left(mp(\theta-\Omega_r t) + mp\theta_0\right) \\ &+\frac{1}{2} \sum_{m=1,3,5} \sum_{j=1,2,3} \lambda_{jr}(r)\, b_{rm}(r)\, cos\Big((mp+jn_s)\Big(\theta - \frac{(mp\Omega_r + jn_s\Omega_s)}{(mp+jn_s)}t\Big) + mp\theta_0\Big) \\ &+\frac{1}{2} \sum_{m=1,3,5} \sum_{j=1,2,3} \lambda_{jr}(r)\, b_{rm}(r)\, cos\Big((mp-jn_s)\Big(\theta - \frac{(mp\Omega_r - jn_s\Omega_s)}{(mp-jn_s)}t\Big) + mp\theta_0\Big) \end{aligned} \quad (4)$$

$$\begin{aligned} B_\theta(r,\theta) &= \lambda_{\theta 0} \sum_{m=1,3,5} b_{\theta m}\, \cos\left(mp(\theta-\Omega_r t) + mp\theta_0\right) \\ &+\frac{1}{2} \sum_{m=1,3,5} \sum_{j=1,2,3} \lambda_{j\theta}(r)\, b_{\theta m}(r)\, cos\Big((mp+jn_s)\Big(\theta - \frac{(mp\Omega_r + jn_s\Omega_s)}{(mp+jn_s)}t\Big) + mp\theta_0\Big) \\ &+\frac{1}{2} \sum_{m=1,3,5} \sum_{j=1,2,3} \lambda_{j\theta}(r)\, b_{\theta m}(r)\, cos\Big((mp-jn_s)\Big(\theta - \frac{(mp\Omega_r - jn_s\Omega_s)}{(mp-jn_s)}t\Big) + mp\theta_0\Big) \end{aligned} \quad (5)$$

The number of pair of pole from the space harmonic flux density distribution produced by either PM rotor, with the influence of the modulating stator, is given by:

$$p_{m,k} = |mp + kn_s| m = 1,3,5,...,\infty k = 0,\pm1,\pm2,\pm3,...,\pm\infty \quad (6)$$

The angular velocity of the flux density space harmonic is given by

$$\Omega_{m,k} = \frac{mp}{mp + kn_s}\Omega_r + \frac{kn_s}{mp + kn_s}\Omega_s \tag{7}$$

As predicted, it can be seen from the last equation, that the angular velocity of the space harmonic is different from the angular velocity of the rotor with the introduction of the ferromagnetic pôle-pieces($k \neq 0$).

The combination m = 1,k = -1, gives the highest asynchronous space harmonic[6]. Thus, when p corresponds to the number of magnetic pole-pair of the inner rotor($p = p_{hs}$), the number of pole-pairs of the outer(low-speed) PM rotor, must follow the relationship :

$$p_{ls} = n_s - p_{hs} \tag{8}$$

In the stationary pole-pieces mode ($\Omega_s = 0$), the Gear Ratio is then given by :

$$\boxed{\mathrm{G}_r = \frac{n_s - p_{hs}}{p_{hs}} = \frac{p_{ls}}{p_{hs}}} \tag{9}$$

In the mode where it is the PM rotor that is maintained stationary($\Omega_r = 0$), the gear ratio becomes :

$$\boxed{\mathrm{G}_r = \frac{n_s}{p} = \frac{n_s}{p_{hs}}} \tag{10}$$

As mentioned in the article[1], the rotating permanent magnet mode, might be the preferred mode of operation, since it simplifies the overall mechanical design. It is in accordance with many other papers who preferred the rotating permanent magnets mode instead of the rotating modulating ring. Furthermore, they already paid attention to the complexity of the structural design of the pole-pieces and the importance accorded to the stiffness of the modulating ring. Indeed, they represent the magnetic ground, and bare on themselves the sum of both torques of the low speed and high-speed rotors[6].
As in several other articles, the matter accorded to the strength of the pole-pieces structure is described as "A key importance towards industry use"[9].

As mentioned before, the stiffness of the pole-pieces structure under the effort of the electromagnetic torque, will be the main subject aborded in this thesis.

2.2 Space harmonic analysis, reduction factor and transmitted torque

In the first study of what is believed to be first the coaxial magnetic gear, three different gear ratios(resp. $G_r = 5.5\,, 5.75\,, 11$) have been numerically tested[6]. Those gear ratios have been selected following the rules of the modulated magnetic field distribution as explained above. The three corresponding configurations were then :

- $G_r = 5.5/1 : \quad p_h = 4; p_l = 22; n_s = 23$
- $G_r = 5.75/1 : \quad p_h = 4; p_l = 23; n_s = 27$
- $G_r = 11/1 : \quad p_h = 2; p_l = 22; n_s = 24$

The importance of finding the appropriate number of PM pair of poles and ferromagnetic poles, beyond the objective of coupling the magnetic flux of either low-speed and high-speed rotors, is to optimize the transmissible torque and to minimize the interaction between the ferromagnetic pole-pieces and the PM rotors, that creates parasites harmonics that will induce losses and asynchronous torques(i.e cogging torque, ripple)[6]. In the objective of finding the best combination, the modulated space harmonic spectra is computed as well as the torque transmission and the torque ripple. The below figures show results from[1] :

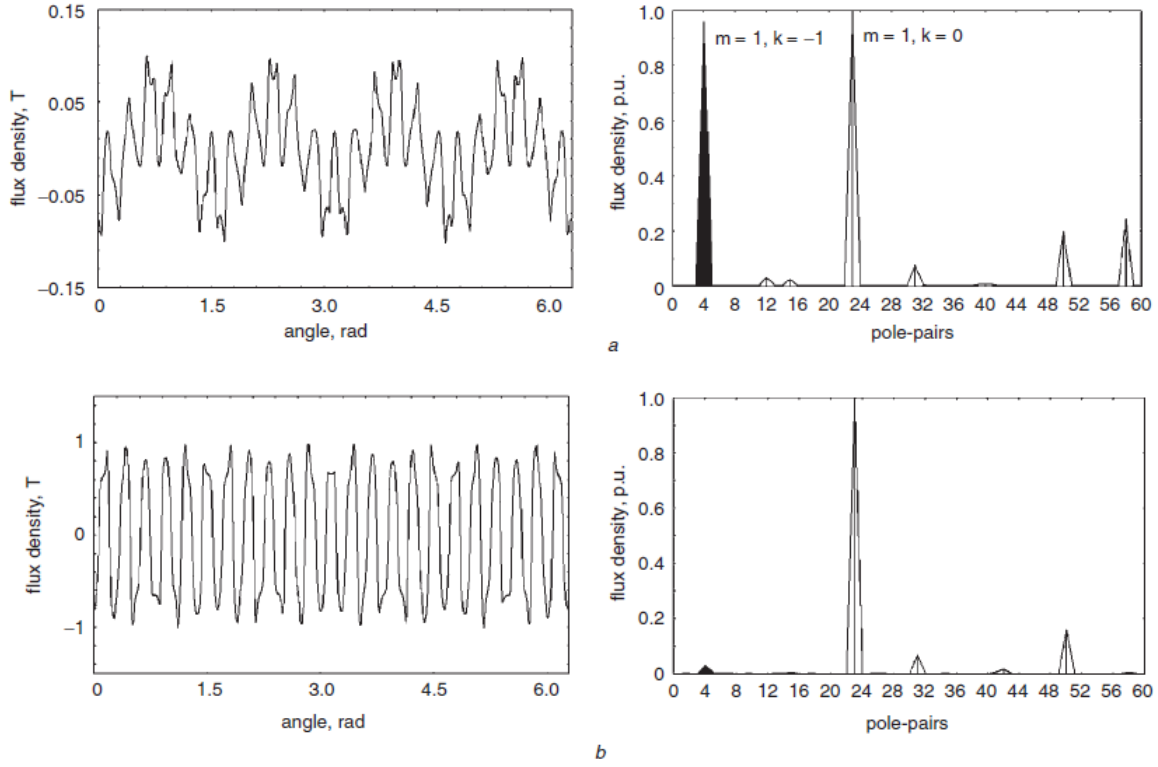

Figure 5: Radial flux wave-forms and their spectra due to the low-speed rotor magnetic field. $G_r = 5.75 : 1$, with and without modulating ring ($k = 1, 0$). a) in the air-gap adjacent to high-speed rotor, b) in the air-gap adjacent to low-speed rotor.[6]

In fig.5, the action of the modulator on the magnetic field distribution is shown in black. The main harmonic space of the low-speed rotor(resp. $p_l = 24$), as been modulated and now match the space harmonic of the high-speed rotor(resp. $p_h = 4$).

The harmonic content is responsible for the torque transmission. A wide panel of harmonics will induce a large ripple as shown in fig. (6) for $G_r = 11 : 1$,$5.5 : 1$ and 5.75 . This causes the overall performance of the magnetic gear to drop, in addition of compromising it's structural integrity. Also, the results in fig.6 and 7, reveal that besides of having a high torque transmission, the 5:75 gear ratio can procure a virtual "ripple-free" torque transmission. Finally, the maximum mean torque transmission is obtained for $G_r = 5.5$.[6]

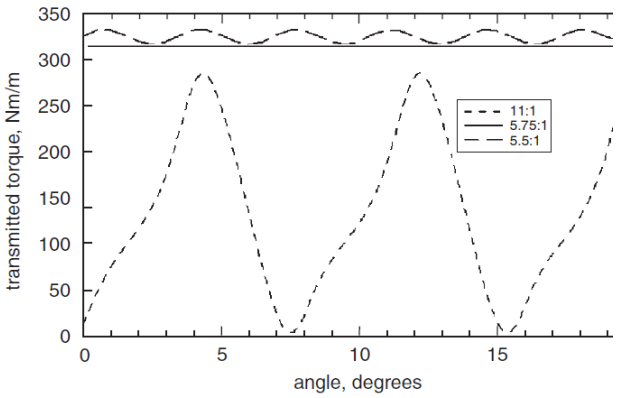

Figure 6: Transmitted torque along the angular variation of the high-speed rotor.[6]

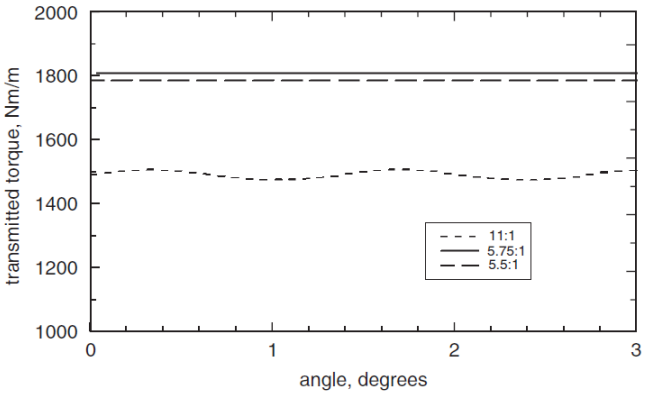

Figure 7: torque along the angular variation of the low-speed rotor.[6]

2.3 Magnetic leak, end-effect and iron losses

One key point when it comes to the magnetic gear mechanical conception, is the optimization of the employment of the magnetic flux. In case of bad configurations, the magnetic flux may leak outside of the magnetic circuit. This, results into the decrease of the torque density capability of the MG. The magnetic spur gear(cfr. fig.(3)) is a perfect example to illustrate the phenomena, for which only around 30% of the generated magnetic flux is used in the flux linkage at the same time[1]. The coaxial magnetic gear, and flux-modulating gears in general are a good solution for this problem[7]. However, as for converted magnetic gears, the coaxial magnetic gear is a subject to the end-effect and iron losses, which can drastically decrease the performances of the system if not handled properly[8].

In order to evaluate the end-effect, 3D-FEM must be implemented since the axial component of the magnetic flux density(B_z) is not represented in 2D-FEM. The leakage occurs when instead of penetrating the modulating pole pieces and going from the high-speed rotor magnets to the low-speed rotor magnets(and vice versa), the magnetic fields leaks outside the circuit to fall back inside the high-speed rotor yoke, or the supporting structure. As shown in fig.(8-9), the leaks are circled in black. We can also notice the modulating ring that is fixed on the supporting structure in fig.(8).

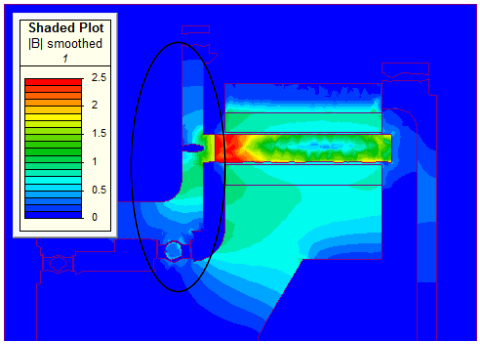

Figure 8: Side-cut, end-effect amplified by the supporting structure.[8]

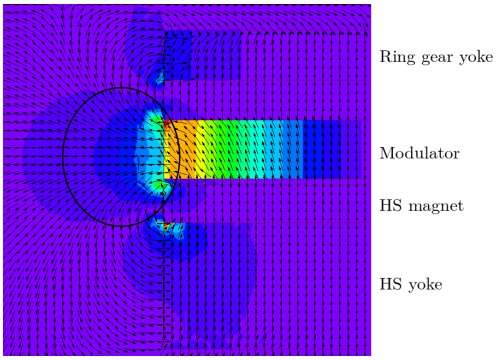

Figure 9: Side-cut view of the z-component of the magnetic flux distribution.[8]

To understand the importance matter of end-effect, a spoke type magnetic gear that was made in 2003[10], encountered severe end-effect. While after 2D-FEM, the stall torque of the machine was evaluated at 27$[N.m]$, it actually dropped out at 16$[N.m]$ after the assembling of the 3D-prototype. By means, the actual static stall torque measured was only 60% of the one predicted by 2D-FEM. The gap between the two results was actually involving severe end-effects, due to an additional bearing installed to overcome mechanical problems[10].

In an other research [11], a 2D-FEM and 3D-FEM comparison of a surface mounted magnet coaxial magnetic gear was performed in order to predict the end effect for a 40$[mm]$ long machine. The radial flux intensity is also evaluated in the z-axis :

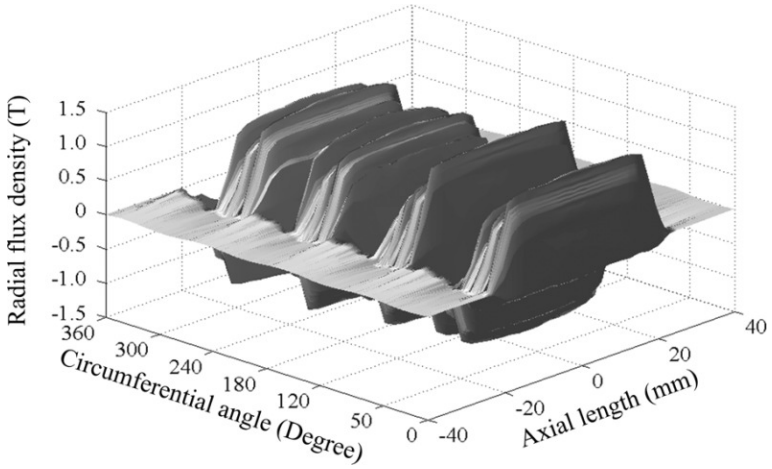

Figure 10: 3D radial magnetic flux distribution of a 40$[mm]$ long surface mounted PM MG.

The pull-out torque obtained from the 2D-FEM, were 51.7$[N.m]$ for the high-speed rotor and 221.1$[N.m]$ for the low-speed rotor. While the 3D-FEM gave as results, 37.3$[N.m]$ and 159.2$[N.m]$ for the high-speed and low-speed rotors. The end-effect is slightly less important since a bit more than 70% of the 2D-FEM predicted torque remained. Nevertheless, the noticeable point, is that the axial length of the gear and the supporting structure are important components to act on the end-effect.

The influence of the stack length over the 3D-FEM performances compared to the 2D-FEM, and thus the influence of stack length over the end-effect, as been implement in[12], and is shown in the figure (11).

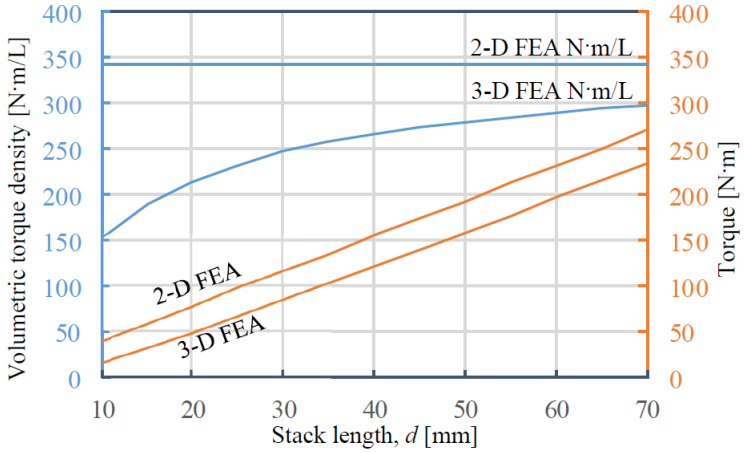

Figure 11: Peak torque and torque density in function of the stack length for 2D and 3D FEM[12].

In the attempt to evaluate the impact of the end-effect over the stall torque, in function of the geometry paramters, S. Gerber and R-J Wand[8], introduced the end-effect ratio E_T, that defines the stall torque ratio between the 2D and 3D FEM.

$$\boxed{\mathrm{E}_T = \frac{T_{3D-FEM}}{T_{2D-FEM}}} \tag{11}$$

An interesting discovery in this investigation, is that the end-effect finds it's origin mostly in the repulsive part of the created torque (the total magnetic torque is the sum of the repulsion torque and attractive torque, inside a magnetic gear). This phenomenon termed as "escaping", occurs when two opposing magnets "force" the magnetic field out of the plane in the z-axis. This phenomenon is illustrated in the below figures[8]. (a) the attractive-responsible magnets. (b) the repulsive-responsible magnets. (c) The z-axis field intensity, showing the "escaping" flux that is stronger in the repulsive-responsible magnets.

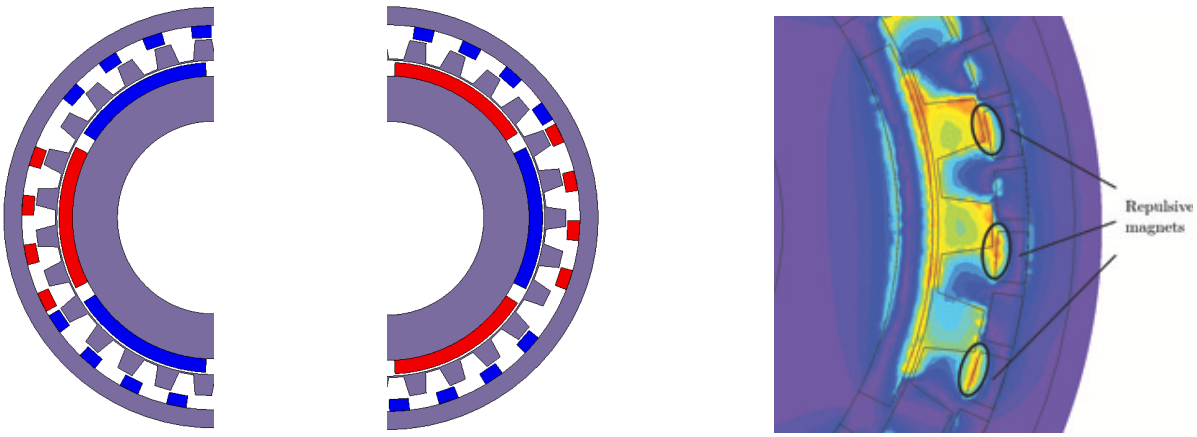

(a) Attracting magnets. (b) Repulsing magnets. (c) Z-axis field intensity on the repulsing side.[8]

The experiment leaded by Rasmussen, T.O. Andersen and F.T. Joergensen in 2003[10], following the end-effect problems due to the additional bearing and it's important decrease of performances (40%), investigated the provenances of the losses.

Firstly, the spoke-type topology used in [10](fig.12) was unable to take the most advantage of the PM's since almost 1/4 of the magnets were used in the magnetic leakage. Indeed, the deep bury of the permanent magnets doesn't focus the field lines near the air-gap which caused severe iron losses in the yoke and the additional bearing[10].

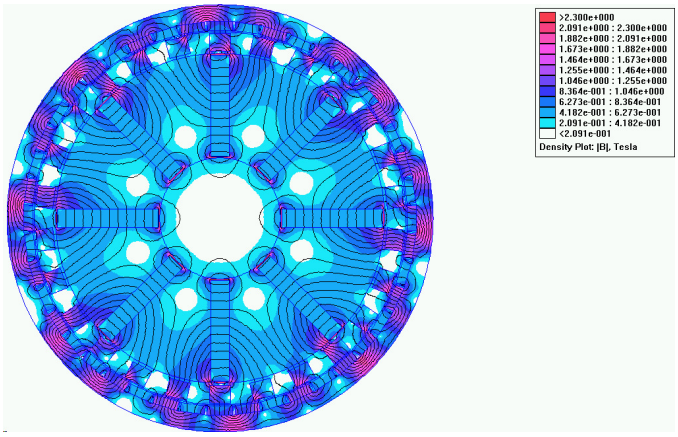

Figure 12: Flux lines for a deep-bury mounted magnets.[10]

Secondly, due to mechanical issues during the assembling of the test gear, an additional bearing had to be piled up to the initial structure. It was placed between the high-speed rotor and the nylon housing of the pole-pieces. To predict the efficiency, iron losses and mechanical losses were measured during a no-load test. The results of the no-load operation are shown below :

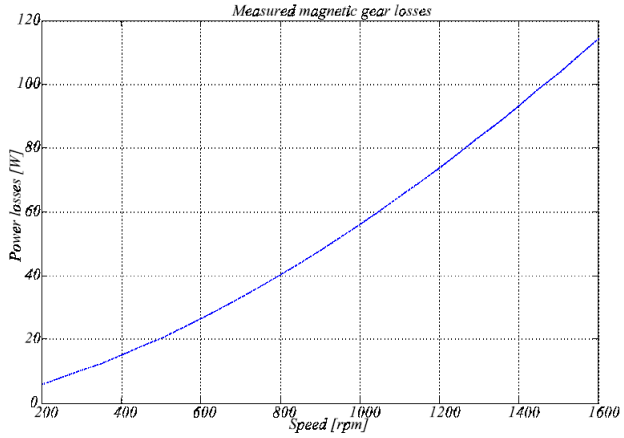

Figure 13: No-load losses in function of angular speed.[10]

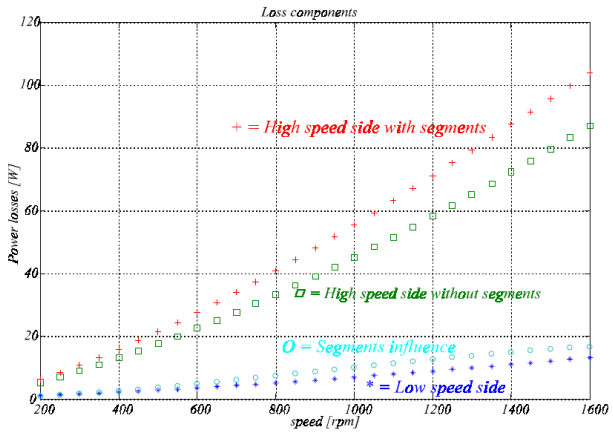

Figure 14: Losses components during no-load operation.[10]

Due to its important scale, the losses components have been separated in partitioned losses, in order to understand their provenances.

It came from these results that the major part is from the high-speed rotor, at which 3 bearing were installed. If the origin of the losses differences between the high-speed side and the low-speed side were only mechanical, it should have been more than 68 $[W]$. All this losses dissipated in friction, which is enormous for just only one bearing difference. The ascertainment from this experiment, was that the additional bearing were the cause of significant end-fields from the rotor magnets which also caused a rise of the iron losses and also gave additional kinematic friction, all these additional effect in consequence of the added bearing.[10]

An other surprisingly high source of losses were the laminated pole-pieces. Which raised at $18[W]$ for a total weight of $0.2[kg]$. This may be explained by the z-axis magnetic flux components that are the cause of important eddy-current since the stator is laminated in the x-y plane.[10]

The main conclusion from the above experiments are the following. In the first place, longer stack-lenght is preferred in order to reduce the end-effect proportion. Also, surface-mounted PM rotor might be a more convenient topology to make better profit of the magnetic flux. Furthermore, the stator segments have to be stacked in the axial length and have to be secured "more efficiently than with nylon-housing"[10]. This point is important to remember since it will be involved in the investigations of this thesis. Finally, special cares are to be given to the cinematic layout in order to avoid mechanical issues. Single-sided bearings are to be outcasted for long-stacked machines. Bearings that support both sides of the low and high-speed rotors are a good solution to solve those issues.[10]

In order to avoid those unexpected losses, the mechanical structure should be considered very carefully since it can lead to tremendous losses and thus erase all the benefits of a good implemented magnet configuration. The following section will cover this subject.

2.4 Permanent magnets configurations

In the precedent section, a research proposed that in some cases surface-mounted PM's might be preferable compared to internal spoke-type PM's. But surface and internal mounted magnets can be of different configurations. This subject was the investigation of numerous studies in the last two decades, since it can lead to important improvements of the magnetic field distribution. Thus, important improvements of the harmonic content and of the flux density at the air-gap. The present section will introduce some of the main investigated topologies. Some of the principle topologies covered by the researches are depicted in fig.15 :

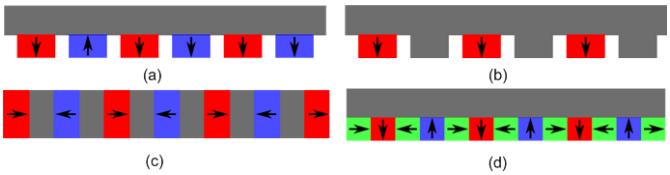

Figure 15: (a) Altenating surface PM. (b) Consequent poles. (c) Spoke-type arrangement. (d) Halbach array PM arrangement.[7]

2.4.1 Halbach arrays

Several authors, like Linni Jian, K. T. Chau and others that published papers in 2009[11] and 2010 [13], covered the application of Halbach array's for coaxial magnetic gears. These papers compared the conventional surface mounted PM magnetic gear and a new version of surface mounted PM with an Halbach array configuration. The conventional and Halbach mounted gears are depicted in [11]:

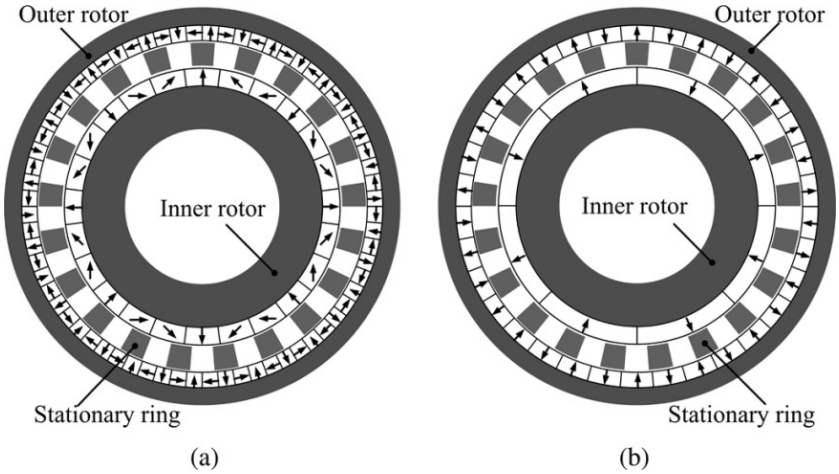

Figure 16: (a) Halbach and (b) Conventional mounted PM magnetic gears topologies

One of the main features of Halbach arrays, compared to conventional surface mounted magnets, is the flux density distribution, that is concentrated in the air-gap, that leads to higher torque transmission.

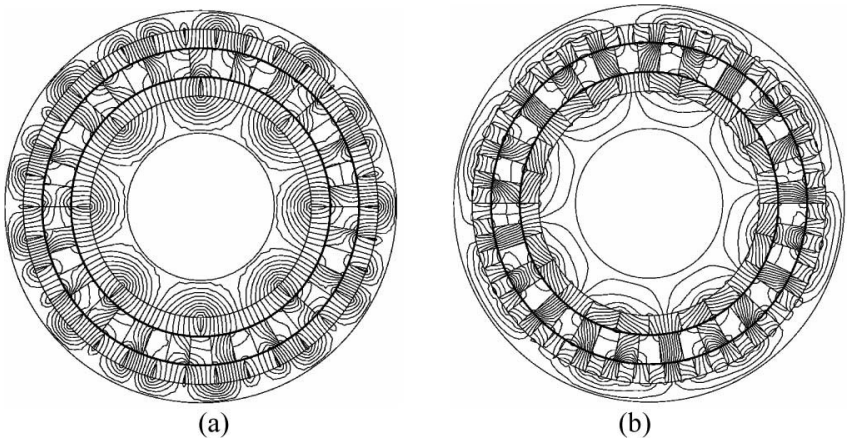

Figure 17: (a) Conventional and (b) Halbach flux density distribution

In the figure 17, we can observe that the Halbach array significantly decreases the magnetic flux density in both high-speed and low-speed rotors yokes. This can allow the reduction of the yoke volume and thus the total weight and inertia of both rotor. The magnetic flux being more concentrated in the ferromagnetic pole-pieces, the iron losses in this section could be more significant. But, as depicted in fig.18 and 19, the Halbach array disposition

also contributes to a significant reduction of the harmonic content, limiting the undesirable components of the space harmonic[13].

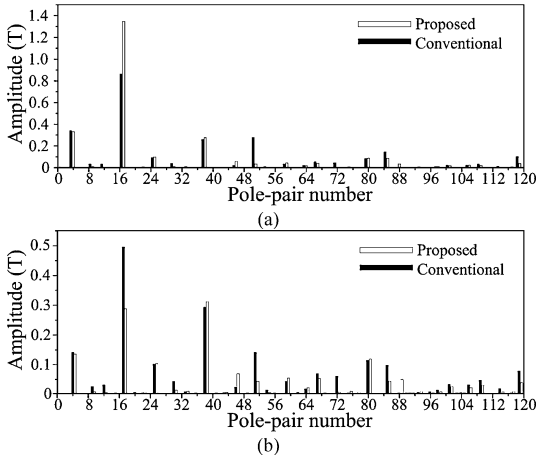

Figure 18: Harmonic spectra of flux densities components in the outer airgap(a) Radial (b)Tangential

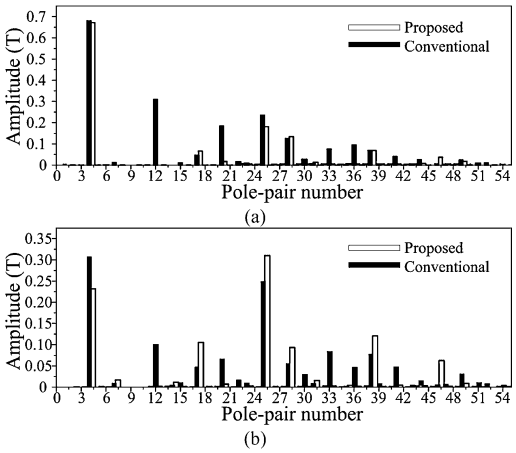

Figure 19: Harmonic spectra of flux densities components in the inner airgap(a) Radial (b)Tangential

In [11], the number of pair of poles at the high-speed/low-speed rotors are $p = 4/17$, the effective harmonics in this application are thus $p = [4, 17, 25, 38, 46]$.

In the figure 19, the pair of pole $p = [12, 20, 28, 33, 36, 41, 49]$ that contribute to the iron losses are present in the conventional surface mounted magnet, but significantly suppressed with the use of halbach arrays. Those numbers of pole components contribute to the iron losses $(12, 20, 28, 36)$, and to the torque ripple $(33, 41, 49)$.[13]

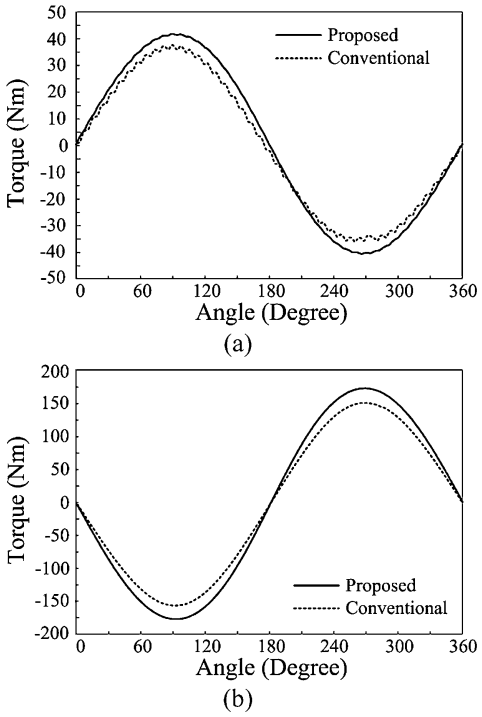

Figure 20: Torque in function of the rotational angle, (a) high-speed rotor .(b) low-speed rotor.[13]

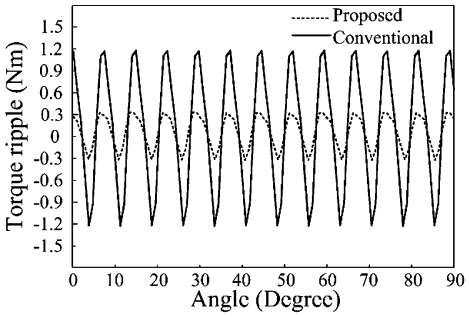

Figure 21: Torque ripple component of the total torque on the high-speed rotor.[13]

The limitation of the ripple-contributing components in the harmonic spectra, has profitable consequences that can be measured on the torque-angle curves of each rotors. In addition of increasing the maximum torque of 13%(fig.20), the ripple component is substantially reduced(fig.21). The conventional surface mounted MG is showing values of cogging torque up to 1.2$[N.m]$, while the magnetic gear using Halbach arrays has only about 0.3 $[N.m]$. This represents a reduction in cogging torque of 67%.[13]

A no-load operation, has been performed to compute the iron losses, which are believed to be the major losses in Halbach array configurations[11]. In figure 22, the no-load iron losses are shown at diverse angular speeds. The benefits brought by the Halbach array in terms of iron losses are noticeable. The most important component of the iron losses is, at the opposite of [10], localized in the stationary pole-pieces. Which firstly shows the better conception of the rotors in [11]. Secondly, as predicted by the harmonic space analysis, even if the field density is more important in the pole-pieces with the Halbach array, the spectrum composition of the field limits the iron losse. By limiting the iron/ripple-harmonic components and by focusing the effective harmonics.[11]

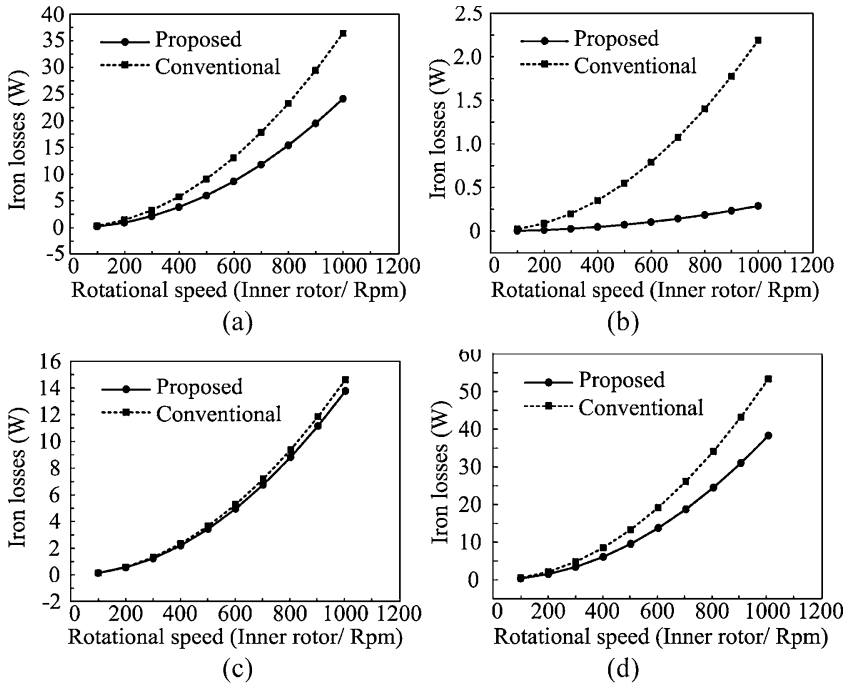

Figure 22: Iron losses in function of the angular speed. (a) Pole-pieces.(b) High-speed rotor yoke. (c) Low-speed rotor yoke. (d) Total iron losses. [13]

2.4.2 Consequent poles

An other alternative to Halbach arrays, in order to improve the efficiency of surface mounted magnets, is the consequent-pole configuration. Instead of using a periodic alternation of South and North poles, as in conventional surface mounted magnetic gears, it employs only one polarization of magnet. The performance of consequent pole rely on the increased reluctant force that is drawn by the ferromagnetic yoke. From this, comes a diminution of the volume of magnet in the construction and thus a better cost efficiency.[14]

A typical consequent-pole topology, is depicted in the figures below :

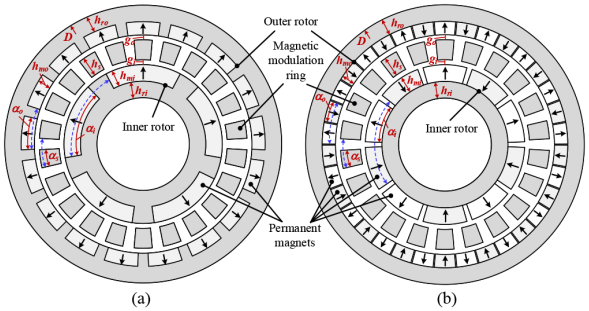

Figure 23: (a) Consequent-pole type. (b) Conventional type.[14]

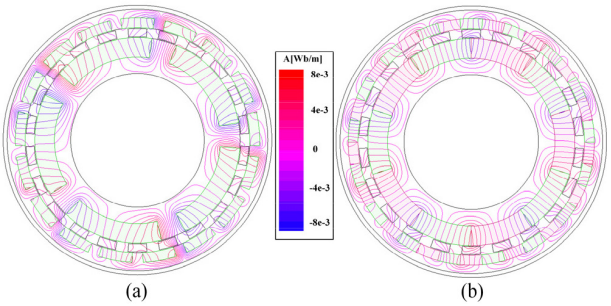

Figure 24: (a) Consequent-pole type. (b) Conventional type.[14]

As shown in fig.(23-24), the south pole magnets are replaced by salient ferromagnetic poles induced by the flux path of the north pole magnets. The actual difference between

the consequent pole magnetic gear and the conventional surface mounted magnetic gear, resides in the pole-arc coefficient, denoted "α"[14]. It is the ratio between the pole-arc $[rad]$ and the pole pair pitch of the corresponding rotor(resp. α_o for the outer rotor and α_i for the inner rotor). By means, the pole-arc ratios of a conventional surface mounted magnetic gear are both 0.5, since the north and south magnet occupy half of the pitch each. For the consequent-pole magnetic gear presented in[14], $\alpha_0 = 0.75$ and $\alpha_i = 0.8$. The volume of magnet reduction is then 25% and 20% for the outer and inner rotors.

This topology, even though it is employing less magnetic material, has demonstrated by FEM and experimentation, paradoxically both higher torque and higher losses. The torque improvement for this type of configuration, was 24% which is a noticeable improvement.

The higher losses for the consequent pole type, comes from the higher number of harmonics in the modulating ring. Also, the end-effect is more important, with an end-effect ratios of $E_T = 0.82$ for the consequent-pole type and $E_T = 0.88$ for the conventional magnetic gear.[14]-[15] The end-effect difference is depicted in the following figure :

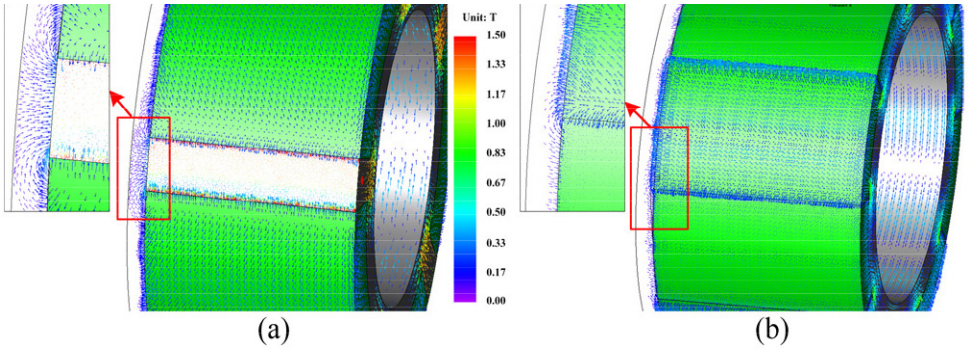

Figure 25: Inner rotor flux deflection density vectors.(a) Consequent-pole type. (b) Surface mounted magnet. [15]

The same authors, leaded a second investigation the year after in 2017 [15], comparing no less than 15 different typologies. This resorted that an even higher torque can be obtained with the replacement of the ferromagnetic stator, by a permanent magnets stator. In some ways, this can be understood as an "active" rather then "passive" modulation of the magnetic field. However, this machine was not implemented, due to the complexity of the latter.[15]

2.4.3 Optimal Permanent Magnet Arrangement

This last topic over the permanent magnet configuration will discuss an interesting method of finding the optimal PM topology. This comes from an investigation published in 2016 by W.N.Fu and Longnv Li[16]. In this article, a novel and innovative general pattern of PM arrangement method is presented. It relies on the determination of PM/ferromagnetic teeth dimensions that are based on the figure 26. From the original method, 5 basic and already well known topologies can be found. Hybrid forms of arrangement are also implemented (fig.27).

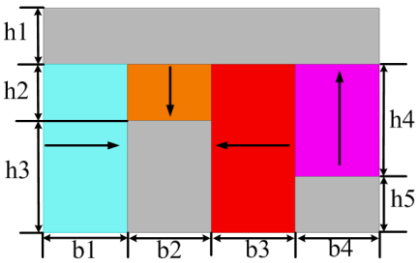

Figure 26: New general pattern of PM arrangement.

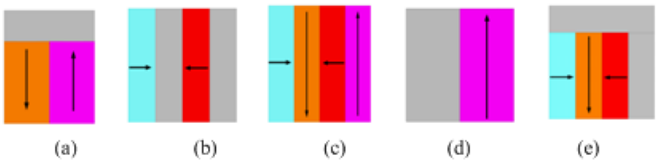

Figure 27: Basic PM arrangement produced by the general pattern.(a) Surface-mounted arrangement. (b) Spoke type arrangement. (c) Simplified Halbach magnet arrangement. (d) Simple consequent-pole type arrangement. (e) Consequent-pole Halbach magnet arrangement.

Two configurations were implemented.

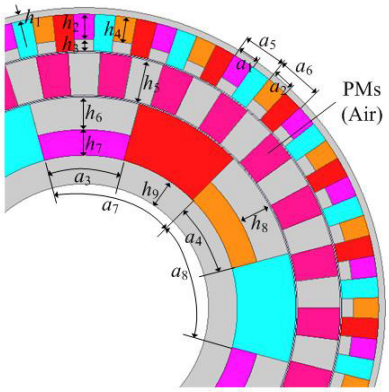

Figure 28: Dimension parameters of the Magnetic Gear (b).

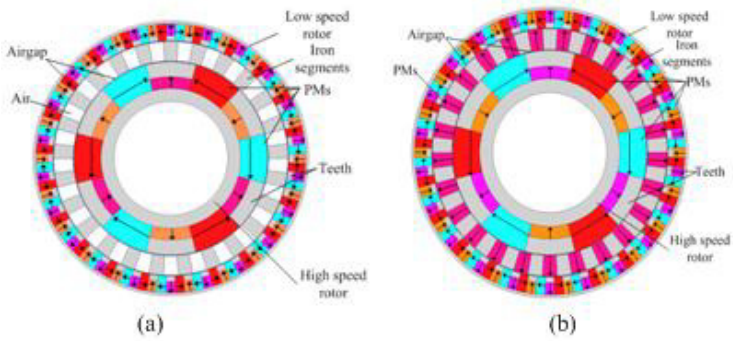

Figure 29: (a) First proposed magnetic gear implemented with the new method (b)Second proposed magnetic gear with additional set of magnets in the stator.

The multiple dimensions are then found using a tabu search algorithm that is described in the paper. The results of the two implemented magnetic gears, compared to a conventional surface mounted PM magnetic gear, were relatively impressive. Indeed, the first topology showed a peak torque 62.12% higher than a conventional magnetic gear and the second one 92.18% higher than a conventional magentic gear. [16]

However, the evaluations only come from 2D-FEM, thus neglecting end-effect. Secondly, the apparent complexity of this type of mounting cannot hide the important challenge proposed by constructing such a gear. Lastly, the amount of PM needed in these types of magnetic gear, certainly is greater than for the above-mentioned topologies. Thus, the evaluation of the cost-efficiency of these configurations surely should be investigated.

2.5 Modulating Ring

In the previous topics, diverse articles demonstrated that the PM configurations, represented, without much surprise, a fundamental role in the magnetic gear performance. Thus this area is widely investigated and sometimes lead to original improvement as shown in [16]. However, it has been pointed out, that the pole pieces were also an important part of the magnetic gear as well and could lead to severe losses when wrongly implemented or secured [10].

2.5.1 Pole-pieces shape factor

The shape factor of the pole pieces is by means, an important section to explore, in order to obtain high torque density and efficient magnetic gear. In a cylindrical reference(fig.30), the section of the pole pieces are defined by an inner and outer radius R_i and R_o. The radial thickness "r_p" is then defined as the difference of those too dimensions. The revolution angle "α"is also defined, and in most application, corresponds to half of the pole-pieces pitch, which corresponds to a pole-arc coefficient of $\alpha_s = 0.5$.

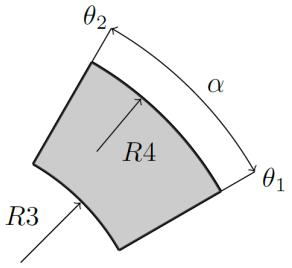

Figure 30: Pole piece section in the cylindrical reference.[17]

The influence of the radial thickness over the transmitted torque has already been checked in the first coaxial magnetic gear publication by K.Atallah [6]. This investigation has been reiterated in 2014 [8][18], alongside the influence of the radial thickness over the end-effect ratio.

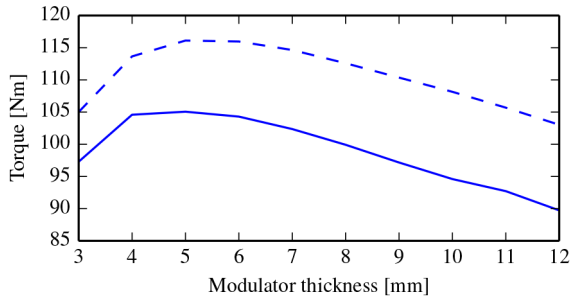

Figure 31: Maximum transmitted torque in function of the modulator radial thickness.[8]

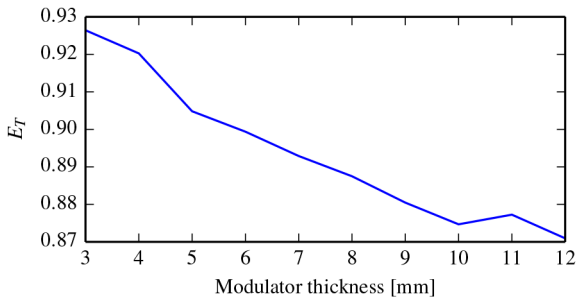

Figure 32: End-effect ratio for a given length and with a variable radial modulator thickness.[8]

The figure 33, shows that an optimal radial thickness for the peak torque transmission exists around $4 - 6[mm]$[8]. The figure 34 shows that a linear-like relation exists between

the radial thickness and the end-effect ratio. This could also explain the excessive decrease from the 2D-FEM to the 3D-FEM in [10], in which the radial thickness was of 8[mm]. Of course, the other dimensions are not taken into account and this ascertainment doesn't rely on prooves.

Those results have been confirmed by [14], where the pole-arc coefficient was also expressed in function of the radial thickness and the torque capability of the outer rotor(fig.33. The maximum region is included within the region of $\alpha_s = [0.5, 0.6]$ and $r_p = [4mm, 6mm]$. This can be also compared with the results of [18], for which the pole-pieces pitch angle is 5.3°, with a maximum angular span of the pole pieces located at around 7°. Which corresponds to a pole-arc ratio of $\alpha_s = 0.66$.

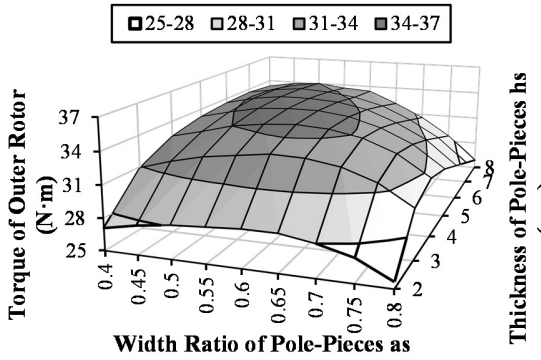

Figure 33: Torque of the outer rotor in function of the radial tickness and the pole-arc coefficient.[14]

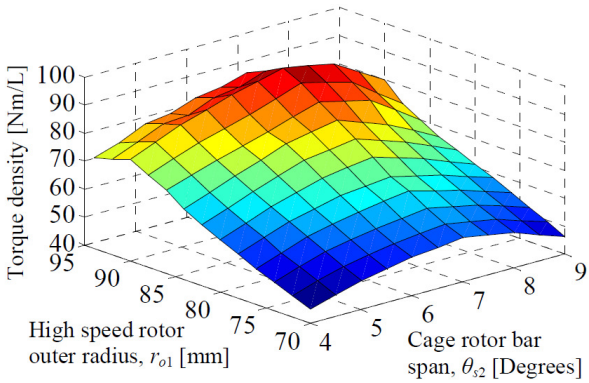

Figure 34: Torque density capability in function of the pole-arc ratio and the high-speed rotor outer radius.[18]

Even though the results in different investigations, have comparable results, the optimum shape factor of the pole pieces is dependant of a consequent number of parameters, which should be taken into account for every, magnetic gear configurations.

An investigation that was conducted in 2013, also showed that the introduction of an additional dimension of the pole-pieces section, could lead to greater torque transmission capability[19]. This is implemented with an additional circular cut in the middle of the laminated sheet, as showned in figure 35. One of the main features of this implementation, is the improvement of the cohesion between the laminated sheets and the resin molded housing, for which a "groove in the middle, would prevent detachment from the resin". The laminated sheets are ineed locked in the radial direction thanks to the groove. An additional feature of a narrowed pole pieces shape, is the higher magnetic flux density compared to conventional rectangular shapes, which can increase the torque transmission capability of5.5%. Besides, the larger air-gap between the pole-pieces, also prevents from magnetic leaks inside the modulating ring. However, when the middle becomes too thin, magnetic saturation appears, and the peak torque transmission decreases.[19]

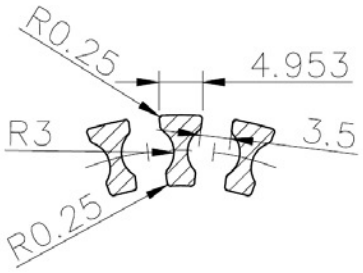

Figure 35: Grooved pole-pieces shape.[19]

2.5.2 Stationary pole-pieces supporting structures

The experiments that have been treated above, mainly concerned the optimization of the magnetic circuit. The means employed to achieve an increased torque transmission and increased efficiency, were through the optimization of diverse topologies or permanent magnets layout types or the shape factor of the pole pieces. Nevertheless, the majority of the studies also mentioned the fundamental role of the robustness of the statoric pole-pieces under the magnetic constraints. It has been found that a torsional angle of 1 deg at the pole-pieces, can lead a to a drop of 23% of the total transmitted torque[1]. It follows that all the possible improvements in terms of topology and layouts don't represent a consistent improvement for the magnetic gears if the integrity of the pole-pieces isn't secured.

Besides, the shape of the modulating is also heavily involved in the global performance of the magnetic gear. It holds a major role in torque transmission capability[19], magnetic flux leakage handling[20] and end-effect diminution[8]. The limitation of the iron losses inside the pole pieces is obtained using laminated steel sections. This creates a shortage inside the pole pieces that prevents the Eddy current from circulating inside the modulating ring.

An investigation on the strengthening of the stator has been carried out by Nicolas W.Frank and Hamid A.Toliyat[9], in which a steel bridge is linking the laminated statoric pole-pieces. The strengthening of the high-speed rotor is also elaborated.

Three different bridged stator alternatives have been proposed and the magnetic performances have been investigated. The stator pieces were connected by a $0.3[mm]$ bridge. In the first variation, the stator pieces were connected on the interior, the second on the exterior, and the last one on both sides[9].

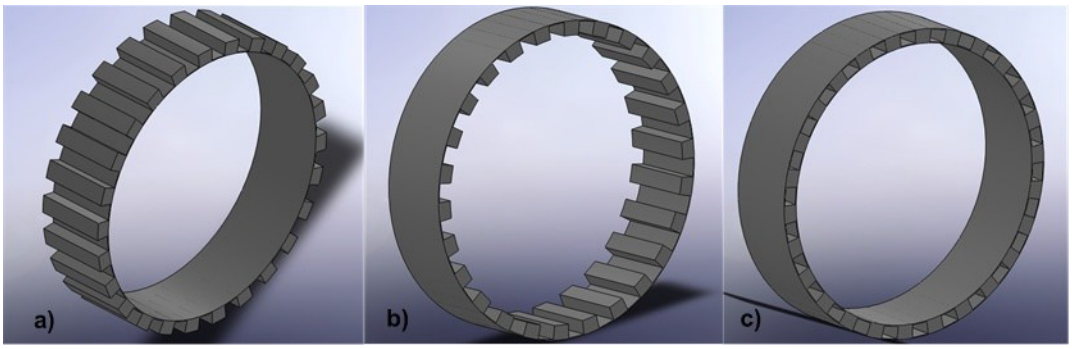

Figure 36: Stator altrnatives (a) interior bridge. (b)exterior bridge. (c)bridge on both sides.

The results obtained from the simulations shown that the torque rating was more affected by the exterior bridge(23%)and both sides connection(26%). As for the inner bridge connection, the rated torque was decreased by only 2%[9]. The decrease of transmitted torque, can be explained by the fact that when the pole-pieces are connected to each other, the magnetic flux is short-circuited inside the magnetic path. The flux leakage can rise up to 30% in order to match the strenght of the magnetic poles. The flux leakage presented by [9] is illustrated in fig.40. In [19], the same principle of bridged stator pieces has been analyzed. In this configuration, three different bridges where placed between the pole pieces, but this time with one placed in the middle of the geometry.

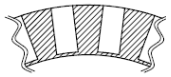

Figure 37: inner bridge.[19]

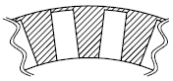

Figure 38: outer bridge.[19]

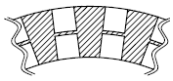

Figure 39: middle bridge.[19]

In those configurations, the bridged was $0.5[mm]$ thick, which is almost double in size of the one in[9]. The rated torque decreased slightly lower as a consequence of the thicker connection. The torque rating for the basic configuration, was $20.5[N.m]$. The inner, outer and middle bridged pole-pieces, had rated torques of respectively $18.6[N.m](-9.3\%)$, $14.2[N.m](-30.4\%)$ and $17.5[N.m](-14.6\%)$.

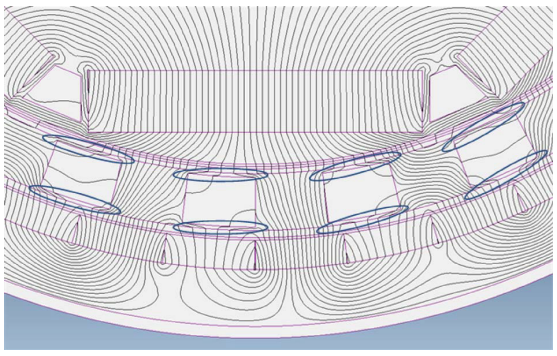

Figure 40: Flux leakage at the additional bridges.[9]

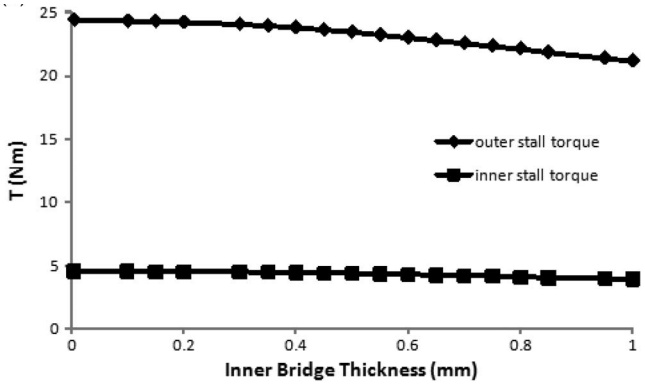

Figure 41: Stall torque in function of the inner bridge thickness.[9]

It can be observed that both examples from [9] and [19], had lower drop in performances for the stator with the inner bridge. However, the second application shows a drop of roughly 7% lower than the first one. The relation between the thickness of the bridge and the stall torque of the machine in [9] is depicted in fig.41. It is noticeable that the nominal drop in function of the bridge thickness, doesn't match the one in [19].

2.6 State of the Art : conclusion

Even if many improvements have been brought to the coaxial magnetic gear. However, in many articles the robustness of the pole-pieces, although often mentioned, leans on dubious methods. Those methods consist in general of molding the steel sheets in a resin housing(i.e [1][13][10]) or linking the pole pieces with a bridge(i.e [21][9][19]). Even if those are coherent methods to improve the torsional resistance, nothing has been measured or simulated yet in order to predict the behavior of the laminated poles under the magnetic constraints.

3 Design

3.1 Objectives and specifications

The original purpose of the thesis, was the implementation and design of a magnetic gear and its benchmark, the main objectives being to implement a high torque density magnetic gear with a high efficiency. In order to reach the objectives, the magnetic gear has to respond to several basic criterions in the first place. That is why, at the beginning of this thesis, the first step was to set up the specifications of the machine to be made.

At first, the functional characteristics had to be in adequacy with what was available in the present state of the advances in terms of magnetic gears technologies. The magnetic gear has to be composed of three independent cylindrical stages, following the CMG configuration. Two being composed of surface mounted permanent magnet, both connected with external shafts. The two shafts are the accesses to the input and the output powers. The input and output have a range of torque and angular speed that depends on the potential of the magnetic circuit to transmit power, and on the structural ability to support those power transmissions. Typically, the range of torque at the input and output shafts for an the commonly tested scale of the machine, were around $10[N.m]$ at the high-speed rotor, and arround $50[N.m]$ at the low-speed rotor. The reduction ratio is by then often defined between $5:1$ and $6:1$. The nominal rotation speed of the high-speed rotor, is also an important matter. The magnetic gear should be designed to sustain a high rotational velocity, up to $314[rad/s](50[Hz])$ for the high-speed side, since it is a common nominal speed for electric alternators. From these last functional characteristics, the maximum transmission power is deduced at about $4[kW]$. The magnetic gear should also allow access to several sensors, including dynamometer, thermometers and strain gauges all along the machine, in order to extract torques, heats, and strain deformations. All these basic assumptions were made to set the basis of a consistent test prototype which would allow a deep and extensive analysis of the machine.

Secondly, concerning the constraints, the dimensions of the machine have to be contained in a cylinder with a diameter of $150[mm]$ and a length of $200[mm]$, in order to be easily contained and tested in a room-scaled benchmark. The constraints over the security level is also an important matter. Indeed, the whole system must be completely sealed from the outside while operating, with only the input and output shafts from both sides to be opened and accessible. Since no contact is supposed to happen inside the CMG, no overload constraints must be specified. One last point is that the selected magnetic configuration of the magnetic gear, should ensure low ripple, in order to maintain structural integrity, while functioning at high rotation speed.

All the above assumptions are taken in the following specification table.

Table 1: Magnetic gear specifications

Functions	• Speed/Torque reduction between the input/output shafts	**Function requirements: Criteria and levels**	• Input upper limits :$\omega_{in,max} = 314[rad/s], C_{in,max} = 10[N/m]$ • Output upper limits :$\omega_{out,max} = 0.2.\omega_{in,max}, C_{out,max} = 50[N/m]$ • speed ratio : $r = \frac{\omega_{out}}{\omega in} = [5-6]$ • Maximum power transmission : $4[kw]$ $(P_{max} = C_{in}.\omega_{in})$
Constraints	• Dimensions • Safety • Rules • Scale (Based on the real application for Alstom^{TM}) • Ripple	**Constaints requirmeents : criteria and levels**	• Dimensions : $D_{ext} = 15cm, L = 20cm$ • Security : No free access to the rotating shafts during operation. • rules : Tension in the bolts, resistance of the materials, bearings, etc. To clarify with the suppliers. • Scale : Dimensions = $1/5[m/m]$ Torque density = $1/125[N.m/m^3]$ • ripple : Optimal structure and layout to be defined numerically.

In order to test the prototype, a benchmark has to be implemented. The latter should be able of providing the input power by the means of DC/AC motor with enough power to reach -if possible- the $4[kW]$. The power that, in theory, should be handled by the magnetic gear. The benchmark should be equipped with a torque transducer in order to couple the mechanical power input to the magnetic gear. On the other side, at the output, a resistant torque needs to be applied by the means of a magnetic break, or simply an alternator functioning in generating mode. Finally, the benchmark should provide a full set of measuring instruments, including a gyroscope, and a dynamometer, in order to measure the speed and the torque of both the input and output shafts.

Table 2: Benchmark specifications

Fonctions	• Applies an input torque, as well as an opposite breaking torque • Measures a series of parameters(constraints, torque, angular speed, temperature, ..) • Operate a power balance over the transmitted power • Switches of operating mode	**Function requirements: Criteria and levels**	• Input upper limits :$\omega_{in,max} = 314[rad/s], C_{in,max} = 10[N/m]$) • Output upper limits :$\omega_{out,max} = 0.2.\omega_{in,max}, C_{out,max} = 50[N/m]$ • Sensors consistently distributed • Electronic or mechanic command on a locking system for the rings
Constraints	• Dimensions • Safety • Standards and norms for the AC/DC motor	**Constraints requirements : criteria and levels**	• Room dimensions ($L_{max} = W_{max} = 1m$) • Safety : Sealed gear, no live wires, etc.. • Standards : $V = 230[V], 50[Hz]$

3.2 Cinematic design

The second step of the design was the analysis of the possible cinematic solutions for the magnetic gear. To proceed so, the attention has been brought to the location of the bearings that will support the structure. As already seen in [10], a bad cinematic conception, can lead to the necessity to add up an additional supporting bearing, which can in turn, lead to greater end-effect and decrease the global performances of the magnetic gear. Two principle types of bearings configurations are used to support the rotors and the modulating rings. The first one is the cantilevered configuration, simple in application, good reliability and small deflection for small structures. The second is the vice configuration, more complex in application since one bearing is directly placed inside the structure, but the possible improvement of performances and smaller deflections thanks to the two-sided support. In the figures 42 - 47, the considered cinematic options are exposed. The color designations are the following :

- Low-speed rotor
- Modulating ring
- High-speed rotor

3.2.1 Held modulating ring("stator")

This is the most commonly used configuration. Since the modulating ring is a very complex structure. Besides, since the rotation of the modulating will occur deflection in the radial direction, and since it is the most brittle components, the steady modulating ring seems the best operating mode. However, even when they are held stationary, it still represents an important challenge in the conception of the magnetic gear. In the present case, they are integrated in a rigid structure that also support the high-speed side.

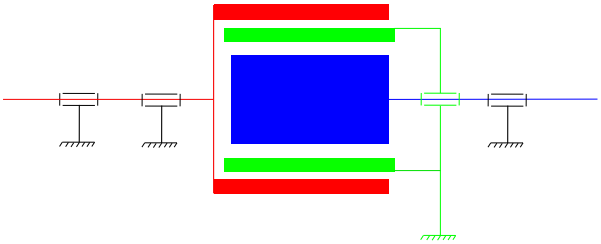

Figure 42: Cantilevered High-speed/Low-speed rotors. Grounded stator.

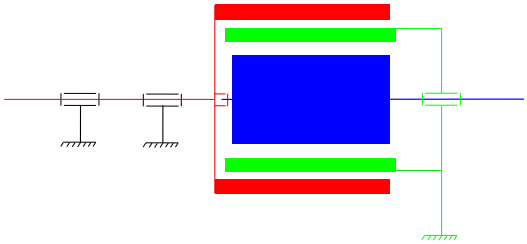

Figure 43: Cantilevered Low-speed rotors, viced High-speed rotor. Grounded stator.

3.2.2 Held High-speed Rotor

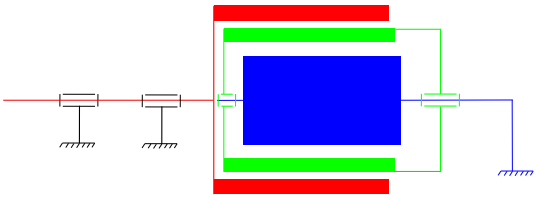

Figure 44: Cantilevered Low-speed rotor, viced stator on high-speed side. Grounded High-speed rotor.

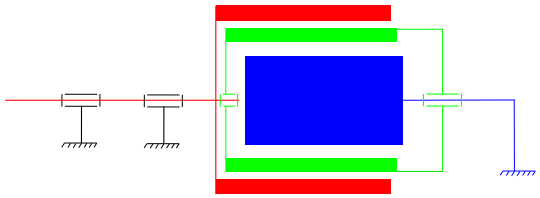

Figure 45: Cantilevered Low-speed rotor, viced stator on low-speed side. Grounded High-speed rotor.

3.2.3 Held Low-speed Rotor

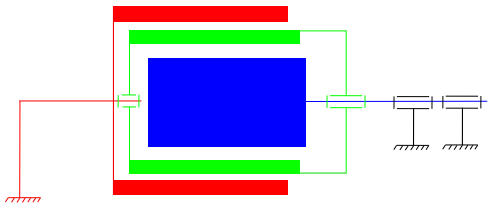

Figure 46: Cantilevered High-speed rotor, viced modulating ring. Grounded Low-speed rotor.

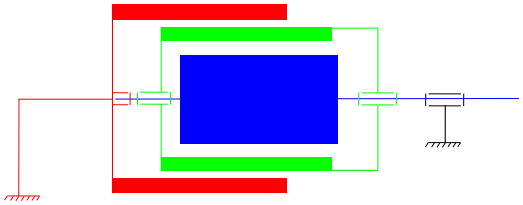

Figure 47: Viced High-speed rotor and modulating ring. Low-speed rotor.

In first two cases the low-speed side must be cantilevered because of the necessity to "open" the structure from both sides in order to assemble the magnetic gear and to get access to the

input and output shafts. Furthermore, in most applications, the low-speed side(outer rotor) is destined, due it's large radius, to be the component with most inertia and is also more likely to be the heaviest part of the magnetic gear. Then it represents a good anchor point to support the high-speed rotor or the modulating ring.

From the examination of the possible cinematic configurations, it appears, that the most common choice that is the anchoring the modulating ring as a stator, represents, both an easier and a more reliable structure to implement. Cantilevering the high-speed side is a question that should be investigated in function of the weight and dimensions of the magnetic gear, especially to find the resonant frequency to avoid possible damage while rotating at high speed. Still, it offers simplicity and allows the insurance of minimizing the end-effect, since the bearing is not very near the magnetic field. Nevertheless, the viced high-speed rotor, seems to be the most suited option for it's compactness and reliability to prevent radial deflections.

3.3 Morphological diagram, literature synthesis

At this stage, it has been clearly defined, that the future axis of the investigation, would concern the modulating pole pieces and their structure. Indeed, the permanent magnet configuration, represent a large part of the attention paid to magnetic gears, leaving behind the extension of the modulating poles experiments. However, it has been shown in several studies that the pole pieces occupy a major role in the global performances of the machine. We can remind that the twist of the pole pieces of only 1, decreases the performance by 23%[6]. The influence of the magneto-mechanical deflection over the air-gap distance between the rotors and the modulating ring, is also investigate in [22]. The paper shows, that torsional and radial rigidity are key points to be considered during the conception of the stator. Secondly, the pole pieces experience severe losses, due to end-effect and eddy-currents, as shown in [10],[14] and [20]. Lastly, the creation of a modulation ring, is a complex and delicate process, since the air-gap between the permanent magnets and the modulating ring is very small and that the the steel bars are, in most cases, laminated.

The next step taken in the design processing, was the setting of a morphological diagram. By means, this is a tabular taking diverse solutions possible and which compares each solutions on selected items concerning major performances aspects. The ratings of the criterions are on a 5-point-basis and are expressed as follow :

- 0 : inappropriate
- 1 : poorly adapted
- 2 : moderately adapted
- 3 : sufficiently adapted
- 4 : Well adapted
- 5 : perfectly adapted

It is important to notice that this rating is documented as far as possible. This means that the rating involves a good share of "common sense" and personal reflection. Also, the purpose of the following procedure is to guide the reflection and the direction to be taken for the prototype.

Criterion	(1)	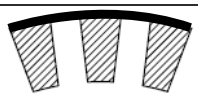 (2)	(3)	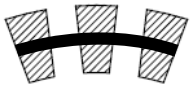 (4)	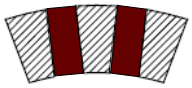 (5)
Torque transmission	**4**	**3**	**3.5**	**2.5**	**4**
Weight	**3**	**2**	**2**	**2**	**2.5**
Total performance	**7**	**5.5**	**6**	**4.5**	**6.5**
Torsion rigidity	**-**	**2**	**2**	**2.5**	**3**
Radial deflection	**-**	**2**	**3**	**2.5**	**1**
Wear, lifespan	**-**	**4**	**4**	**4**	**2**
Total Rigidity	**-**	**8**	**9**	**9**	**6**
Cost	**-**	**3.5**	**3.5**	**3.5**	**3**
Complexity	**-**	**4**	**4**	**4**	**2**
Total conception		**7.5**	**7.5**	**7.5**	**5**
TOTAL	**-**	**20.5**	**22**	**21**	**17.5**
	(6)	(7)	(8)	(9)	(10)
Torque transmission	**3.5**	**4.5**	**4**	**4.5**	**4**
Weight	**2**	**4**	**3**	**3.5**	**3**
Total performance	**5.5**	**8.5**	**7**	**8**	**7**
Torsion rigidity	**4**	**-**	**2**	**3**	**4**
Radial deflection	**4**	**-**	**3**	**1**	**4**
Wear, lifespan	**3**	**-**	**2**	**2**	**3**
Total Rigidity	**11**	**-**	**8**	**6**	**11**
Cost	**3**	**-**	**3.5**	**3**	**3**
Complexity	**3**	**-**	**4**	**3**	**3**
Total conception	**6**	**-**	**7.5**	**6**	**6**
TOTAL	**22.5**	**-**	**22.5**	**20**	**23.5**

Table 3: Morphological diagram, figures inspires from [19]

In the tabular 3, the configurations (1) and (7), with no supporting structure, serve as references. The purpose is to evaluate the structure strengthening method and the consequences over the transmitted torque.

3.4 Conclusion and Objectives

What comes as an ascertainment, from the morphological diagram, is that the literature analysis concerning CMG's, provides insufficient data in order to modelize the behavior of the laminated pole pieces structure under constraints, and thus to give a good approximation of the expected torsion angle. In [22], a deflection model of the modulating ring is proposed as shown in figures 48 and 49. However, the structure consists of steel bars without any presence of lamination, which, allows considerable eddy-current flows through the bars. That is why, in the context of this thesis, the set of new objectives is drawn. In the view of the insufficiency of the mechanical study of the magnetic gears, the creation a 3D finite element method on the behavior of laminated structures, under magneto-mechanical constraints has been highly motivated.

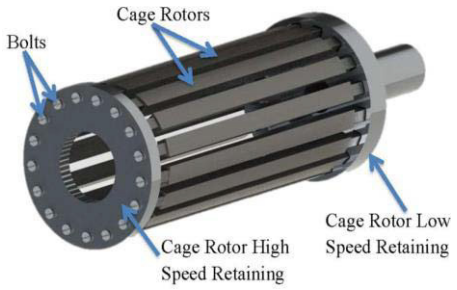

Figure 48: Modulating ring composed of steel bars. [22]

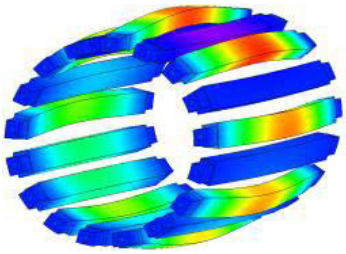

Figure 49: 3-D deformation under magnetomotive force.[22]

4 Theoretical approach

Following the decision of implementing a new model for the deformation behavior of the laminated pole-pieces, a new procedure as been started. The procedure includes first a theoretical approach, based on literature researches and personal reflection. In order to find a consistent method of computation for the laminated beam deformation. As explained further, the literature researches to find a suitable theory for the current application will be in vain. Nevertheless, based on this section, a 3-D FEM model will be implemented and the produced results interpreted in order to hopefully provide a good answer to this problem. Ideally, a laboratory experimentation should also have been conducted, but time was missing for this last validation.

4.1 Problem definition

The magnetic gear is composed of 3 cylinders. 2 PM mounted rotors, and one modulating ring. The ring is itself composed with a number of laminated bars, which dimensions and number are defined beforehand. Following the ways of fastening the laminated steel sheets together to form the elongated ferromagnetic pole bar, the strength of the global structure will change and thus the torsional angle, the radial displacement and tangential displacements will be different under the same constraints. In some articles(i.e [8]), the laminated steel sheets, were held together using a resin molded housing, has shown in fig.50. In others(i.e [19]), a bridge was employed to link the ferromagnetic poles together(fig.**??**). Some also didn't laminated at all the sections, using simple steel beam-type ferromagnetic poles. As seen in figure 48. Nevertheless, only the laminated modulating rings configurations are considered in the context of the thesis, since it offers the best solution to handle eddy-current.

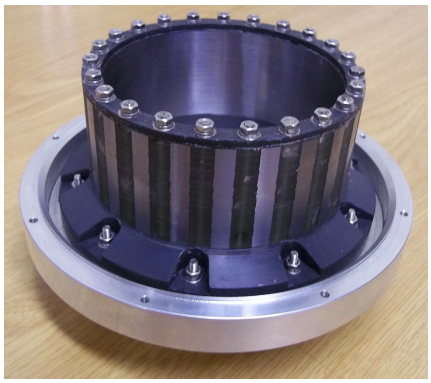

Figure 50: Modulating ring, with a resin molded housing. [8]

Figure 51: Pile stack of laminated steel sheet.[8]

The matter of the physical behavior of the laminated pole pieces, has already previously been treated. In [9], a bridged laminated pole section staking is treated like a regular beam, for which the overall system is considered homogeneous and isotropic. This assumption leads to the direct computation of the torsional twist angle expressed with the following relation :

$$\theta = \frac{T \cdot l}{G \cdot J} \qquad [rad] \tag{12}$$

With G, the shear modulus, T the torque at one end of the beam, l the length and J, the polar moment inertia. This relation would be accurate, if a perfect contact, without any friction, between the laminated sheets could be assumed and thus, all the shear constraints would be transmitted through static contact and deformation. However, this assumption will be tested in the context of the thesis, in order to evaluate the impact of the lamination on the overall effective material properties.

The torsional twist isn't the only deformation happening during the operation. Indeed, the transverse magnetic flux induces an in-plane force applied on the ferromagnetic sheets that can be separated on a radial and a tangential component. This force tends to maximize the magnetic flux flowing through the magnetic circuit and is known as reluctant force. The reluctance of the circuit is dependant on the shape, the permeability of the material and the air-gap length. This force's components can be determined by integrating the Maxwell Stress Tensor over the section. This point covered in the eponym section.

4.2 Hypothesis

In order to implement a simplified -but still consistent- representation of the problem, the definition of a set of hypothesis is done.This will serve as a guideline during the researches and the finite element implementation. As we will see below, the limitations of the finite element method, will sometimes restrain the possibilities, so further simplifications will be made and mentioned when they will occur. Nevertheless, the following items are the hypothesis that defines the new investigated problem. The hypothesis chosen are the following :

- The modulating ring is composed of a stacking of number n of independent sheets of thickness t.
- All the independent sheets present the same dimensions.
- The material composition of each sheets is the same and is in this particular case, structural steel.
- The contact at the interface is homogene and is characterized by a section surface A and a friction coefficient η_s
- There is no force generated in z-axis, and thus $F = F(r, \theta)$.
- The moment about the y-axis and x-axis are null, and thus $M = M_z$
- The moment and the force are both concentrated on the center point of the effective section.
- The moment and the force is equally distributed along the z-axis.

A simplified representation of the problem with it's assumptions is illustrated below :

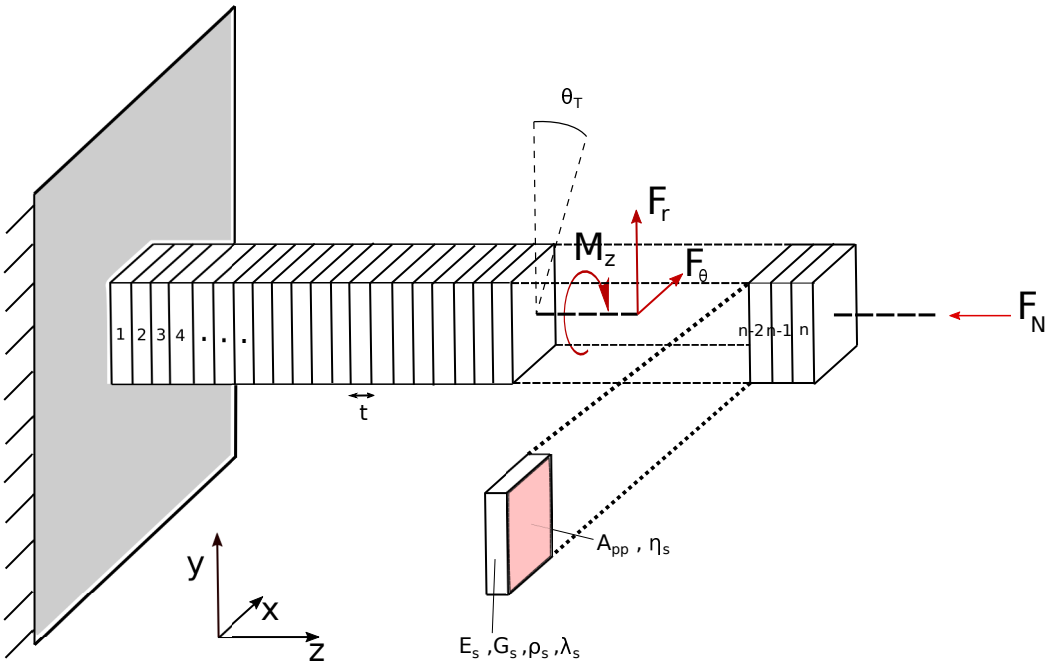

Figure 52: Simplified representation of the problem.

4.3 Simple and higher order lamination theory

In the attempt to find a consistent theoretical basis to predict the behavior of laminated systems, new searches in the literature has been made. The actual state of the theory of laminated structures, can be divided in sub-theories. Among which, the Classical Laminated Theory(CLT)[23, 24], the Shear Deformation Theory[25, 26, 27], the Interlaminar Stresses computation[28, 29, 30] which is based on a Higher Order Laminated Theory[31, 32, 33, 34]. And finally the Effective Moduli Method [35, 36, 37, 38, 39, 40].

The first important remark to be noted, is that in the lamination theory, the thickness-axis (z-axis), is considered to be very small compared to the planar dimensions (x-y plane).

The Classical and Higher Order Laminated theories, are used to predict the displacement field of laminated plates by the means of approximation function. The Classical theory neglects the shear deformations and thus only consider the "in-plane" deformations. Those core assumptions of course directly disqualify the consistency of this theory for the present application. The Higher-order theory, although the above-mentioned hypothesis of dominant planar dimension is still considered, introduces this time through-thickness polynomial displacement functions that enable the computation of the z-axis displacement and stress fields. However, in the present studied papers, the only covered deformation was bending, buckling, and vibrations. We recall that the main deformations considered in the present application, are the axial torsional twist, the radial and tangential bending, which are not considered here at the profit of the normal load and it's distribution. Therefore, again there is no really important connections between the present application and the above-mentioned papers.

Finally, the Effective Moduli Method, might present some interesting tools for the current problem. Indeed, the purpose of this method is to find equivalent elastic constants, following the Hook'law[40] :

$$\begin{bmatrix} \bar{\sigma_1} \\ \bar{\sigma_2} \\ \bar{\sigma_3} \\ \bar{\sigma_4} \\ \bar{\sigma_5} \\ \bar{\sigma_6} \end{bmatrix} = \begin{bmatrix} \bar{C_{11}} & \bar{C_{12}} & \bar{C_{13}} & \bar{C_{14}} & \bar{C_{15}} & \bar{C_{16}} \\ \bar{C_{21}} & \bar{C_{22}} & \bar{C_{23}} & \bar{C_{24}} & \bar{C_{25}} & \bar{C_{26}} \\ \bar{C_{31}} & \bar{C_{32}} & \bar{C_{33}} & \bar{C_{34}} & \bar{C_{35}} & \bar{C_{36}} \\ \bar{C_{41}} & \bar{C_{42}} & \bar{C_{43}} & \bar{C_{44}} & \bar{C_{45}} & \bar{C_{46}} \\ \bar{C_{51}} & \bar{C_{52}} & \bar{C_{53}} & \bar{C_{54}} & \bar{C_{55}} & \bar{C_{56}} \\ \bar{C_{61}} & \bar{C_{62}} & \bar{C_{63}} & \bar{C_{64}} & \bar{C_{65}} & \bar{C_{66}} \end{bmatrix} \cdot \begin{bmatrix} \bar{\epsilon_1} \\ \bar{\epsilon_2} \\ \bar{\epsilon_3} \\ \bar{\epsilon_4} \\ \bar{\epsilon_5} \\ \bar{\epsilon_6} \end{bmatrix} \quad (13)$$

$$\bar{C_{ij}} = \sum_{k=1}^{N} \nu_k C_{ij}^{(k)} \qquad i,j = 1.2.3.6 \quad (14)$$

$$\frac{\sum_{k=1}^{N} \nu_k C_{ij}^{(k)}}{\Delta_k} / \Delta \qquad i,j = 4.5 \quad (15)$$

$$\Delta = \Big(\frac{\sum_{k=1}^{N} \nu_k C_{44}^{(k)}}{\Delta_k}\Big)\Big(\frac{\sum_{k=1}^{N} \nu_k C_{55}^{(k)}}{\Delta_k}\Big) - \Big(\frac{\sum_{k=1}^{N} \nu_k C_{45}^{(k)}}{\Delta_k}\Big)^2 \quad (16)$$

$$\Delta_k = C_{44}^{(k)} C_{55}^{(k)} - (C_{45}^{(k)})^2 \quad (17)$$

Where the equivalent elastic constant $\bar{C_{ij}}$ are calculated in function of the material elastic constants C_{ij} and the volume ratio of the laminates ν. This procedure as been implemented in the Appendix C.

Without surprise, the corresponding equivalent elastic constants of the whole structure are the same as the laminated material. This comes from the fact that the employed material is isotropic. Nevertheless, for others applications, an isolating coating might be applied on the steel sheets in order to obtain better electric insulation. Glue might even be applied fulfilling both a fastening role and the electrical insulation. These components can change the global effective moduli. Lastly, the process of lamination can change the metal structural properties, and thus make the material anisotropic. Thus, the stacking of anisotropic material is actually changing the global properties of the ferromagnetic pole.

As a conclusion, the present searches aren't of much use in the case of dominant axial dimensions, that are more related to beam theories than lamination theories. Furthermore, with the hypothesis that the employed material is isotropic, the use of effective elastic constants isn't of much use either. This confirms the motivation of implementing a personal method in order to predict the deformations inside a laminated beam.

4.4 Magnetic gear parameters

Although the thesis focuses only on the pole pieces structure, it has to be implemented based on a complete magnetic gear application. The magnetic gear characteristics on which the modulating ring's resistance is investigated, has been worked out and provided by Pf. Dehez's PhD student, Christophe De Gréef. Who is actually working on finding a suitable solution of magnetic gear system for rail transport. A project leaded by Alstom^{TM}.

Below is exposed the provided parameters :

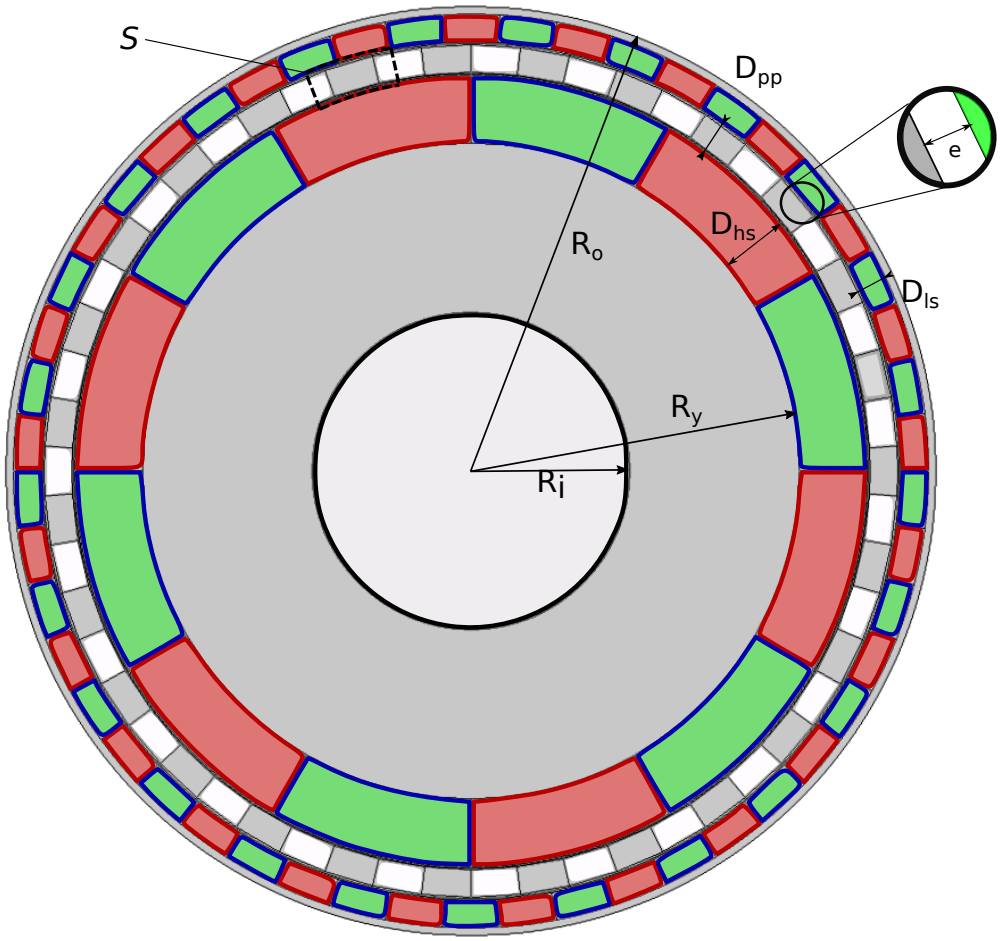

Magnetic gear parameters

$p_{hs}[\#]$	6	$D_{hs}[mm]$	32	$D_{pp}[mm]$	13
$p_{ls}[\#]$	25	$D_{ls}[mm]$	12	$t[mm]$	0.5
$n_s[\#]$	31	$e[mm]$	1.5	$\mu_r[-]$	1000
$R_i[mm]$	75	$L[mm]$	150		
$R_y[mm]$	155	$B_r[T]$	1.2		
$R_o[mm]$	220	$\alpha_s[-]$	0.5		

Table 4: Parameters

4.5 Ferromagnetic pole pieces parameters

The surface's section on which the modulating ring is investigated is represented in black dashes on the figure of table 4. The angular revolution of the surface represents a full ferromagnetic pole pitch, which is equal to $\theta_s = \frac{360}{31} = 11.61°$. This choice was motivated by the possibility to implement Periodic Boundary Conditions (PBC), in order to simulate the interaction of the section with the complete structure of the modulating ring.

The steel sheets that compose the laminated ferromagnetic poles, are held together, by two compressing rings. One is supposed to be fixed on the supporting structure and is considered to be encastred. The other compressor ring compresses the laminated poles by the means of screws and bolt, that encloses the ferromagnetic pole pitch (cfr. figure 51).

The geometrical parameters of the compressor ring and the laminated pole pieces are depicted in tabulars 5 and 6.

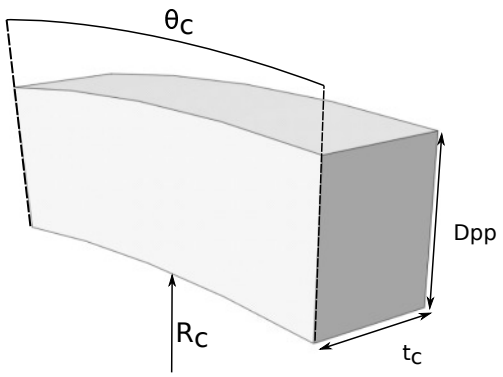

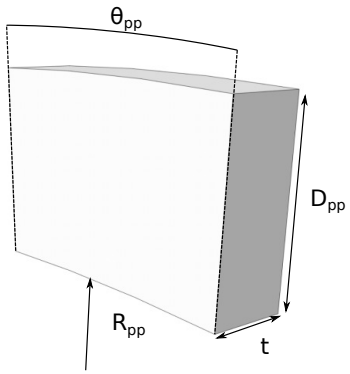

$\theta_c[°]$	11.61
$t_c[mm]$	10
$R_c[mm]$	188.5
$D_{pp}[mm]$	13
$S_c[mm^2]$	512

Table 5: Compressing ring section

$\theta_{pp}[°]$	5.8
$t_{pp}[mm]$	0.5
$R_{pp}[mm]$	188.5
$D_{pp}[mm]$	13
$S_{pp}[mm^2]$	256

Table 6: Ferromagnetic pole sheet

The stack lenght is $150[mm]$, thus the hypothetical number of laminated sheets, without considering the normal strain, is 300. The angular revolution of the compressor section fits the ferromagnetic pole pitch. The z-axis thickness has been chosen in order to have a low deformation induced by the bolt tensile pressure. And thus, being able to apply a sufficient compressive pressure on the laminated sheets. The laminated sheets have an actual thickness of $0.5[mm]$. Since the arc-pole factor of the pole pieces is 0.5, the angular revolution is half of the ferromagnetic pole pitch.

The assembled ferromagnetic pole pitch section, as implemented in 3D-FEM, is depicted in the following figure.

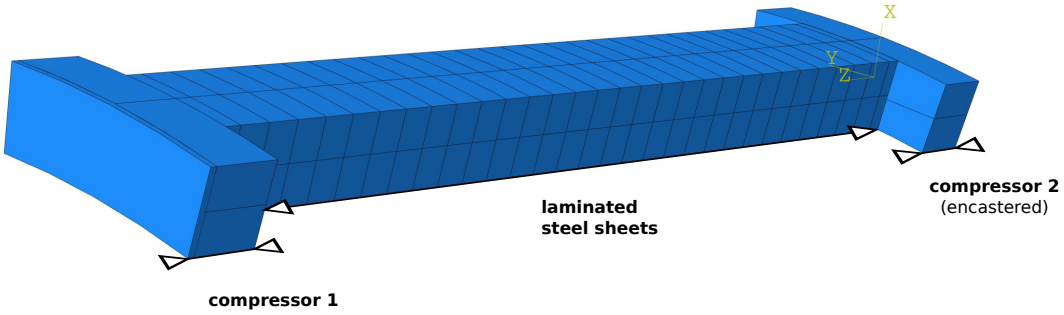

Figure 53: Ferromagnetic pole structure.

4.5.1 Section properties

The quadratic moments of the laminated pole pieces and the compressor rings are obtained via solidWorks^{TM}. The moment of inertia for the reference axis are depicted in the table 7.

	$I_{xx}[m^4]$	$I_{yy}[m^4]$	$I_{zz}[m^4]$
Pole-pieces	$3.333.10^{-9}$	$8.42.10^{-9}$	1.754^{-9}
Compressor ring	6.69^{-9}	$6.726.10^{-8}$	$7.395.10^{-8}$

Table 7: Section properties

We can make the assumption that the moment of inertia of the radial and tangential directions of the cylindrical coordinates, correspond to I_{xx}(resp.I_r) and I_{yy}(resp.I_θ).

4.5.2 Material properties

The materials that compose both the compressor rings and the laminated sections is industrial steel. In the ideal application, the compressing ring should have the lowest magnetic permittivity possible in order to reduce the end-effect, like high rigidity resin compounds made of glass fibers. However, in the context of the structural resistance interpretation, the only feature of interest of the compressing ring, is to have a high enough rigidity to apply a sufficient pressure without yielding. So the steel is a good material to fulfill this condition.

An other material is also commonly employed for the structure of the stator. It is liquid epoxy that is poured to fill the gap between the laminated ferromagnetic poles. Both of the material characterisitic are resumed in the table 8 .

Material	Density, $\rho[kg/m^3]$	Tensile Modulus, $E[GPa]$	Tensile Strength $\sigma[MPa]$	Poisson's ratio $\lambda[-]$
Industrial Steel	7.85	210	585	0.3
Epoxy resin	1.25	3.5	69	0.35

Table 8: Material properties based on [41]

4.6 Maxwell Stress Tensor

The magnetomotive force that experiment a geometric section inside a moving magnetic field, can be obtained by using the Maxwell Stress tensor. As expressed in [42], the integration of the Maxwell Stress Tensor over the laminate section is depicted in figure 54.

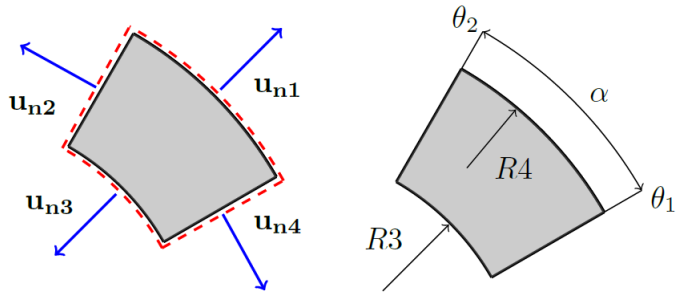

Figure 54: Pole pieces section, with the the surface of integration for the Maxwell stress tensor, which is the surface obtained by the extrusion in the z-axis of the dashed line.

$$\overrightarrow{F} = \oint_S \mathbb{T} \cdot \overrightarrow{n}\, ds \tag{18}$$

Where S, denotes the closed surface of integration, as accounted in [17] and is presented in figure 54. $\mathbb{T}$, is the Maxwell stress tensor. Which is expressed in the cylindrical coordinates as :

$$\mathbb{T} = \frac{1}{\mu_o}\begin{bmatrix} \frac{B_r^2 - B_\theta^2 - B_z^2}{2} & B_r B_\theta & B_r B_z \\ B_\theta B_r & \frac{B_\theta^2 - - B_r^2 - B_z^2}{2} & B_\theta B_z \\ B_z B_r & B_z B_\theta & \frac{B_z^2 - B_r^2 - B_\theta^2}{2} \end{bmatrix} \tag{19}$$

The radial and tangential components of the force are given by:

$$F_r = \frac{1}{\mu_0}\int_S \frac{B_r^2 - B_\theta^2 - B_z^2}{2} ds \tag{20}$$

$$F_\theta = \frac{1}{\mu_0}\int_S B_\theta B_r ds \tag{21}$$

The radial and tangential components of the force, for the investigated MG configuration, have been computed thanks to Virginie Kluyskens, researcher at the Catholic University of Louvain. Following the given parameters, the resulting force components that are acting on the ferromagnetic pole pieces, during the rotation of two inner rotor magnetic periods are depicted in the next figures.

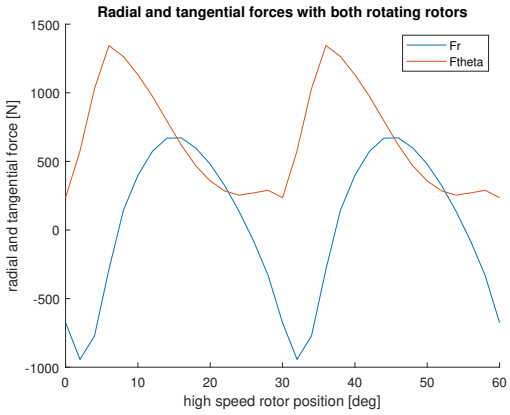

Figure 55: Radial and tangential force components. V. Kluyskens.

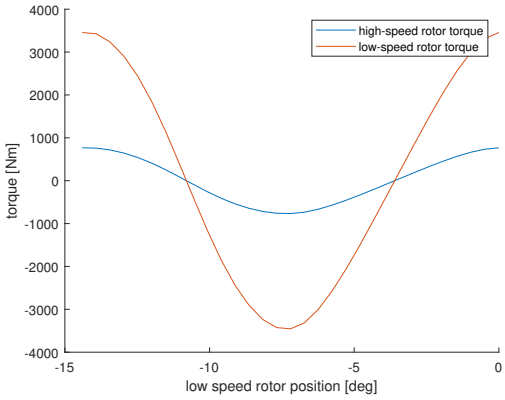

Figure 56: Global torque variation. V. Kluyskens.

We can see in figure 55, that the peaks are not in phase for the radial and tangential forces. The maximum peaks are $-943.262[N]$ and $1344,2[N]$ for the radial and tangential forces components.

The total torque variation over a single ferromagnetic pole by rotating the high-speed rotor has also been computed for the present magnetic gear configuration, and is depicted in the figure.57 :

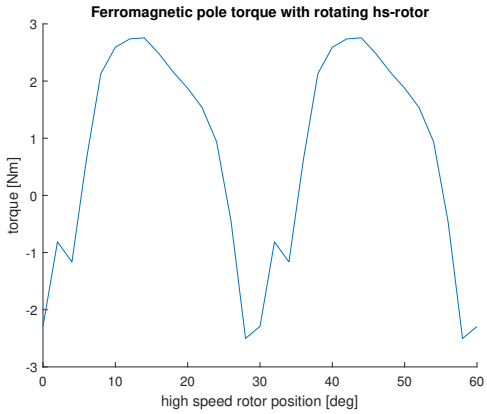

Figure 57: Ferromagnetic pole torque. V. Kluyskens.

We can see that the period of the torque function is $\frac{\pi}{6}$, which correspond to the number of pair of pole at the high-speed rotor, which is 6. The maximum torque applied to one ferromagnetic pole is $2.7560[N.m]$

In [17], the pole pieces are considered to behave like isotropic beams, since the axial length is predominant. Again, this is correct, if the assumption of perfectly cohesive contact (without friction or peeling off between the laminated pieces) is confirmed. In the case of [17], the beam is also assumed to be encastred at both ends. Then, the maximum displacement occurs in the middle of the beam and can be expressed as follow :

$$\Delta_{max} = \frac{w \cdot L^4}{384 \cdot E \cdot I} \tag{22}$$

where $w = \frac{F}{L}$, is the distribution force. Then it comes from (22), that the radial and tangential peak displacement located at the middle of the beam is :

$$\Delta_r = \frac{F_r \cdot L^3}{384 \cdot E \cdot I_r} \tag{23}$$

$$\Delta_\theta = \frac{F_\theta \cdot L^3}{384 \cdot E \cdot I_\theta} \tag{24}$$

It will be interesting to compare those results with the finite element method with the actual model of laminated beam. Furthermore, the authors themselves, encourage a further analysis by 3D-FEM to be carried on. The objective of the thesis is to respond with a well conditioned FEM model to precisely predict the static solid and kinetic deformations of the modulating ring.

5 3D - Finite Element Method

At first, the 3D-FEM was implemented in Comsol Multiphysics, which was the selected software to work with in the context of magnetic circuit analysis. The software, although it is well suited to work with magnetic fields, showed quite quickly the limits of the included features to work with solid materials, especially to implement contact surfaces. The magnetic gear model and the first implementations of the laminated beam can be found in Annexe A.

In order to find a better way to implement the contact surfaces, advises from the UCL professor Issam Doghri, has been asked and given. He encouraged the use of the software Abaqus^{TM}, which provides much more features to modelize solid physics and is also much more optimized for the finite element calculations.

Nevertheless, since no real known similar model has been implemented to date. This was a total venture, trying to find the just compromises between the possibilities of FEM using Abaqus^{TM}, and the real application exigences.

5.1 Model description

The geometric parameters are described in the previous section, as well as the initial hypothesis of the problem. With the simplified problem(fig. 52), the hypothesis and the geometric parameters (tab. 4-6) . The 3D-FEM model has been implemented,

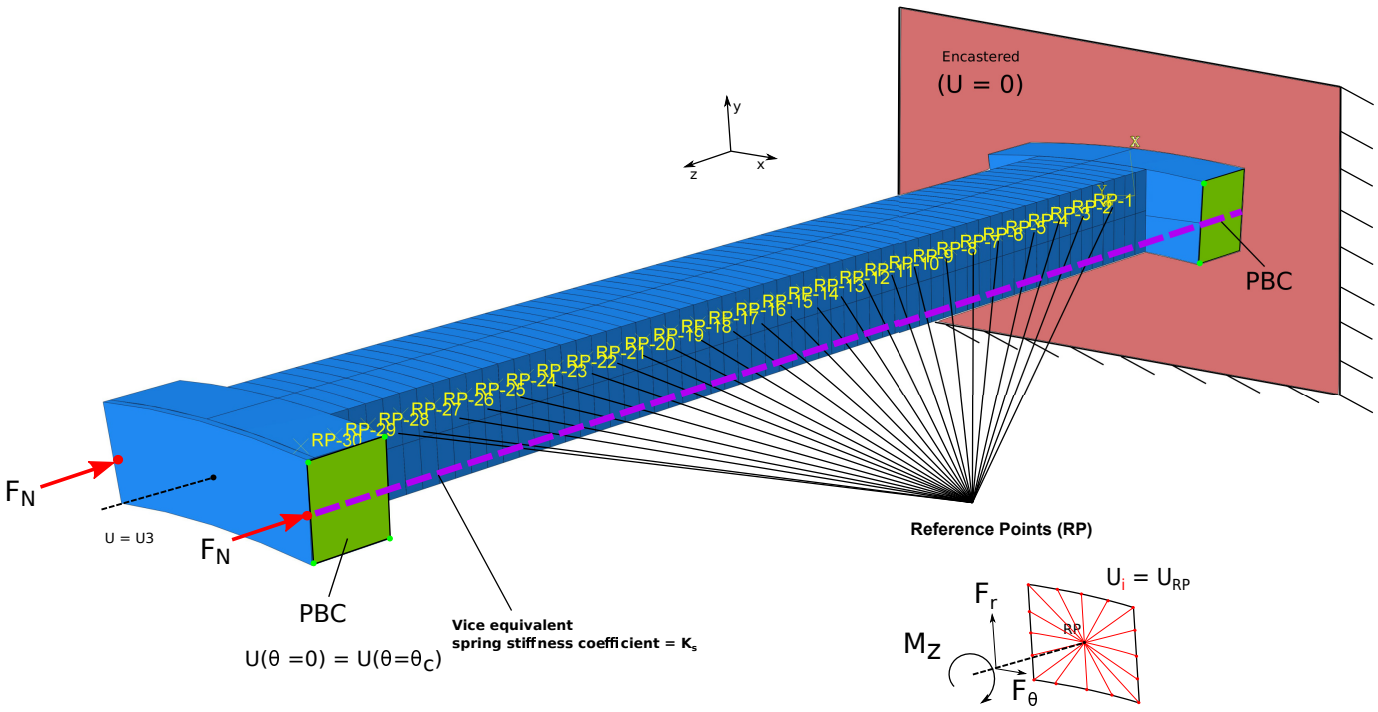

Figure 58: Finite Element Method, based on the simplified model.

5.1.1 Boundary Conditions

In order to have a well-conditioned problem, with a finite element method that computes easily the wanted results, a series of Boundary Conditions(BC's) had to be instanced.

The first BC to be implemented, is the encastered surface of the second compressor ring($U = 0$). It is considered as the reference, since it is more likely to by built-in in the supporting structure.

Secondly, the PBC's at the adjacent surfaces are implemented by the way of conditioning equations. Which in abaqus is defined as follow :

$$C_1 \cdot U_{k,left} + C_2 \cdot U_{k,right} = 0 \tag{25}$$

$C_{1,2}$ are the weighted coefficients, and thus, $[C_1 = 1, C_2 = -1]$
k is the spacial degree of freedom $(1 = x, 2 = y, 3 = z)$, then $k = [1; 2; 3]$
The designations "$left-right$" are the correspondent points in the radial and axial directions for which $\theta = [0(left); \theta_c(right)]$.

From this, a system of 3 equations is created for each selected point. Considering that the material is quite stiff, and that each of the PBC's are to be computed by hands, it is the choice of the simplest and most efficient way that prevailed. So, the chosen application points are the 4 corners on both sides. The constraints applied on such small surfaces, are believed to render a sufficiently precise version of the real application.

The last BC the be implemented, is the imposed axial movement of the center point of the moving compressor ring. It might not be completely founded by the real behavior of the model, although the radial and tangential movement are supposed to be negligible compared to the axial one, due to the action of the vices on the whole structure. But still, it simplified the computation process, which granted us noticeable time for more important matters of the problem. Which are the contact surfaces and are explained in the following section.

5.2 Contact surface

Since the contact surface is certainly the one most important component of the thesis, the implementation of the parameters which rules the contact behavior is crucial. Thus, this section will cover the main options that were available in order to simulate the contact interfaces.

5.2.1 Master - slave interaction

In Abaqus, the surface can be implemented with many ways, including the "general contact surface" which take all surfaces into account and find which ones are actually in contact. This contact is easily defined, but the computational cost is important. the most efficient is the "surface-to-surface" contact, where contact-pairs are defined. So, the calculations, only focus on the predefined surfaces.

The contact pairs always include a "Master-surface" and a "slave-surface". The master surface's nodes are allowed under heavy contact pressure, to penetrate the slave elements. But this phenomenon is reduced to the minimum in the calculations. The phenomena are depicted in figure 59.

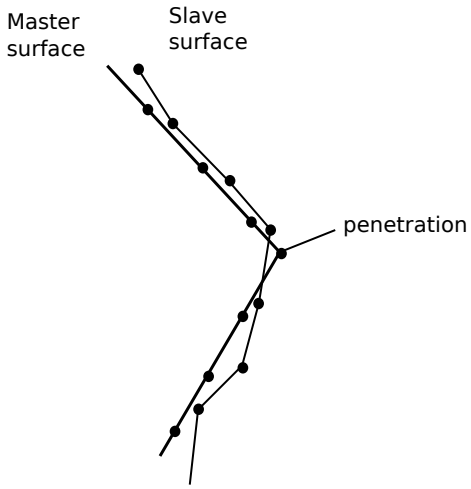

Figure 59: Master-slave interaction

The Master surface is generally the stiffer one, but in the actual case, all the parts of the structure is composed with steel of the same rigidity modulus ($E = 210[GPa]$). The Master surfaces are thus the two compressors plus half of the laminated surfaces and are distributed evenly through the laminated structure. This definition, under reasonable constraints, shouldn't show noticeable consequences over the results.

5.2.2 Normal Behavior

When two plane bodies are in contact, they will apply on each other a normal force $\overrightarrow{N}$ at the interface, which will create a friction force between them, depending of the intensity and the friction coefficient μ_s.

$$\overrightarrow{F_{frict}} = \overrightarrow{N} \cdot \mu_s \quad [N] \tag{26}$$

The normal force when applied on a surface A, is also called contact pressure, which is denoted as

$$P_{contact} = \frac{N}{A} \quad [Pa] \tag{27}$$

The contact pressure in the case of "Hard" contact, is transmitted instantaneously and homogeneously when the two bodies reach each others. In the real application, this contact method might be considered more relevant, especially when the right stiffness factor is featured with it. However, even though the hard contact is to be preferred for precision, this method as a higher computational cost since the contact pressure is instantaneous when the contact happens. Furthermore, important stress steps with sudden increase of pressure have been encountered with this method, which yielded into important deformations.

A second option is to implement a smoother relation between the contact pressure and the clearance between the two surfaces. This is called the "soft contact" method. Instead of applying a step pressure when the contact occurs as with the hard contact method, the step is smoothed by fitting an exponential function. This can be achieved through tabular,

linear or exponential functions. This also means that pressure is occurring at the interfaces while the contact has not happened yet. The exponential fitting function represent the best compromise between having the most real-like relation and numerical complexity. Indead, by selecting a very small zero-pressure value, and a large zero-clearance pressure, the pressure before the contact is very small and the prenetration pressure is very high.

In the current numerical method those values have been chosen through trials and are $0.01[mm]$ and $100[MPa]$. This allowed the reduction of computing time from several hours to a few dozens of minutes.

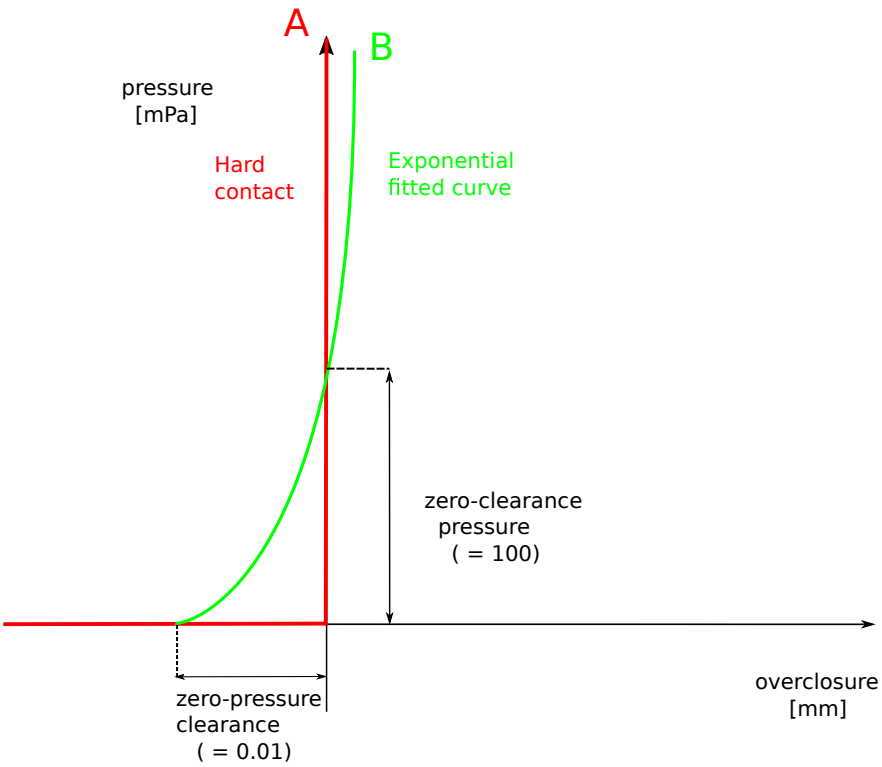

Figure 60: Pressure-overclosure relation

5.2.3 Friction model(Tangential behavior)

As for the normal behavior, Abaqus has many features concerning the frictional behavior implementation.

The first one to be used, and certainly the most conventional one, is the simple "Penalty" method, based on the Coulomb friction, for which the friction coefficient is manually computed and defines the relationship between the shear stress transmitted at the interface and the contact pressure. As the contact pressure rises, the allowable shear stress transmission without falling into the slip region increases too. This relation is correct while the material sustains only elastic deformations. When the pressure exceeds the elastics deformation tolerance, the materials yields into plastic deformation and cannot apply additional contact pressure. This is why a maximum transmitted shear stress τ_{max} is defined. A good approximation for this value is $\frac{\sigma_y}{\sqrt{3}}$. In the case of steel, this value is estimated at $\tau_{max} = 448[MPa]$. The equivalent elastic slip can also be personally defined, but having insufficient knowledge on this area, the default settings(0.5%) have been kept. The friction coefficient has been

found in [41] and is equal to 0.73 . The Coulomb contact paramters are summarized in the following table.

Static friction coeff. $\mu_s[-]$	slip rate ratio [%]	Maximum shear stress transmission $\tau_{max}[MPa]$
0.73	0.5	448

Table 9: Caption

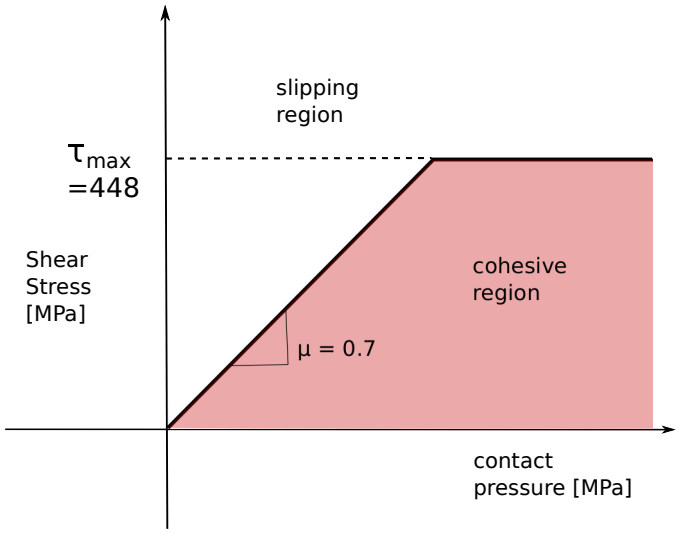

Figure 61: Cohesion curve

The second implemented contact method is the formulation of a relation between the static friction coefficient and kinetic friction coefficient. This method follows the same principle of the first but instead of having a step between the static and kinetic coefficients(which are defined as the zero-slip rate and maximum slip-rate, with no transition), the static and kinetic coefficient can be defined for intermediate values. These values are obtained by fitting an exponentially decreasing curve. The elastic slip is the same as the previous model, but the decay coefficient "d_c", is added to modulate the swiftness at which the kinetic friction coefficient is reached. This coefficient has been setted out to 10^3, in order to have a instantaneous-like behavior. This implementation, might show quicker computation time, in the case of severe slip. Nevertheless, this should not be the actual case.

The chosen values of the static and kinetic friction coefficients are obtained from the "Handbook of physical quantities"[41].

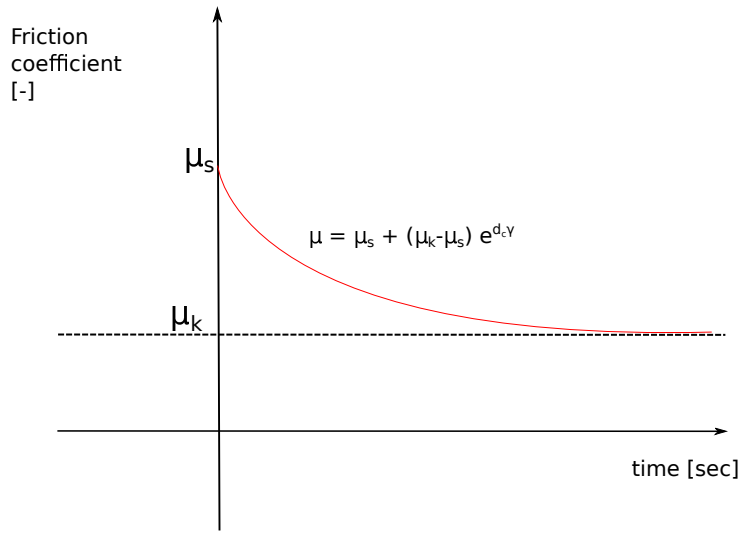

Figure 62: Static-Kinetic transition funtion

Static friction coeff. μ_s	Kinetic friction coeff. μ_k	Slip rate ratio [%]	Decay coefficient [−]
0.73	0.57	0.5	10^3

Table 10: Static Kinetic contact method properties

After some trials in comparison with the first method, the results difference between the two method, seemed to be negligible while maintaining the contact. Which is of course predictable since the static behavior is supposed to be the same as the Penalty method. Therefore, the following trials will carry on with the Penalty method to characterize the contact behavior.

One last contact interface has been implemented, which is the Rough method. This contact ensures no slip nor friction($\mu_s = \infty$) once the surfaces are in contact. This method is important to serve as a reference in order to evaluate the numerical errors during the computation of the total slip angle. In other words, this contact will be employed to validate the hypothesis of perfect cohesive contact and equivalent homogeneous beam.

5.3 Force and contact interfaces distribution

The contact has been defined and implemented, the geometry as well as the boundary conditions have also been setted out. In order to achieve the final model and go on with the trials, the final parameters left open are the stacking sequences and the force distribution implementation.

The force distribution, as seen in the previous sections, can be approximated by a homogeneous distribution alongside the z-axis, due to the axial symmetry. This is a relatively good approximation except if the end-effect is important(i.e, very short magnetic gears).

But, with the Abaqus interface, the force cannot be expressed as a constant field throughout the axial length, but must be applied on a discrete set of points. These points, also called "Reference Points"(RP), can further be linked to other set of points composing the

longitudinal plan(z-normal axis) on which the reference point is located. This by imposing a movement constraint. This method is depicted in figure 58 and 63. With this method, each point composing the plan are constraint to have equal displacements to those of the RP. Thanks to the high rigidity of the material, the force is efficiently transmitted trough shear stress. Therefore, this method is assumed to be the closest possible from the reality with the means proposed by Abaqus^{TM}.

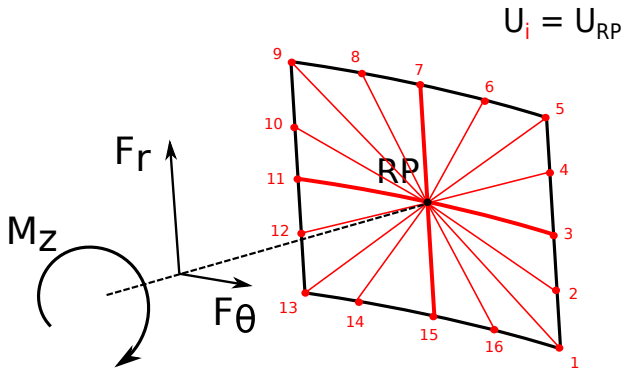

Figure 63: Force application on a section of the pole piece.

The discrete force applied on each RP's is then expressed as follow:

$$F_{rp} = \frac{F_{tot}}{N_{rp}} \tag{28}$$

With F_{tot} the force integrated over the whole length of the structure, provided by Virginie Kluyskens. And N_{rp}, the number of evenly distributed Reference Points.

The laminated ferromagnetic pole, on its part is the stacking of steel sheets that have in the ideal scenario, the thinnest thickness possible to short circuit the eddy-current. For a reasonable application, this thickness is agreed to be fixed at $0.5[mm]$. However, in the context of the 3D-FEM study, to obtain the wanted stack length of $150[mm]$, the number of sheets should rise up to 300(without considering the normal strain). Since each laminated steel sheets are hand-computed and that each contact interactions increases the non-linearities of the global model and thus the computational cost, the number of possible stacks must be revised downward.

This is why in this thesis, we will try to predict the evolution of the "effective homogeneous beam" behavior while increasing the number of stacks, in order to make realistic assumptions on the real stack number. The first model, composed of one $150[mm]$, is a regular homogeneous beam and will serve as reference for the rest of the study(fig.64).

After this choice, some trials with random numbers of stack and reference points have been made. From those trials, came some observations. First, when distributing evenly both the separation interfaces and the discrete force distribution (RP), in some configurations, the reference points and the interfaces meet up and the same plan in some at some points. Although the magnetomotive force is also present at the interfaces of the stacks, it is an infinitesimal part of the total force involved in the ferromagnetic pole, since it is distributed on a continuous basis. But when the force is discretized, the portion of the total force present

on each RP is more important. Thus, applying an important part of the total force, directly on the contact plan, might increase severely the shear stress at the interface. This might cause to prematurely reach the maximum shear stress and topple into sliding mode.

The best found way to ensure that contact surfaces and reference points will never meet up, without changing the force distribution, and having different number of stack of the same length, was the use of a Lest Common Multiple(LCM) method. After a quick calculation, the number of 30 RP's and contact surfaces, showed a large panel of possible combinations, while keeping steady distribution specifications. By means, an equal force distribution through the different models, and a force application at a "safe" distance from the contact interface. This method is depicted in the figure 64.

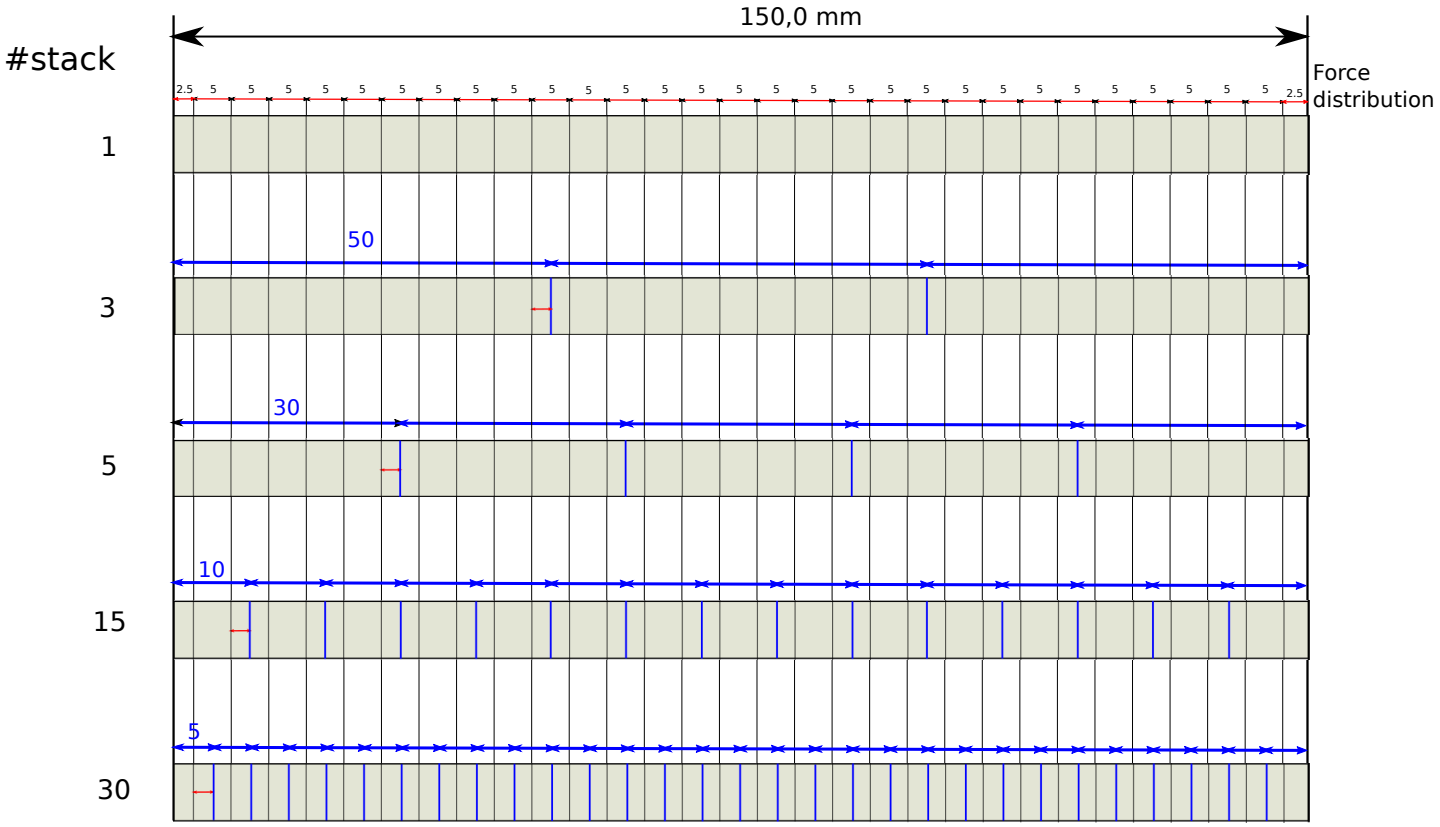

Figure 64: Force and contact distribution as implemented in the 3D-FEM.

As we can see, the closest distance between the contact surface and the force application, shown in red in figure 64, is constant for each stack sequences. The chosen numbers of stacks are therefore $N_s = [1, 3, 5, 15, 30]$ and the number of reference points(force application) $N_{RP} = 30$.

5.4 Resolution method

The first resolution method that was selected, was the Standard Static implicit method, which uses an implicit method of iterations to resolve the mechanical equations and converge toward the final values, when an acceptable level of error is reached. However, the first tests with 10 interfaces revealed that the non-linear character of the contacts and the accumulation

of the number of contacts was challenging for this resolution method. Finding a convergence took several hours of computation time. That is why, with the consultation of Pf. Doghri, in order to improve the calculation efficiency, the decision to switch to an explicit Dynamic method has been made. This method resolves the mechanical equations over a small time-step, that is specified by the user and carries on the calculations through the final time-step.

This method implies several other choices to be taken. At first the time step, which should be the smallest possible in order to reduce the time calculation, but also large enough to allow the system to reach a steady state. Secondly, since the method is now dynamic, a "procedure" separated in two successive steps. In order to simulate the preconstraint -which is the initial compression of the compressor rings- the first step, is the compression phase. The pressure is gradually applied on the compressor ring at two edge points, which are the locations on which the two virtual screws and bolts are placed. When the first step is stable, the torsion phase begins with also a gradual application of the constraints inside the laminates. When the whole system is stabilized, the results can be checked and post processed.

This method showed it's better adaptation to resolve the non-linear problem of the contact surfaces, with smaller computation time, and stable results at the end of the computations.

6 Results

6.1 Equivalent Spring stiffness

The laminated stack in the stator is held by tensed steel rods, or more simply vices and bolts(see fig.51). The screws are represented as simple springs, with a rigidity coefficient k_s. The value of the initial length of the spring being not allowed to be defined at a wanted value(link between two nodes), other methods of defining the equivalent spring stiffness to have an equivalent contact pressure for every model have been implemented .

First, The equivalent spring stiffness can be deduced from Hooke'slaw, relying the stiffness of the material and it's deformation rate under a certain constraint.

$$\begin{aligned} \sigma &= E \cdot \epsilon \\ \frac{F_n}{A} &= E \cdot \frac{\Delta x}{x_0} \\ F_n &= \frac{E \cdot A}{x_o} \cdot \Delta x \\ F_n &= k_s \cdot \Delta x \end{aligned} \tag{29}$$

We see then that the equivalent stiffness of the screw, grows quadratically with the screw's radius ($A = \pi r_v^2$). The choice of the radius depends on the available space in the gaps between the steel plots. It also depends on the weight limitations, since the volume, and thus the weight also goes quadratically with the screw's radius. The maximum space available in the gaps for the present model as shown in table 4.4, is $((R_{pp} + D_{pp}) * \theta_{pp} = 19.6[mm])$. Thus the upper limit of the diameter of the screw is about $18[mm]$. Table 65 sums up the equivalent spring stiffness for divers steel screw diameters.

$\emptyset[mm]$	3.5	5	7.5	9	11.5	13	15.5
$k_s[N/mm]$	$1,34.10^4$	$2,75.10^4$	$6,16.10^4$	$8,9.10^4$	$1,45.10^5$	$1,858.10^5$	$2,64.10^5$

Table 11: Equivalent spring stiffness for vices diameters

As seen previously, the introduction of a soft contact interface between the laminated steel sheets, implies a non-zero contact pressure while the sheets are not in contact yet. This can be understood as a "spring interface", while the clearance goes thinner, the contact pressure increases. The pole pieces can therefore also interpreted as springs of rigidity coefficient k_{pp}. Even if the contact conditions are the same for each model (resp. homogene, 3 laminates, 5 laminates, etc), the number of interfaces will influence the "equivalent local spring" for small compression regions, then the normal displacement under the same applied force. The equivalent spring stiffness of the different plots are obtained by imposing a normal force step of $10[kN]$, and analysing the resulting displacement.

$\#laminates$	1	3	5	15	30
Δx	0.03	0.0375	0.045	0.0799	0.1212
$k_{pp}[N/mm]$	$3,33.10^5$	$2,66.10^5$	$2,22.10^5$	$1,25.10^5$	$8,25.10^4$

Table 12: Equivalent spring stiffness for the laminated plots

Therefore, in order to have the same equivalent force applied on the plots, the applied force on both edges(resp. the vices points) can be expressed as follow :

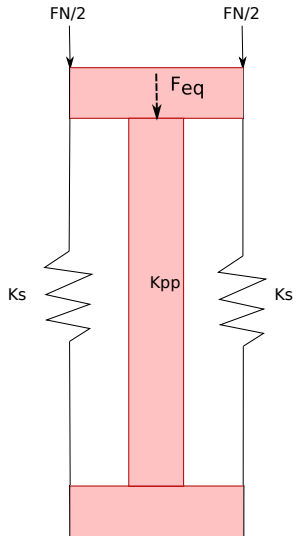

Figure 65: Equivalent force applied on the plot

With the hypothesis of a constant rigidity coefficient for the pole pieces, and small bending for the compressing ring. Those rather weak hypothesis, considering that a part of the stiffness comes from "non-linear springs" at the interfaces and that the compressing ring is made of the same material then the laminated sheets.

The force to be applied, in order to obtain the same equivalent normal force at the plots, is then found :

$$\begin{aligned} F_N &= \Delta x_{tot} \cdot (k_{pp} + 2.k_s) \\ F_{eq} &= \Delta x_{tot} \cdot k_{pp} \\ F_{eq} &= F_p \cdot \frac{k_{pp}}{(k_{pp} + 2.k_s)} \end{aligned} \tag{30}$$

From this, we can choose the equivalent force and then compute the force to apply on both ends of the compressor.

The maximum contact pressure is known and is equal to :

$$p_{max} = \frac{\tau_{max}}{\mu} = \frac{\sigma_y}{\mu\sqrt{3}} = 640[mPa] \tag{31}$$

A good base value for the applied pressure, would be around one tenth of the maximum pressure.

Therefore we can find the normal force F_N to be applied in order to a contact pressure $p_{contact}$.

$$F_N = \frac{p_{contact}}{A} \frac{k_{pp} + 2.k_s}{k_{pp}} \tag{32}$$

In the case of the thesis, the base value of the normal force has been chosen at $10[kN]$. This corresponds to a contact pressure of $59[mPa]$ and is believed to be high enough to generate sufficient contact pressure and thus shear stress transmission capability to evaluate the beam for reasonable torsion levels. All this while staying relatively far from the value of the theoretical maximum shear stress transmission, and thus avoid the plastic deformations which would alter the wanted results.

In order to have more dominant linear component of the global stiffness, the chosen dimension of the screw is chosen at about half of the gaps, and is $11.5[mm]$. Then we can compute the equivalent stiffness ratio and the force to be applied in order to find the wanted contact pressure.

$\#laminates$	1	3	5	15	30
$\frac{k_{pp}+2k_s}{k_{pp}} = k_{eq}[-]$	1.87	2.09	2.30	3.32	4.53
$F_N\ [kN]$	10.01	11.3	12.4	17.95	24.4

Table 13: Resulting normal force

It seems evident that the more the local equivalent stiffness of the laminated structure induced by the contact surfaces is soft, the more the importance of the spring.

However, the results from this first method showed import differences in the contact force, and thus in the contact pressure. As shown in the following figure.

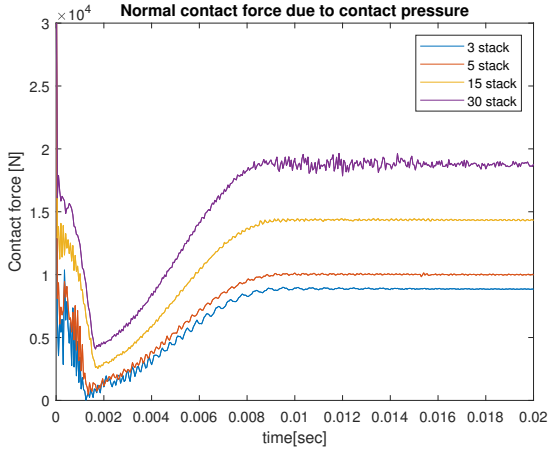

Figure 66: Normal force calculated on the top laminate surface

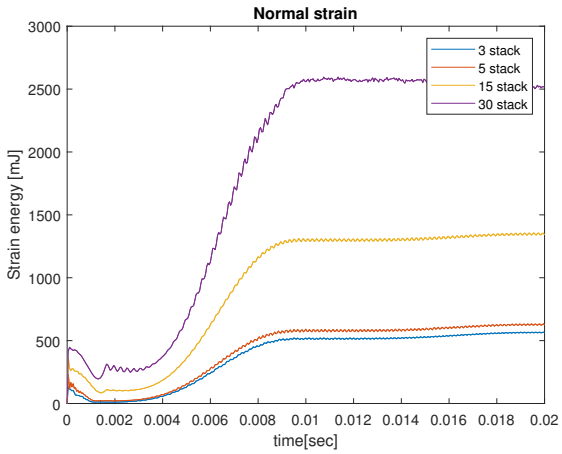

Figure 67: Strain energy on the whole structure

It is clear that the method of constant rigidity coefficients is not suited for the prediction of the normal force in the model. This come actually from the fact that the initial "effective length" of the structure is more than 150[mm], due to the contact specifications. Indeed, at the beginning, the stacks repeal each other due to the contact heavy contact pressure at zero-clearance. This phenomenon occurred as a big "bounce" at the start of the simulations and occasionally made this model unstable with important axial movements.

To counteract this phenomenon, a "damper" stack is applied at the beginning of the simulation, in order to contain the stacks while the compression is not acting yet. Boundary conditions imposing no normal displacements have been tried in the first place, but the stress jump at the release was too important and caused distortion errors. The effect of the damper is visible in the beginning of the upper-shown graphs, by an important jump of the internal constraints. These constraints smoothly vanish while the damper is slowly removed and the pressure applied by the compression ring gradually rises.

A second method was employed in order to find the right amount of compression to exert with the presence of spring of equivalent stiffness. The method is the following: For a given load on the application point of the compressing ring, the displacement amount for each stack models will be different. Thus, for a given contact force applied at the interfaces, the "free displacement" Δx_f, will be different. In order to find an equilibrium with action of the springs(resp. the bolts), an equivalent offset force will have to be applied to counteract the spring force for the given free displacement.

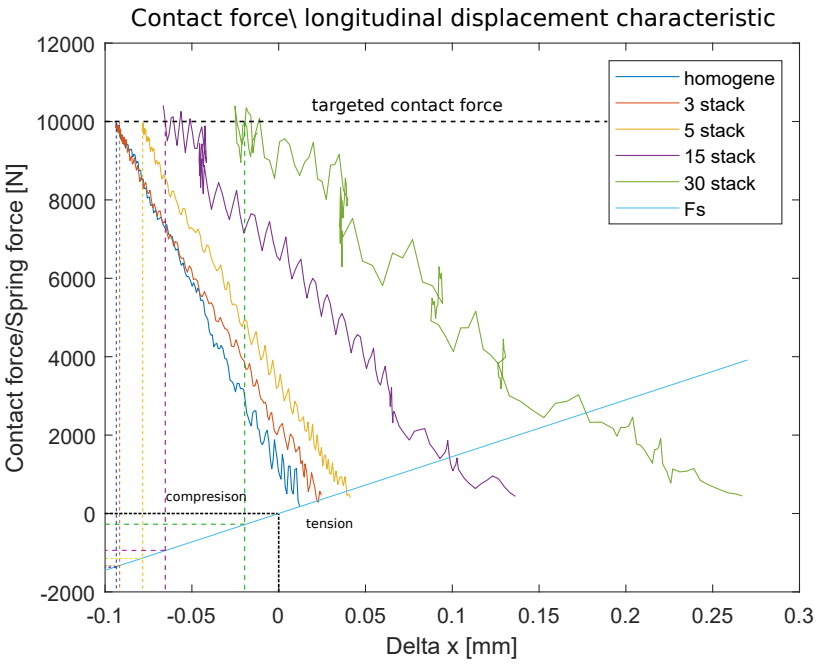

Figure 68: Normal displacement for an equivalent contact pressure application.

From figure 68, we can see that under a certain contact force, the sign of the compensation force to be applied becomes negative. This is from the fact that the spring are actually pulling back. A second observation, is that the rigidity of the models seems actually relatively linear, which validate in some ways the first method of the equivalent springs. The point that

invalidates the first method is the push-pull crossover, and the virtual initial length that is different for each model.

$\#laminates$	1	3	5	15	30
$\Delta x_f[mm]$	-0.09578	-0.0987	-0.081988	-0.0606	-0.0142
$\Delta F_s[kN]$	1.388	1.431	1.188	0.878	0.2059
$\frac{F_N}{2}[kN]$	6.388	6.431	6.188	5.878	5.2059

Table 14: Spring force compensation

As shwon in figures 69-70 ,the obtained results with this method are greatly improved.

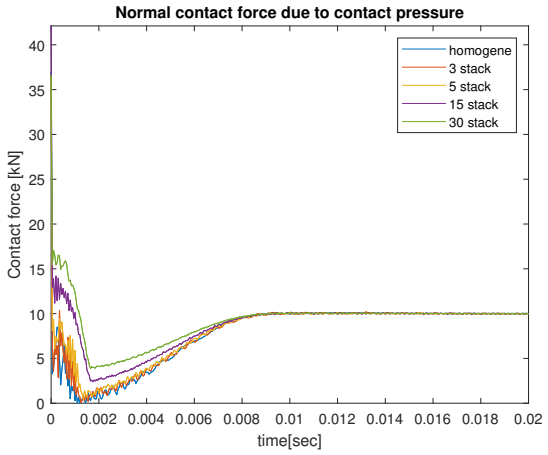

Figure 69: Normal force calculated on the top laminate surface

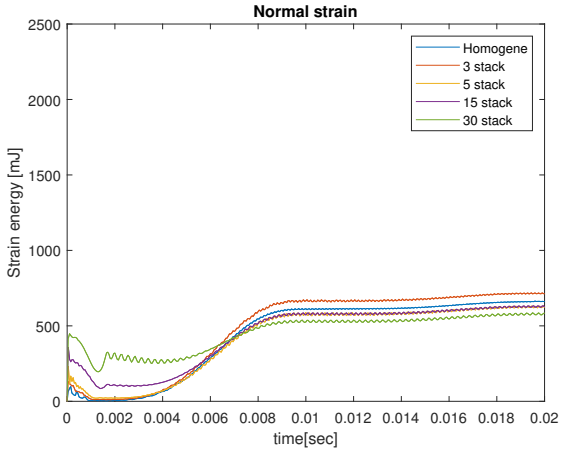

Figure 70: Strain energy on the whole structure

Indeed, the target contact force ($F_N = 10[kN]$)is almost perfectly reached. The strain energy remains however slightly variable for the different models. This difference may come from the different applicated force at the compressing ring in order to obtain an equivalent result in the laminated section. This assumption is not verified, since the important part of the model is still the laminated section.

6.2 Torsional twist, no-slip region and equivalent beam validation

In the previous sections, several contact methods have been presented. Among which the Penalty contact method(defined with a friction coefficient ,μ_s), which is the most commonly used to model friction contact. An other method is also available, which involves a virtual infinite friction coefficient, in other words, the contact surfaces are sticking to each other independently from the applied load. To perform the torsion test on the laminted beams, the applied torque as been increase of equal steps and the final steady torsional angle as been encoded.

The applied torque is for the test is shown below :

$$T_{RP} = [1, 1.25, 1.5, 1.75, 2][N.m/RP] \tag{33}$$

$$T_{tot} = 30 \cdot T_{RP} = [30, 37.5, 45, 52.5, 60][N.m] \tag{34}$$

We can remind that the amplitude scale of the applied torque is chosen much bigger than the actual torque endured by the ferromagnetic poles(cfr. Maxwell Stress Tensor). This, with the purpose of minimizing the effect of the vibrations since the measurement with the real torque were very small. During the first trials, as seen in figure 71, the torsion with the penalty method seemed to be linearly increasing with the number of stack partition of the model. Even for small load which didn't overcome the maximum shear transmission allowed. Since small displacement are allowed with the penalty method, even for small loads, this didn't seemed irrelevant at first. But after some trials with the Rough method, these same linear increments appeared with the growing number of stacks. The following ascertainment has been drawn from this observation: the displacement difference between the different models under the assumption that the slip is null, comes from numerical distortion due to the normal contact behavior implementation (cfr. Normal behavior).

Since the normal behavior implementation is the same between the Penalty and the Rough method, the hypothesis that the magnitude of the numerical distortion is the same for both models. Thus, this error can therefore be subtracted from the Penalty model to obtain the actual angle due to the slip.

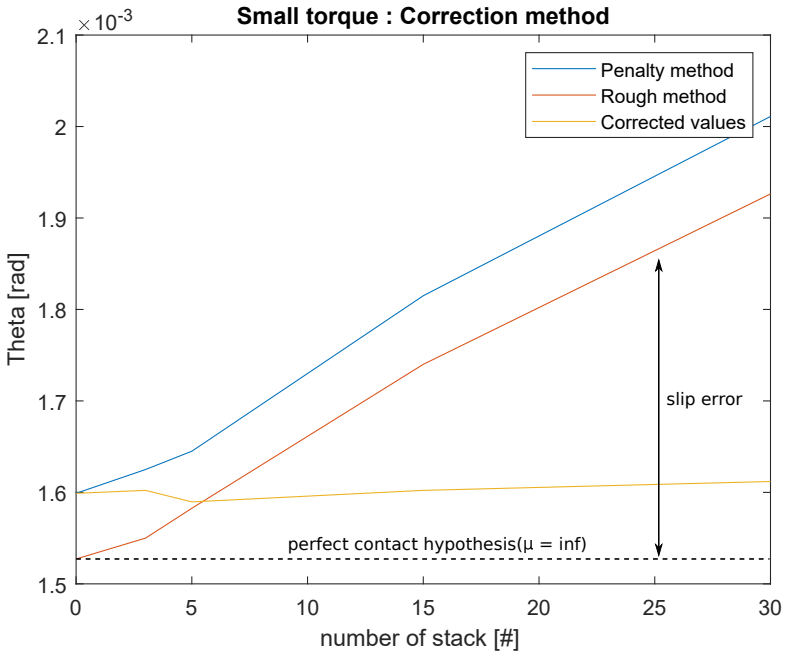

Figure 71: Correction method

The linear behavior of the error can be observed in figure 71. The correct result of the Penalty method is constant through the laminate number variation, as it is to be expected for small loads. The actual slip angle is therefore the difference between the Penalty method and the Rough method.

$$\Delta e_i = \Delta\theta_{Rough,i} - \Delta\theta_{Rough,1} \tag{35}$$

$$\Delta\theta_i = \Delta\theta_{Penalty,i} - \Delta e_i \tag{36}$$

$$\Delta\theta_{slip,i} = \Delta\theta_{Penalty,i} - \Delta\theta_{Rough,i} \tag{37}$$

With $i = [1, 3, 5, 15, 30]$ the stacking sequence, Δe the distortion error due to the normal behavior, $\Delta\theta$ the total torsion angle and $\Delta\theta_{slip}$ the angle due to the slip. Sometimes, the stacking number "1", is also referred as "hom" for homogeneous. This procedure is then iterated for different values of torques, in order to evaluate the corrected curve of the angle variation alongside the torque.

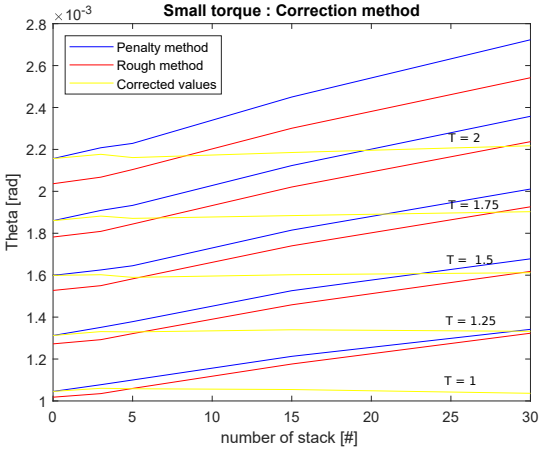

Figure 72: Correction method for different values of torque.

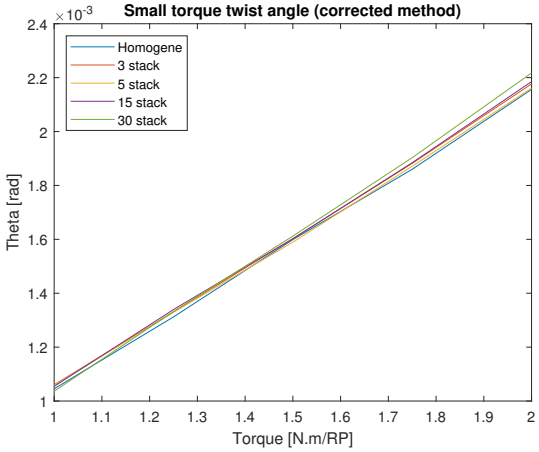

Figure 73: Corrected torsional angle variation with axial torque.

The results are summarized in table 15 and 16:

$T_{RP}[N.m/RP]$	1.0	1.25	1.5	1.75	2.0
$\Delta\theta_{hom}[rad.10^{-3}]$	1.0	1.3	1.6	1.9	2.2
$\Delta\theta_3[rad.10^{-3}]$	1.1	1.3	1.6	1.9	2.2
$\Delta\theta_5[rad.10^{-3}]$	1.1	1.3	1.6	1.9	2.2
$\Delta\theta_{15}[rad.10^{-3}]$	1.1	1.3	1.6	1.9	2.2
$\Delta\theta_{30}[rad.10^{-3}]$	1.0	1.3	1.6	1.9	2.2

Table 15: Torsional twist angle after the correction method

$T_{RP}[N.m/RP]$	1.0	1.25	1.5	1.75	2.0
$\Delta\theta_{slip,hom}[rad.10^{-5}]$	2.74	3.99	7.18	7.8	11.9
$\Delta\theta_{slip,3}[rad.10^{-5}]$	4.24	5.8	7.5	10	14
$\Delta\theta_{slip,5}[rad.10^{-5}]$	4.02	5.7	6.24	8.9	12.4
$\Delta\theta_{slip,15}[rad.10^{-5}]$	3.65	6.72	7.5	10.2	14.9
$\Delta\theta_{slip,30}[rad.10^{-5}]$	1.85	6.0	8.47	12.1	18.1

Table 16: Slip angle based on the correction method.

6.3 Stall region

It has been seen in the previous section, that laminated beams can be approximated as homogeneous beams in the cohesive region. However, the laminated beams could be more likely to slip under more important torque loads. In this section, the stall behavior of the different models has been computed and analyzed to try and give an answer. To try and understand this phenomena, the frictional energy, that is homologous to the slip level, has been measured on the first contact interface betweent the compressing ring and the laminated section.

From figure 74, we can see that the measured frictional energy, stays almost constant till a certain value of torsional angle. Then the ferromagnetic pole falls into the slip region with an intermediate state that is the transient region. We can also observe that this angle is not noticeable difference from a model to an other, that also consolidates the equivalent beam theory.

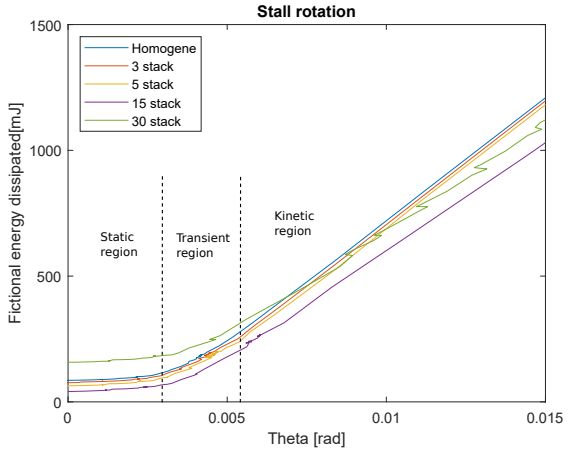

Figure 74: Frictional energy in function of the torsional angle.

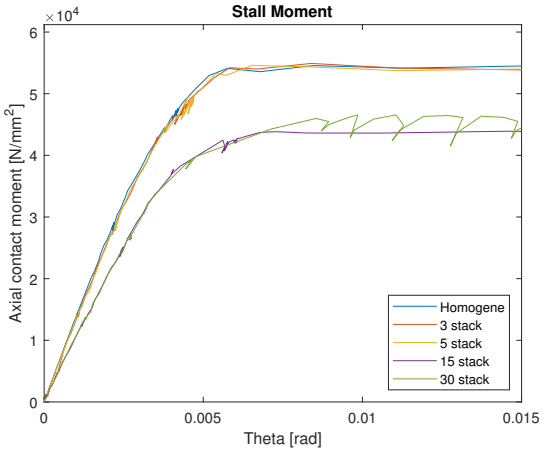

Figure 75: First interface axial shear moment in function of the torsional angle

The difference in $(\theta = 0)$, comes from the set up of the stacks that generates an "off-set" frictional dissipation. The important value is the slope of the frictional energy in function of the torsional twist angle θ. The slope is also equal to the gap spacing rate between the Penalty angle and the Rough angle in figure 72.

However, we can see that the maximum reached moment before entering the slip region for the $15 - 30$ stacks models, is not as high as the for the lower-stack models. This is explained by the fact that This is explained by the fact that is the second closest laminate to the compressing ring that stalls in the first place.

These results are useful mainly to compute the maximum moment that can be handled by the interfaces before breaking into the slip region. This with the purpose to eventually assemble a modulating ring with the minimum supporting structure possible, since it adds up on the total weight. This might be useful essentially for high performance magnetic gears.

Magnetic gears without supporting structures for the modulating ring have already been constructed (**ref**), but in those configurations, the modulating poles were composed of simple

steel bars. This represents an important source of losses. If the reason of using such beams were the questioning of the structural integrity, the presented computation procedures can brought answers to this problem.

6.4 Transient region, stack influence

The two sections above showed that no noticeable differences exists between laminated beams and simple uniform beams in the stick region and the slip region. Indeed, while the applied torque increases, the slip angle remains constant for the different models. However, we also have seen that an intermediate state exists between those two regions. This region is characterized by the limit of the sticking region and the occurring of important slips. If the torque is further increased, the slip becomes predominant the difference between the models becomes again negligible.

The slip angle as also been computed for the small slip region, those are depicted in figures 76 and 77. In the first one, we can notice that for the lower torque values, the difference between the different stacking models isn't noticeable yet, which is understandable since the the slip angle is small compared to the torsion

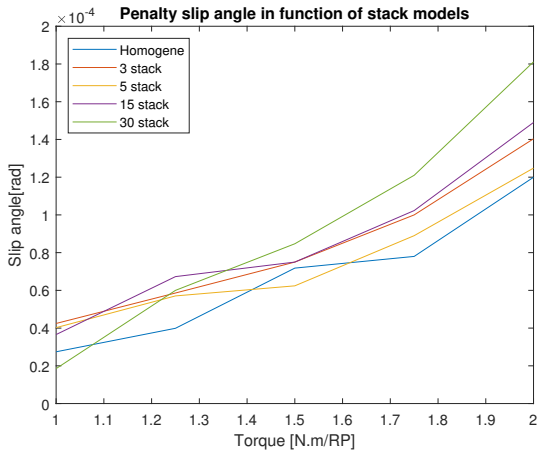

Figure 76: Slip angle for small sliding and different stack configurations

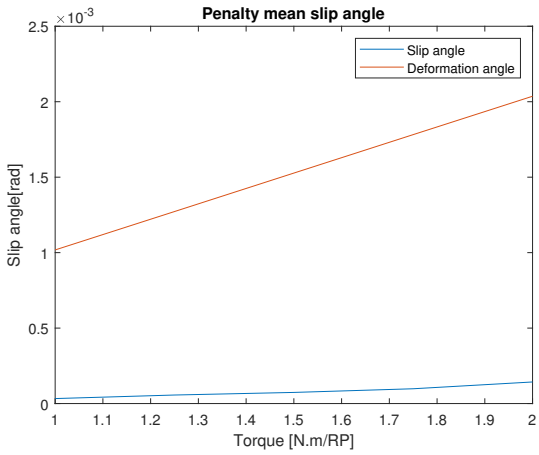

Figure 77: Mean slip angle compared to the deformation angle

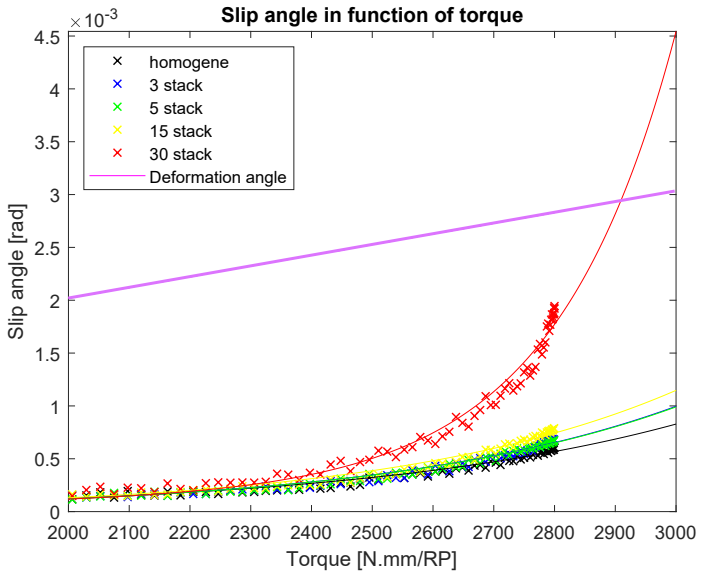

Figure 78: Slip angle of the different stacking configurations, with respect to the deformation angle.

As shown in figure 78, when we further increase the torque, the slip angle grows exponentially, while the solid deformation still grows linearly, following the linear relation :

$$\frac{\Delta\theta}{\Delta T} = \frac{L}{JG} \approx 10^{-3} \tag{38}$$

The slip angle has been curve-fitted in fig. 78 with an exponential function in order to visualize the evolution of the slip angle with the torque application.

We can also notice that the slip angle is steady below a certain value of torque for each models. The maximum shear transmission is reached in the first place for the 30-stack model, while the other model are still in the transient region. We can notice that the advancement state of the slip in the transient region is decreasing with the number of stack. This supposes a higher tendency to enter the slip region for the higher stacking numbers. The explanation given for this phenomena, is the uneven distribution of the normal force by the compressor ring. Indeed, as seen in figure 75, the slip occurs in the second plate for the 30-15 stack models instead of the first plate which is in contact with the compressor. This is explained by the fact that the normal force distribution is more dense on the edges of the first plate, due to the bending of the compressor. This results in a higher sticking on the edges which generate a higher shear transmission limit, since the major part of the normal force is far from the center of the plate. For the second plate, the normal force is smoothed by the intermediate plate and is therefore more evenly distributed. The normal force close to the center as a weaker effect on the torsional twist resistance. Thus, the second plate is more likely to be the first to enter in the slip region. For the lower stack number, since the accumulated torque is not enough when the second interface is encountered, it still the first interface with the compressor that slips. These are presumptions and haven't been extensively investigated since the slip is not supposed to happen inside the magnetic gear.

6.5 Radial bending

The ferromagnetic poles can be constrained to axial moments during the operation of the magnetic gear. In the previous section, we have seen that thanks to the normal force, the friction at the interfaces could transmit the shear stress in a way that the laminated models, could be approximated to equivalent homogeneous beams. One exception remains tho, the breaking point between the sticking and the sliding regions are smaller for the high laminate numbers.

The ferromagnetic plots also experience pure shear constraints, that can be dissociated into a radial and a tangential components. These two force components have previously computed by V. Kluyskens(cfr. Maxwell Stress Tensor). The models have been tested at the peak values in order to evaluate the radial and tangential distortions.

The radial distortion is of vital importance for several reasons. The first one is because the air-gap between the PM rotors and the modulating ring is small ($1.5[mm]$), and thus the rotors could enter in contact with the modulating ring, which would cause damage and wear. The second is because when air-gap closes between the ferromagnetic pieces and the modulating ring, the attraction force rises even further due to the increasing permeance. This results then in higher bending, and a higher attracting force again, causing a vicious cycle.

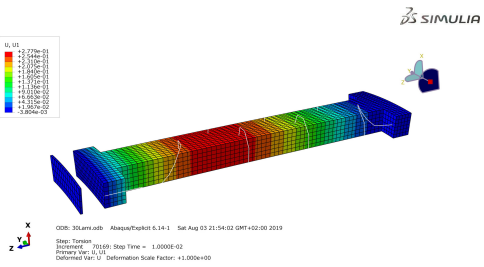

Figure 79: Radial distortion, $F_r = 943.26[N]$

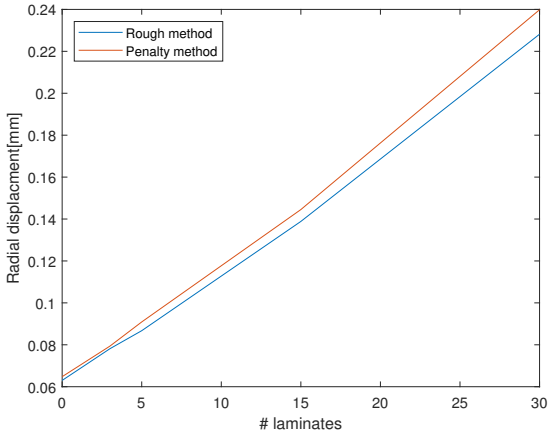

Figure 80: Radial displacement differences between the different stacking sequences.

$\#laminates$	1	3	5	15	30
$\Delta x_{r,max}$ (Rough)$[\mu m]$	63.3	78.12	86.73	138.85	228.72
$\Delta x_{r,max}$ (Penalty)$[\mu m]$	64.79	79.36	90.9	144.45	239.84

Table 17: Maximum radial displacement (peak-to-peak mean)

Beam theory's prediction :

$$\Delta x_r = \frac{F_r L^3}{384.E.I_r} = 11.84[\mu m] \tag{39}$$

In the above figures, we can notice the linear relation between the number of stacks and the maximum radial displacement. For the torsional twist, the same linear relation appeared in the first place, but with the hypothesis of infinite friction coefficients, and the exceeding torsional twist error could be extracted from the rough method. In this particular case, the hypothesis cannot be applied again to extract the error. An other explication can be found in the fact that the length of top half, grows when the beam is bent, while the lower half length decreases. In other words, the top half is in tension, while the bottom half is in compression.

The part that is in compression doesn't change with the introduction of laminated segments, since the compression stress is transmitted through the interface. But the tension in the upper part, cannot be transmitted efficiently by the laminated segments, the interfaces would separate from each other.

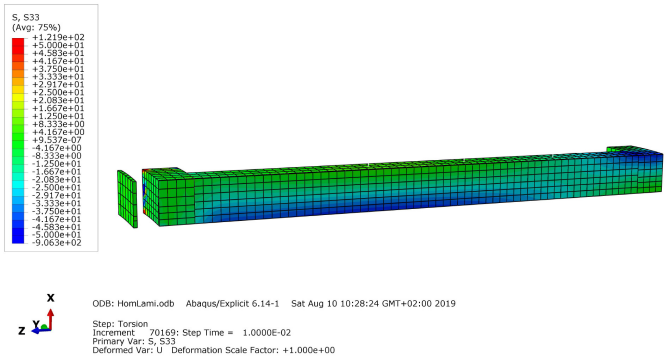

Figure 81: Side-cut of the normal stress distribution for a radial distortion, homogeneous beam.

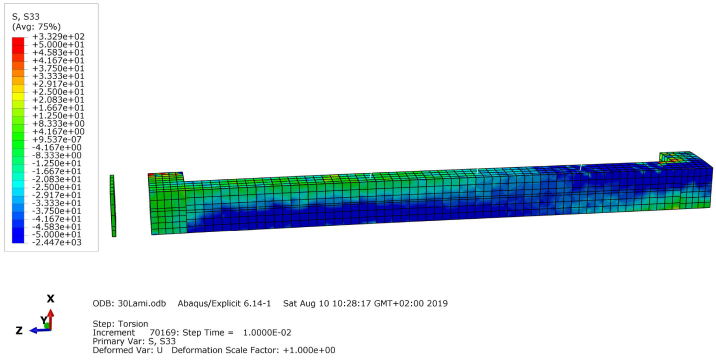

Figure 82: Side-cut of the normal stress distribution for a radial distortion, 30 stacks beam.

This phenomenon is depicted in figures 81-82, in which we can observe the normal stress transmission for the homogeneous and the 30 stacks beam. For the homogeneous beam, the normal stress is continuously transmitted both for the lower part(negative values of the normal stress), and the upper part(positive values of normal stress). The 30-stacks beams shows in the opposite a non continuous distribution of the normal stress, which is mainly noticeable for the positive values of the normal stress. This explains the lower performances of the laminated beams for radial distortions.

Lastly, we can also compare the results with the predicted radial deformation from the beam theory (eq. 39), which is also used in [7]. We can notice the important difference between the FEM of the complete model, and the hypothetical ideal case. This difference of results, takes it's origin from many small differences. But with no doubts the main source is from the fact that instead of being encastred at both ends the beam is compressed between two rings. Thus, the compression also induces a buckling effect, which further extends the bending. Besides, the ring itself also experiment deformation.

6.6 Tangential bending

As for the radial distortion, the tangential displacement is subject to the same phenomena. This results in a higher tangential displacement for increased number of laminates, since the

tension cannot be transmitted as efficiently as with the homogeneous beam. The results are equivalent and are depicted in figures 83 and 84.

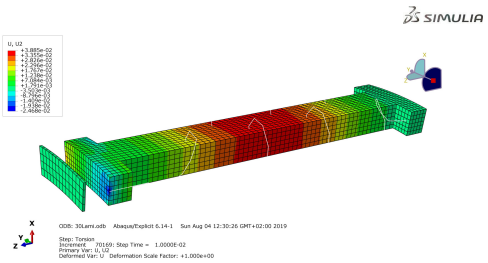

Figure 83: Tangential distortion, $F_\theta = 1344[N]$

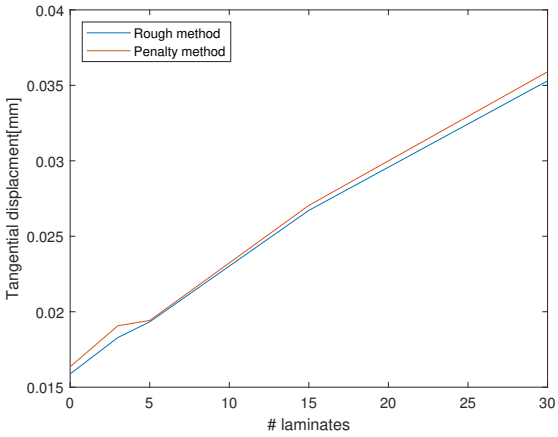

Figure 84: Tangential displacement difference between the several stacking sequence.

$\#laminates$	1	3	5	15	30
$\Delta x_{\theta,max}$ (Rough)$[\mu m]$	15.88	18.29	19.33	26.715	35.3
$\Delta x_{\theta,max}$ (Penalty)$[\mu m]$	16.36	19.07	19.42	27.05	35.9

Table 18: Maximum tangential displacement (peak-to-peak mean)

Beam theory's prediction :

$$\Delta x_\theta = \frac{F_\theta L^3}{384.E.I_\theta} = 6.72[\mu m] \tag{40}$$

We can notice int the first place, that even if the tangential component of the force is more important than the radial one, the maximum displacement is lower because of the quadratic momentum that is higher in the tangential direction. Also, as for the radial displacement, the prediction from the beam theory is lower than the numerical experiment.

From the above results, we can draw the ascertainment, that the simple beam theory is not sufficient to predict the radial and tangential deformation of the laminated modulating ring. Indeed, important increases of bending deformation has been experimented for higher number of stack. Even if the relation between the radial distortion and the stacking sequence seems to have a linear correlation, no strong affirmation can be drawn to predict the general influence of the stacking. Indeed, different section should be tested, with a higher number a stack, in order to isolate the single effect of the stacking.

6.7 Optimization structures

This section presents a comparison between 3 already well known supporting structures for the ferromagnetic pole-pieces. These structures are depicted in figures 85, 86 and 87.

Each model also refers to a configuration evaluated in the morphological diagram (table 3). The first one is a inner bridge linking the ferromagnetic pole-pieces. The bridge is of relatively important thickness of 3[mm]. The choice may be disproportionate, but the thickness as been chosen large, since the PBC's are only applied on a small number of points on both sides. Thus the constraints supported by the bridge is not evenly taken, and is compensated by increasing the thickness and thus the rigidity. This might inflate the performances and surely is a questionable method. But it's purpose is solely to compare the different solutions and give an idea of the performance differences. The "simple" model, refers to the homogeneous beam that was present in the previous sections. The goal being to show the potential improvements brought by the strengthening structures, the benefits will therefore be comparable and independent from the chosen stacking sequence. This motivates the simplest choice. The radial and tangential deformations presented important oscillations due to the bouncing effect (fig . 89-90). The oscillation is assumed to stabilize around the final value. The final values are then assumed to be the mean of the two last peaks of the oscillations. To help visualization, polynomial curve fitting has also been computed.

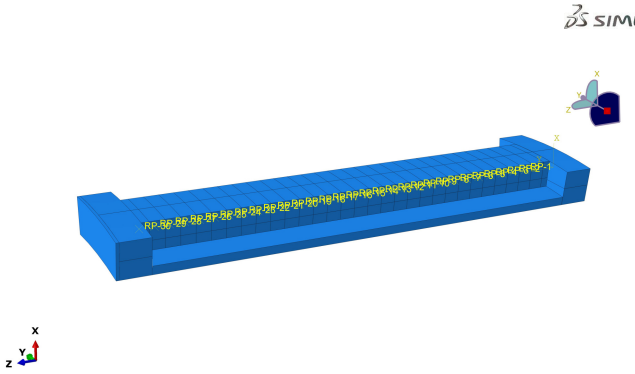

Figure 85: Ferromagnetic plot with an inner bridge(model 3)

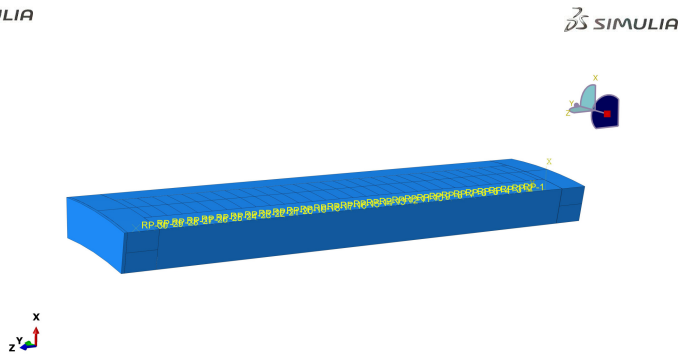

Figure 86: Ferromagnetic plot with a resin molded housing(model 5)

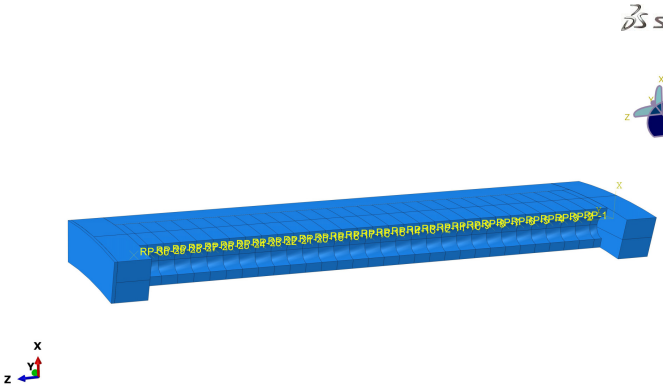

Figure 87: Grooved ferromagnetic plot with a resin molded housing(model 9)

6.7.1 Torsional twist

The method of evaluation method is the same as the previous sections. The first test is a torsion of the beam with a rated torque of $T = 2.8[N.m/RP]$. The total torque is then $84[N.m]$.

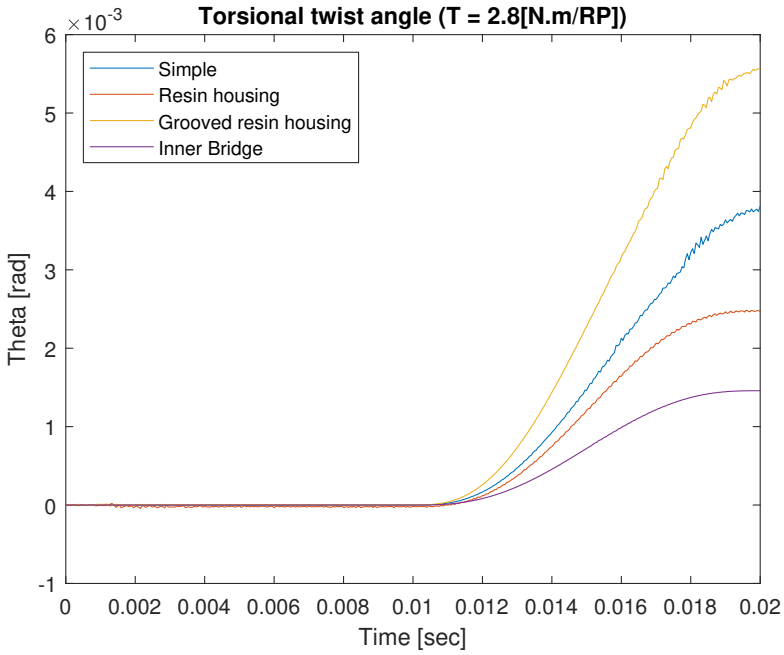

Figure 88: Torsional twit angle for different structure optimization's

	Simple	Resin housing	Grooved	Inner bridge
$\Delta\theta_{max}$ $[rad.10^{-3}]$	3.381	2.4645	5.553	1.458

Table 19: Maximum torsional twist angle

The results show an important improvement for the resin housing and the linking bridge. However, the grooved section experience a decrease of rigidity. This is from the decrease of the inertia moment, which is not compensated by the epoxy resin.

6.7.2 Radial distortion

The radial distortion is measured with a total radial force of 943.262[N], which is the obtained force by the integration of the Maxwell Stress Tensor on the ferromagnetic section.

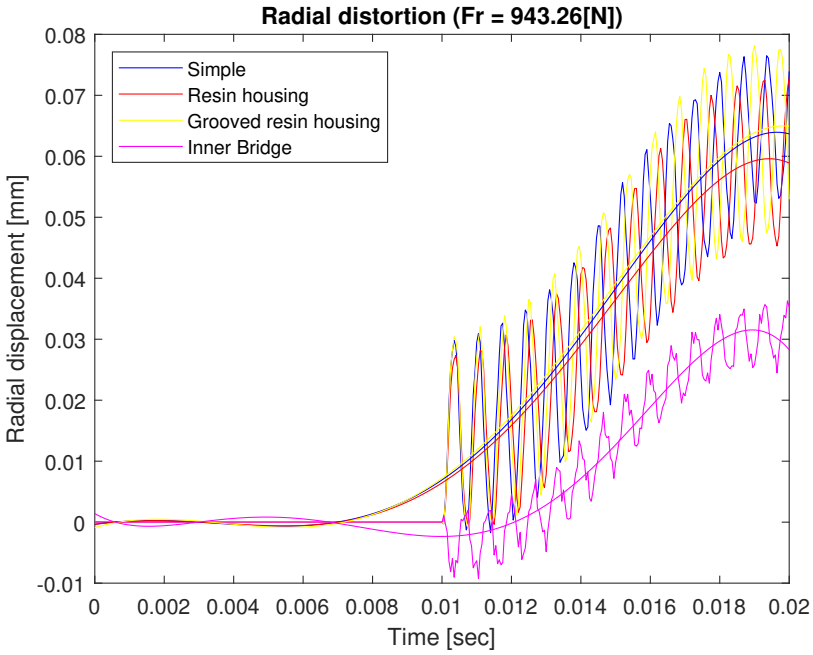

Figure 89: Radial displacement for different structure optimization's

	Simple	Resin housing	Grooved	Inner bridge
$\Delta x_{r,max}$ $[\mu m]$	64.79	59.09	62.89	29.85

Table 20: Radial maximum displacement (peak-to-peak mean)

Here, we can see that has we could expect, the resin housing shows limited benefits in order to maintain the ferromagnetic pole. Indeed, the gain is less than 10%. This might be considered since the epoxy housing increases the weight of the total structure. The grooved housing shows a better performance than for the torsional twist. This is due to the fact that the groove retain the plots in the radial direction. Therefore, it seems evident that the performances of the grooved resin housing is noticeable only for the radial distortions. The bridge shows again the best performances.

6.7.3 Tangential distortion

The tangential displacement is measured with a total tangential force of $1344,2[N]$. which is also the maximum force applied on the ferromagnetic during one full revolution of the rotors.

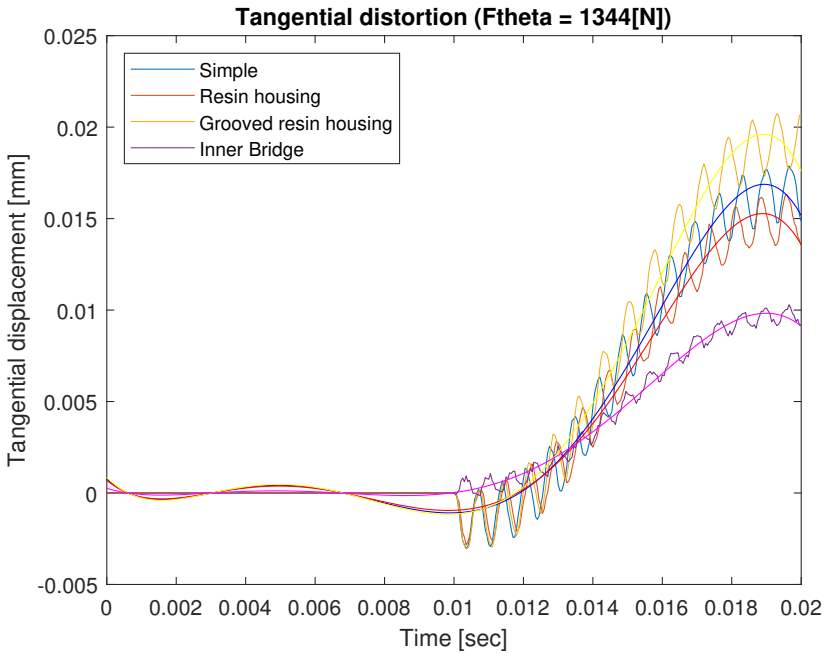

Figure 90: Tangential displacement for different structure optimization's

	Simple	Resin housing	Grooved	Inner bridge
$\Delta x_{\theta,max}$ $[\mu m]$	16.36	14.91	18.89	9.61

Table 21: Tangential maximum displacement (peak-to-peak mean)

The results are similar to the radial displacement, with the exception of the grooved resin housing. The performances fall again since the groove is only supporting the radial efforts.

6.7.4 Summary of the optimized structures

	$\Delta\theta_{max}$ $[rad.10^{-3}]$	$\Delta x_{r,max}$ $[\mu m]$	$\Delta x_{\theta,max}$ $[\mu m]$
Simple	3.381	64.79	16.36
Resin housing	2.464(-27.12%)	59.09(-8.79%)	14.91(-8.86%)
Grooved	5.553$(+64.24\%)$	62.89(-2.93%)	18.89$(+15.49\%)$
Inner bridge	1.458(-56.87%)	29.85 (-53.92%)	9.61(-41.25%)

Table 22: Optimization summary

7 Conclusion and further recommendations

7.1 Results summary

This thesis has investigated the structural resistance of the laminated ferromagnetic structures. The first ascertainment that comes out from these researches, is that as predicted, the beam equivalent theory is valid for torsional efforts, as long as the contact pressure is enough to insure no/small slips inside the model. This was approved by comparing a completely homogeneous beam and the equivalent beams composed by gradually increased number of sections.

Secondly, we have observed, that under radial or tangential forces, the laminated beams showed import differences with the homogeneous one. Indeed, the laminated sections cannot transmit tension efforts during the bending operation, which decreases the opposing force and thus increases the maximum displacement in the middle of the ferromagnetic pole. The prediction of the displacement cannot be reasonably predicted by conventional analytic beam theories.

Lastly, some supporting mechanism that are already widely accepted and implemented in the scientific community, have been implemented in order to evaluate the consequences over the general resistance of the structure. The results have shown that resin housing, had noticeable effect on the torsional twist (-27.12%), but had less impact over the radial and tangential displacements(-8.79%). The grooved laminated pole pieces have shown important decrease in the total rigidity especially for the torsional twist. This is due to the diminution of the quadratic moment in the equivalent beam, this reduction of the quadratic momentum could not be compensated by conventional epoxy resin in the exception of the radial displacement (for which the groove is dedicated for). The inner bridge showed the best overall performances, since it decreased the torsional twist and the radial displacement of more then 50%.

7.2 Limitations of the Results

The complexity of the structure, in term of the number of laminates and interfaces, the limited features offered by the FEM software interface and the difficulties to implement it manually, constrained the model to take many important hypothesis and simplifications that might be discussed. The assumptions that were made and that are believed to limit the accuracy of the present work are the following:

(1) The number of laminates. The number of laminates that could reasonably be achieved by hand was limited to only one tenth of the actual number of 300 in the application. Even if the behavior of the equivalent beam is shown to be independent of the number of laminates for the static torsional effort, this was not the case the for the radial and tangential bendings. The linear increase of the radial displacement makes sense since the tensile stress transmission capability of the equivalent beam decreases with the number of laminates. However, in the opposite of the torsional stress, the level of numerical errors due to the normal specifications of the contact could not be evaluated. This is why further experiments should be leaded in order to confirm this ascertainment.

In the annex B, is presented the last model that was implemented in this thesis, this time

with 150 laminates. However, with the time missing to finish the implementation of this last model, the trials have been aborted. This could be carried on in future works.

(2) The torque distribution was discretized, since no constant torque field could be applied through the Abaqus interface. This surely leaded to additional errors with higher deformations at the point of applications and lower everywhere else. With the present interface, no real solutions are believed to exist to resolve this problem. Maybe changing directly the core code could bring a good alternative to compensate the lack of features in the interface .

(3) The contact parameters selected, especially for the normal behavior, were based on trials results and some advises, not on tangible theory or numerical method. Thus the optimal normal behavior of the actual model, might be different of the chosen one.

(4) The boundary conditions. The periodic boundary conditions for surfaces being unavailable in the interface, the PBC's have been implemented by the means equations constraints that were located on a restricted number of points. This implies that on the other points of the limit surfaces, the nodes where free of boundary conditions and thus leads to unwanted displacements. This phenomena was especially visible for the optimized resin housing, for which the deformations elsewhere of the PBC's applications where noticeable. Therefore, a better way to implement the periodic boundary conditions is required to obtain more accurate results. The limitations of the PBC motivated the choice of increasing the thickness of the inner bridge in the optimized models. This choice is also not based on actual measurements.

(5) The compressor ring. The compressor ring was made of steel, which is of course, not acceptable for magnetic gears. The high permittivity of the steel would lead to severe end-effects and therefore is to prohibit. Thus, a substitute material is to be found with a sufficient rigidity to be able to apply the targeted contact pressure without yielding. The dimensions as well were selected with a common sense, not based on a real evaluation. Therefore, the dimensions of compressor ring must also be evaluated for the wanted constraints.

(6) The normal force influence. Since the relation between the shear stress transmission capability and the applied normal force on the laminated stack is linear, the evolution of the results with respect to the normal force have not been investigated. However, in order to fully understand the behavior of the axially laminated beam, the normal force's influence over the dynamic behavior might be verified as well.

(7) The mesh. The influence of the mesh over the results as not been studied. The meshing parameters have been selected following the good advises of the PhD student Colin Laville. However, the influence of the dimensions of the mesh have not been investigated and might find some differences.

(8) The slip rate. Even if the importance of this one parameter was not fundamental for the present work, the slip rate that was left on default settings, could have been modified adjusted according to the physics of the problem.

7.3 Recommendations

Knowing the potential effect of the air-gap length over the magnetic gear performances, important caution should be given to the implementation of the modulating ring. In this thesis the increase of radial displacement for the increments of laminate number have shown a linear form. However, this might not characterize precisely enough the behavior for the real

number of laminate which rises up to 300 for the wanted prototype. Following the results, the radial displacement of 300 stacks under the same constraint should be around $2[mm]$, which is very high and more than the air-gap length. A model composed of 150 laminates has been created, but the time to test and compare it with the other models missed. This last model results could bring confirmation of the precedent results.

The final idea on which this thesis ends up, is that the modulating ring configuration is a compromise between the magnetic performances and the structural performance, which affects the magnetic performances in return. Therefore, the expected torque capability and the force that acts on the ferromagnetic poles must be taken into account in order to find the optimal combination between the magnetic circuit and the structural strength.

References

[1] S.D Calverley K.Atallah and D.Howe. Design, analysis and realisation of a highperformance magnetic gear. *Journal of magnetism and magnetic materials*, 2001.

[2] C. G. Armstrong. Power transmitting device. *U.S Patent letter*, 1901.

[3] Yi-Chang Wu and Bo-Syuan Jian. Magnetic field analysis of a coaxial magnetic gear mechanism by two-dimnesional equivalent magnetic circuit network method and finite element method. *Applied mathematical modelling*, 2014.

[4] H.T Faus. Magnet gearing. *U.S Patent 2 243 555*, 1941.

[5] K.Tsuruinoto and S.Kikuchi. A new magnetic gear using permanent magnet. *IEEE TRANSACTIONS ON MAGNETICS*, 1980.

[6] S.D Calverley K.Atallah and D.Howe. High performance magnetic gears. *Journal of magnetism and magnetic materials*, 2003.

[7] S. Gerber P.M. Tlali, R-J. Wang. Magnetic gear technologies: A review. *IEEE*, 2014.

[8] R-J. Wang S. Gerber. Analysis of the end-effects in magnetic gears and magnetically geared machines. *IEEE*, 2014.

[9] Nicolas W. Frank and Hamid A.Toliyat. Analysis of the concentric planetary magnetic gear strengthened stator and interior permanent magnet inner rotor. *IEEE Transactions on industry apllications, Vol.47*, 2011.

[10] F.T. Joergensen Rasmussen, T.O. Andersen. Development of a high performance magnetic gear. *IEEE review*, 2003.

[11] Yu Gong J. Z. Jiang Chuang Yu Linni Jian, K. T. Chau and Wenlong Li. Comparison of coaxial magnetic gears with different topologies. *IEEE transactions on magnetics*, 2009.

[12] David Barnett Ho Yin Wong, Jonathan Z.Bird and Wesley Williams. A high order density halbach rotor coaxial magnetic gear. *Electrical and computer engineering faculty, publications and presentations*, 2019.

[13] Linni Jian and K. T. Chau. A coaxial magnetic gear with halbach permanent-magnet arrays. *IEEE, Transactions on Energy Conversion*, 2010.

[14] He Hao Meng-Jia Jin Yun-Chong Wang Jian-Xin Shen, Hua-Yang Li. A coaxial magnetic gear with consequent-pole rotors. *IEEE, Transactions on Energy Conversion*, 2016.

[15] He Hao Meng-Jia Jin Yun-Chong Wang Jian-Xin Shen, Hua-Yang Li. Topologies and performance study of a variety of coaxial magnetic gears. *IEEE, Electric Power Applications*, 2017.

[16] W. N. Fu and Longnv Li. Optimal design of magnetic gears with a general pattern of permanent magnet arrangement. *IEEE, Transaction on Applied Superconductivity*, 2016.

[17] Piergiogio Alotto Mattia Filippini. Coaxial magnetic gears design and optimization. *IEEE transactions on industrial electronics*, 2017.

[18] J. Wright* J. Pitchard-W. Williams K. K. Uppalapati*, M. Calvin†. A magnetic gearbox with an active region torque density of 239nm/l. *IEEE, Transactions on Industry Applications*, 2017.

[19] Kosuke Nagaya Masaru Oka Takashi Todaka Masato Enokizono-Kazunobu Sugiura Tomoyuki Fujita, Yoshinori Ando. Surface magnet gears with a new magnet arrangement and optimal shape of stationary pole pieces. *Journal of Electromagnetic Analaysis and Applications*, 2013.

[20] D.Z. Abdelhamid and A.M. Knight. The effect of modulating ring design on magnetic gear torque. *IEEE, Transactions on Industry Applications*, 2017.

[21] Kosuke Nagaya Masaru Oka Takashi Todaka Masato Enokizono-Kazunobu Sugiura Tomoyuki Fujita, Yoshinori Ando. Surgace magnet gears with a new magnet arrangement and optimal shape of stationary pole pieces. *Journal of Electromagnetic Analysis and Application, 2013, 243-249*, 2013.

[22] Kiran K. Uppalapati and Jonathan Z. Bird. An iterative magnetomechanical deflection model for a magnetic gear. *IEEE, Transaction on Magnetics*, 2014.

[23] Xiaoyu Li and Dashin Liu. Generalized laminate theories based on double superposition hypothesis. *Internaltional Journal for Numerical Methods in Engineering*, 1997.

[24] R. Akkerman. On the properties of quasi-isotropic laminates. *Composites*, 2001.

[25] S.R. Mohebpour M.H. Kadivar. Finite element dynamic analysis of unsymmetric composite laminated beams with shear effect and rotary inertia under the action of moving loads. *Elsevier, Finite Element in analysis and design*, 1998.

[26] Yuwaraj M. Ghugal and Atteshamuddin S. Sayyad. Stress analysis of thick laminated plates using trigonometric shear deformation theory. *International Journal of Applied Mechanics*, 2013.

[27] Yan-ting Ai Yun-dong Sha Song Xiang, Ke-ming Wang and Hong Shi. Analysis of isotropic, sandwich and laminated plates by a meshless method and various shear deformation. *Elsevier, Composite structures*, 2009.

[28] J.Y. Kim and C.S. Hong. Three dimensional finite element analysis of interlaminar stresses in thick composite laminates. *Computers and Structures*, 1990.

[29] x. Martinez A. Solis, S. Sanchez-Saes and E. Barbero-Pozuelo. Numerical analysis of interlaminar stresses in open-hole laminates under compression. *Elsevier, Composite Structures*, 2019.

[30] N.J Pagano. On the calculation of interlaminar normal stresse in composite laminate. *Journal of Composite Materials*, 1973.

[31] Vijay K. Goyal and Rkesh K. Kapania. A shear-deformable beam element for the analysis of laminated composites. *Elsevier, Finite Elements in Analysis and Design*, 2007.

[32] Theofanis S. Pagianakos and Dimitris A. Saravanos. Higher-order layerwise theory for the prediction of interlaminar shear stresses in thick composite and sandwich plates. *Elsevier, Composite structures*, 2008.

[33] T. Kant and K. Swaminathan. Free vibration of isotropic, orthotropic and multilayer plates based on higher order refined theories. *Journal of sound and Vibrations*, 2000.

[34] J. N. Reddy. A simple higher-order theory for laminated composite plates. *Journal of Applied Mechanics*, 1984.

[35] Hong-Ji Chen and Stephen W.Tsai. Three-dimensional effective moduli. *Journal of Composite Materials*, 1995.

[36] E. O. Ayorinde.

[37] Hisao Fukunga. On isotropic laminate configurations. *Journal of Composite Materials*, 1989.

[38] Kuang M. Wuu and Brian L. Avery. Fully isotropic laminates and quasi-homogeneous anisotropic laminates. *Journal of Composite Materials*, 1991.

[39] M. Grimsditch. Effective elastic constants of superlattices. *Material Science and Technology Division, Argonne National Laboratory*, 1984.

[40] C.T Sun and W.C. Liao. Analysis of thick section composite laminates using effective moduli. *Journal of Composite Materials*, 1990.

[41] Evgeniæi Zalmanovich. Grigoriev, Igor S. Meæilikhov. *Handbook of physical quantities*. Boca Raton : CRC Press, QC61 .H36 1997, 1997.

[42] E. A. Lomonova K. J. Meesen, J. J. H. Paulides. Force calculation in 3d cylindrical stuctures using fourrier analysis and the maxwell stess tensor. *Eindhoven University of Technology*, 2011.

A Comsol designs

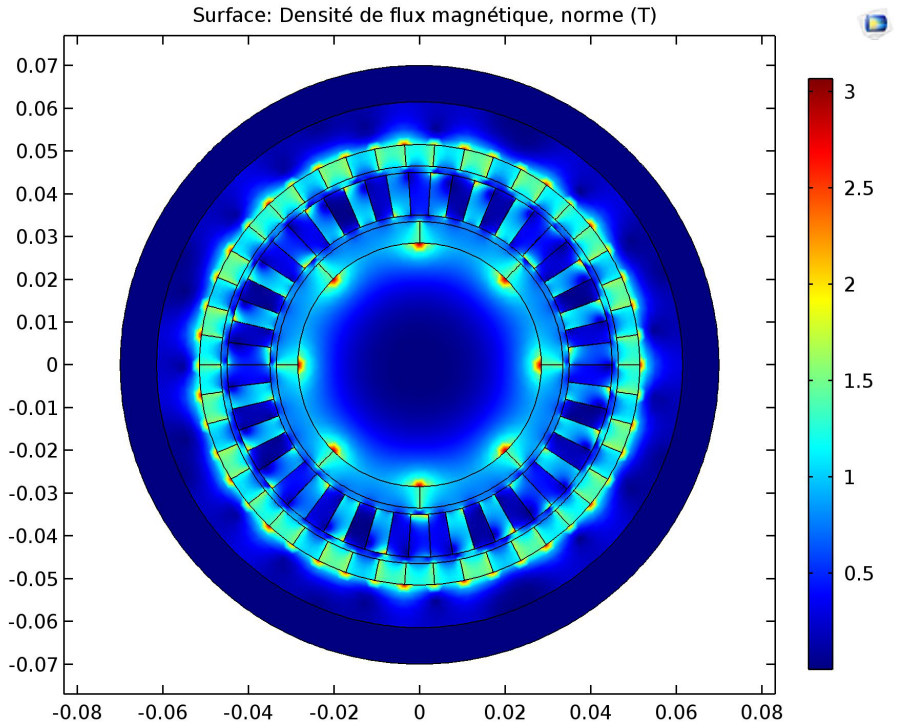

Figure 91: Magnetic flux density, magnetic gear with parametric geometry

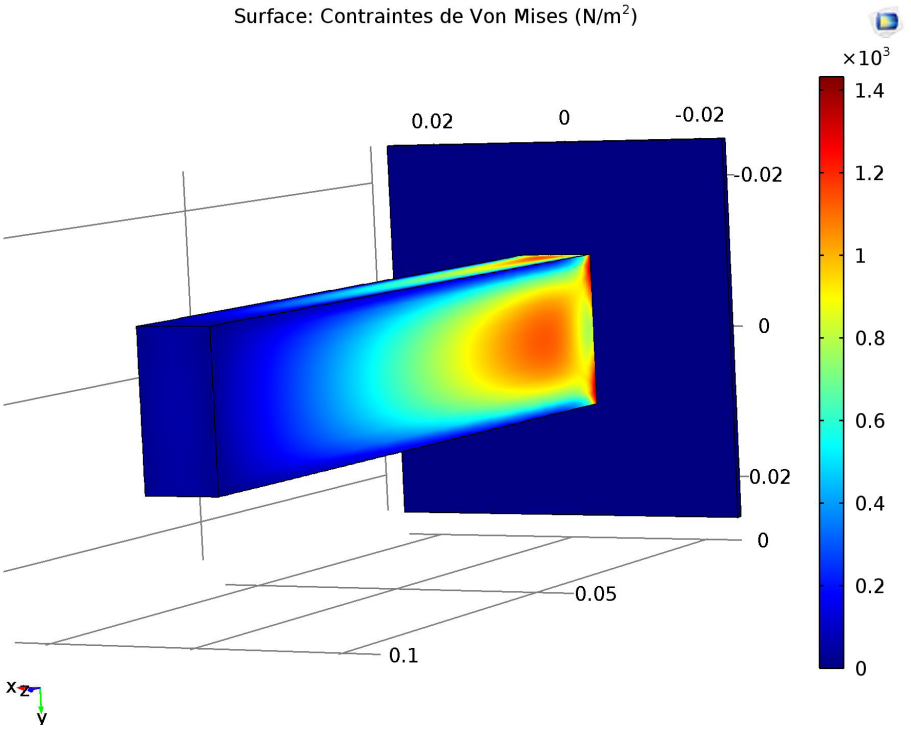

Figure 92: One homogeneous pole torsion

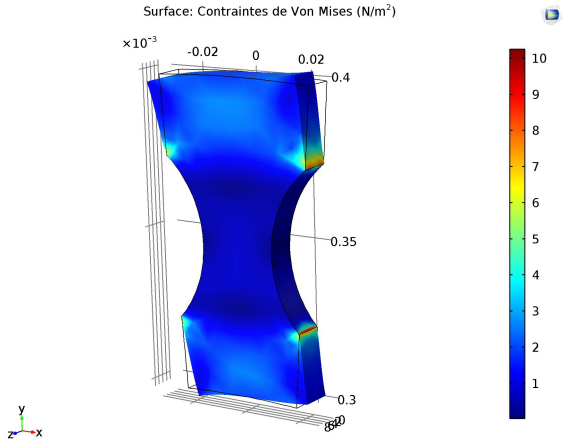

Figure 93: One grooved steel sheet torsion

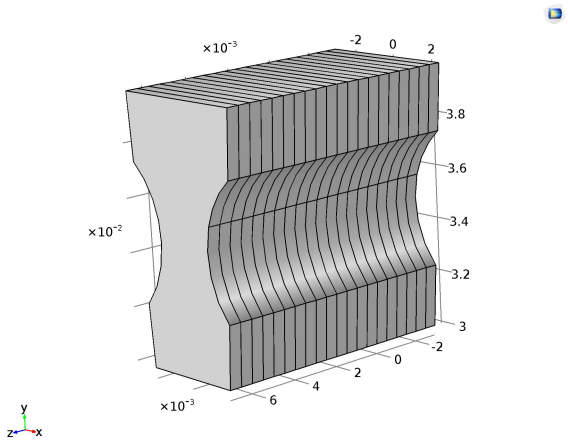

Figure 94: Staking of grooved steel sheets

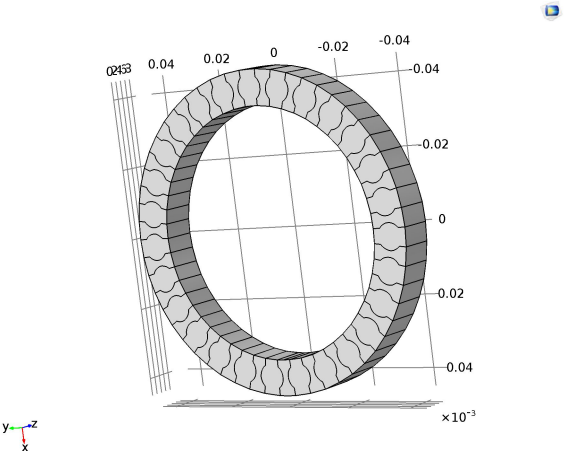

Figure 95: Full revolution section of a grooved modulating ring

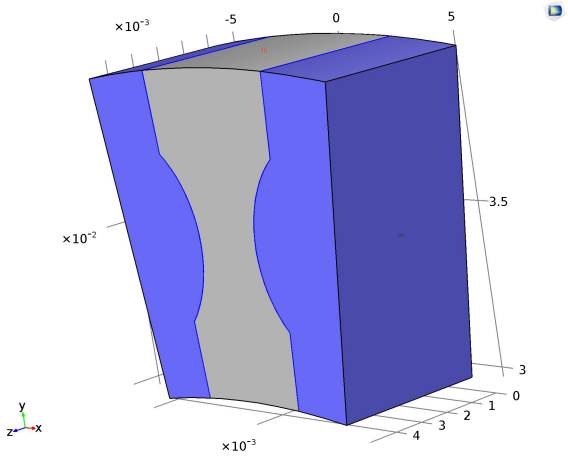

Figure 96: One pole pitch section of the grooved modulating ring

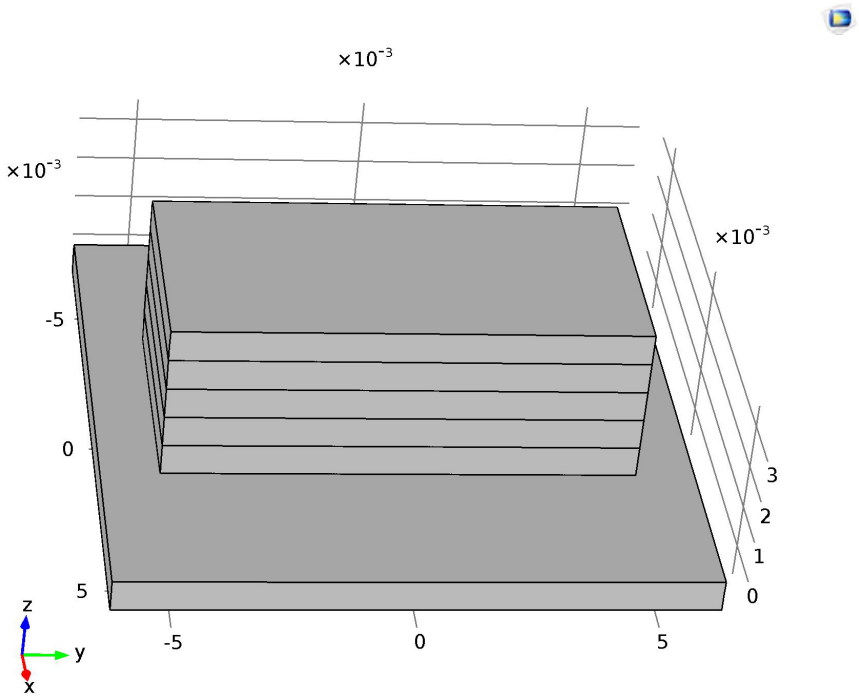

Figure 97: Stacking of simple rectangular plates

B Preliminary Abaqus designs

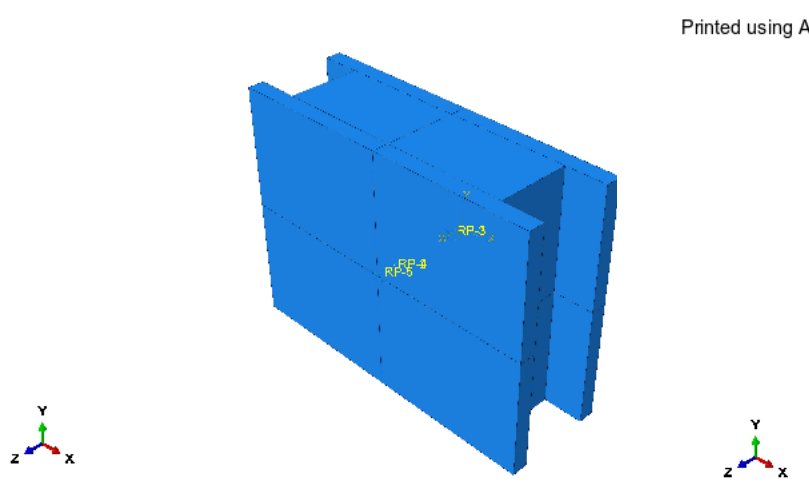

Figure 98: One squared plate

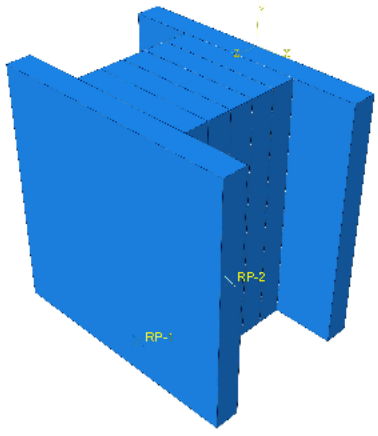

Figure 99: 5 laminated sections

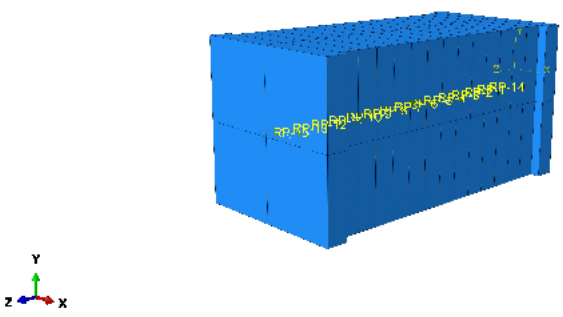

Figure 100: 10 laminated sections

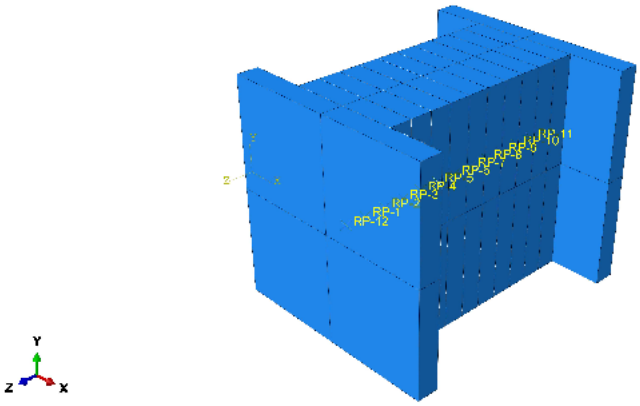

Figure 101: 10 laminated sections

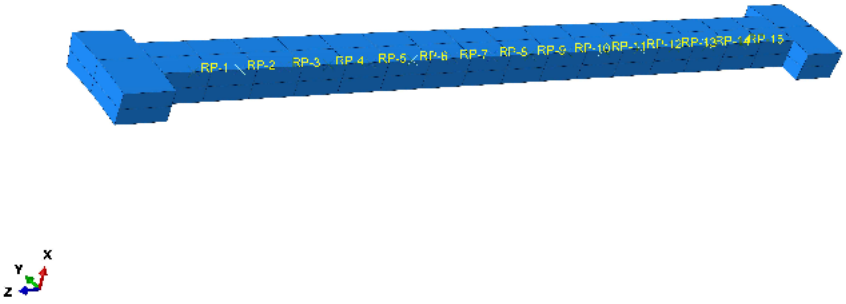

Figure 102: Equivalent beam subdivision

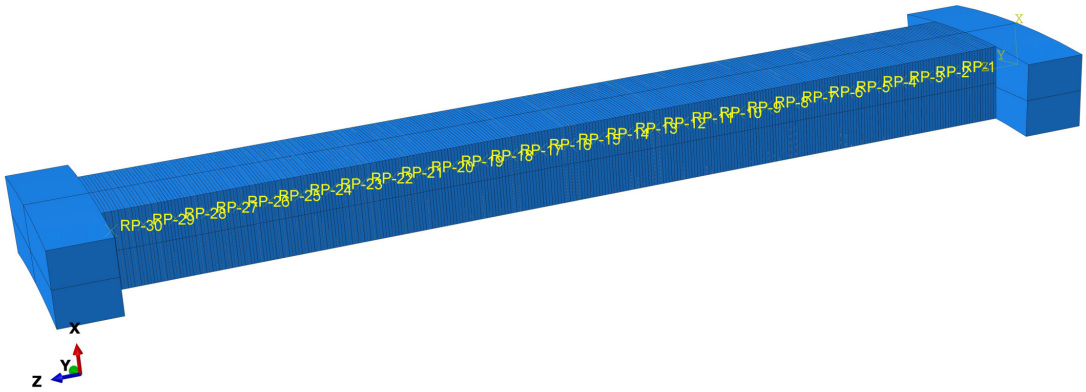

Figure 103: 150 stack model

C Equivalent Elastic Constants

```
% Lamina dimensions

l = 0.02 %length[m]
w = 0.01 %width[m]
tk = 0.001 %thickness[m]
h = 0.1 %height[m]
Nl = h/tk - mod(h,tk); %Number of layers[#]

vk = tk/h*ones(Nl,1);

% Material properties

% Iron

E = 211e9 %Young's modulus[Pa]
mu = 0.29 %Poisson's ratio[-]
G = 82e9 %Shear modulus [Pa]



% Layerwise elastic moduli
sa = 1/E;
sb = -mu/E;
sc = (1+mu)/E;
```

```
sk = [sa sb sb 0 0 0; sb sa sb 0 0 0 ; sb sb sa 0 0 0 ; 0 0 0 sc 0
    0 ; 0 0 0 0 sc 0; 0 0 0 0 0 sc];

ck = inv(sk)

deltak = ck(4,4)*ck(5,5)-(ck(4,5))^2
delta = (sum(ck(4,4).*vk./deltak))*(sum(ck(5,5).*vk./deltak))-(sum
   (ck(4,5).*vk./deltak))^2



%Effective Elastic moduli for thick lamina



c33 = 1/(sum(vk./ck(3,3)))
lambda33 = c33;
c13 = (sum(ck(1,3).*vk))
lambda13 = c13;
c23 = (sum(ck(2,3).*vk))
lambda23 = c23;
c36 = (sum(ck(3,6).*vk))
lambda36 = c36;

c11 = (sum(ck(1,1).*vk))
c12 = (sum(ck(1,2).*vk))
c22 = (sum(ck(2,2).*vk))
c16 = (sum(ck(1,6).*vk))
c26 = (sum(ck(2,6).*vk))
c66 = (sum(ck(6,6).*vk))

c44 = (sum(ck(6,6).*vk./deltak))/delta
c45 = (sum(ck(4,5).*vk./deltak))/delta
c55 = (sum(ck(5,5).*vk./deltak))/delta



%c11 = (sum(ck(1,1).*vk)+(sum((ck(1,3).*vk)


Effective Elastic for layered media
C = zeros(6,6);
for i = [1 2 3 6]
    for j = [1 2 3 6]
        C(i,j) = sum(vk.*(ck(i,j) - ck(i,3)*ck(3,j)/ck(3,3) + ck(i
            ,3)*sum(vk.*ck(3,j))/(ck(3,3)*sum(vk./ck(3,3)))));
    end
```

```
end

for i = 1:1:Nl
    for j = 1:1:Nl
        K(i,j) = vk(i)*vk(j)*(ck(4,4)*ck(5,5)-ck(4,5)*ck(5,4))/(
            deltak^2);
    end
end
Sumk = sum(sum(K(1:1:Nl,1:1:Nl)))

for i = [4 5]
    for j = [4 5]
        C(i,j) = sum(vk./deltak.*ck(i,j))/Sumk;
    end
end

for i = [1 2 3 6]
    for j = [4 5]
        C(i,j) = 0;
    end
end
```

D Correction method

```
%Results : adapted load

n = [0,3,5,15,30];
nNorm=[3,5,15,30];
%T = 1.0[N.m/RP]
theta_penalty1 =  [1.0454,1.0775,1.1,1.2128,1.3416]*10^-3;
theta_rough1 = [1.01796,1.03504,1.05975,1.17622,1.32308]*10^-3;
theta_corr1 = theta_penalty1-(theta_rough1(1:1:5)-theta_rough1(1))
    ;
Standard1 = [theta_penalty1(2)-theta_penalty1(1),theta_penalty1(3)
    -theta_penalty1(1),theta_penalty1(4)-theta_penalty1(1),
    theta_penalty1(5)-theta_penalty1(1)];
Normalized1 = [Standard1(1),Standard1(2)/5*3,Standard1(3)/15*3,
    Standard1(4)/30*3];
%T = 1.25[N.m/RP]
theta_penalty125 =  [1.3122,1.351,1.37836,1.526,1.678]*10^-3;
theta_rough125 = [1.2723,1.2924,1.3213,1.45871,1.618]*10^-3;
theta_corr125 = theta_penalty125-(theta_rough125(1:1:5)-
    theta_rough125(1));
Standard125 = [theta_penalty125(2)-theta_penalty125(1),
    theta_penalty125(3)-theta_penalty125(1),theta_penalty125(4)-
    theta_penalty125(1),theta_penalty125(5)-theta_penalty125(1)];
```

```
Normalized125 = [Standard125(1),Standard125(2)/5*3,Standard125(3)
    /15*3,Standard125(4)/30*3];
%T = 1.5[N.m/RP]
theta_penalty15 =  [1.599,1.625,1.645,1.815,2.011]*10^-3;
theta_rough15= [1.5272,1.55,1.5826,1.74,1.9263]*10^-3;
theta_corr15 = theta_penalty15-(theta_rough15(1:1:5)-theta_rough15
    (1));
Standard15 = [theta_penalty15(2)-theta_penalty15(1),
    theta_penalty15(3)-theta_penalty15(1),theta_penalty15(4)-
    theta_penalty15(1),theta_penalty15(5)-theta_penalty15(1)];
Normalized15 = [Standard15(1),Standard15(2)/5*3,Standard15(3)
    /15*3,Standard15(4)/30*3];
%T = 1.75[N.m/RP]
theta_penalty175 =  [1.86,1.909,1.933,2.123,2.358]*10^-3;
theta_rough175= [1.782,1.809,1.844,2.0207,2.237]*10^-3;
theta_corr175 = theta_penalty175-(theta_rough175(1:1:5)-
    theta_rough175(1));
Standard175 = [theta_penalty175(2)-theta_penalty175(1),
    theta_penalty175(3)-theta_penalty175(1),theta_penalty175(4)-
    theta_penalty175(1),theta_penalty175(5)-theta_penalty175(1)];
Normalized175 = [Standard175(1),Standard175(2)/5*3,Standard175(3)
    /15*3,Standard175(4)/30*3];
%T = 2[N.m/RP]
theta_penalty2 =  [2.15625,2.20795,2.2288,2.45,2.72313]*10^-3;
theta_rough2= [2.0363,2.0676,2.104,2.301,2.542]*10^-3;
theta_corr2 = theta_penalty2-(theta_rough2(1:1:5)-theta_rough2(1))
    ;
Standard2 = [theta_penalty2(2)-theta_penalty2(1),theta_penalty2(3)
    -theta_penalty2(1),theta_penalty2(4)-theta_penalty2(1),
    theta_penalty2(5)-theta_penalty2(1)];
Normalized2 = [Standard2(1),Standard2(2)/5*3,Standard2(3)/15*3,
    Standard2(4)/30*3];

%Theta_#
T = [1,1.25,1.5,1.75,2];
thetapen_hom = [theta_penalty1(1),theta_penalty125(1),
    theta_penalty15(1),theta_penalty175(1),theta_penalty2(1)];
thetarou_hom = [theta_rough1(1),theta_rough125(1),theta_rough15(1)
    ,theta_rough175(1),theta_rough2(1)];
thetacorr_hom = [theta_corr1(1),theta_corr125(1),theta_corr15(1),
    theta_corr175(1),theta_corr2(1)];

thetapen_3 = [theta_penalty1(2),theta_penalty125(2),
    theta_penalty15(2),theta_penalty175(2),theta_penalty2(2)];
thetarou_3 = [theta_rough1(2),theta_rough125(2),theta_rough15(2),
    theta_rough175(2),theta_rough2(2)];
```

```
thetacorr_3 = [theta_corr1(2),theta_corr125(2),theta_corr15(2),
   theta_corr175(2),theta_corr2(2)];

thetapen_5 = [theta_penalty1(3),theta_penalty125(3),
   theta_penalty15(3),theta_penalty175(3),theta_penalty2(3)];
thetarou_5 = [theta_rough1(3),theta_rough125(3),theta_rough15(3),
   theta_rough175(3),theta_rough2(3)];
thetacorr_5 = [theta_corr1(3),theta_corr125(3),theta_corr15(3),
   theta_corr175(3),theta_corr2(3)];

thetapen_15 = [theta_penalty1(4),theta_penalty125(4),
   theta_penalty15(4),theta_penalty175(4),theta_penalty2(4)];
thetarou_15 = [theta_rough1(4),theta_rough125(4),theta_rough15(4),
   theta_rough175(4),theta_rough2(4)];
thetacorr_15 = [theta_corr1(4),theta_corr125(4),theta_corr15(4),
   theta_corr175(4),theta_corr2(4)];

thetapen_30 = [theta_penalty1(5),theta_penalty125(5),
   theta_penalty15(5),theta_penalty175(5),theta_penalty2(5)];
thetarou_30 = [theta_rough1(5),theta_rough125(5),theta_rough15(5),
   theta_rough175(5),theta_rough2(5)];
thetacorr_30 = [theta_corr1(5),theta_corr125(5),theta_corr15(5),
   theta_corr175(5),theta_corr2(5)];



Slip1 = mean(theta_penalty1)-mean(theta_rough1);
Slip125 = mean(theta_penalty125)-mean(theta_rough125);
Slip15 = mean(theta_penalty15)-mean(theta_rough15);
Slip175 = mean(theta_penalty175)-mean(theta_rough175);
Slip2 = mean(theta_penalty2)-mean(theta_rough2);

sliphom = [theta_penalty1(1) - theta_rough1(1),theta_penalty125(1)
    - theta_rough125(1),theta_penalty15(1) - theta_rough15(1),
   theta_penalty175(1) - theta_rough175(1),theta_penalty2(1) -
   theta_rough2(1)];
slip3 = [theta_penalty1(2) - theta_rough1(2),theta_penalty125(2) -
    theta_rough125(2),theta_penalty15(2) - theta_rough15(2),
   theta_penalty175(2) - theta_rough175(2),theta_penalty2(2) -
   theta_rough2(2)];
slip5 = [theta_penalty1(3) - theta_rough1(3),theta_penalty125(3) -
    theta_rough125(3),theta_penalty15(3) - theta_rough15(3),
   theta_penalty175(3) - theta_rough175(3),theta_penalty2(3) -
   theta_rough2(3)];
slip15 = [theta_penalty1(4) - theta_rough1(4),theta_penalty125(4)
   - theta_rough125(4),theta_penalty15(4) - theta_rough15(4),
   theta_penalty175(4) - theta_rough175(4),theta_penalty2(4) -
```

```
    theta_rough2(4)];
slip30 = [theta_penalty1(5) - theta_rough1(5),theta_penalty125(5)
    - theta_rough125(5),theta_penalty15(5) - theta_rough15(5),
    theta_penalty175(5) - theta_rough175(5),theta_penalty2(5) -
    theta_rough2(5)];

%analytical torsion angle
theta = 0.15*15*T/(3*8.3453*10^-9*82*10^9);

figure;
plot(T,[Slip1,Slip125,Slip15,Slip175,Slip2],T,[theta_rough1(1),
    theta_rough125(1),theta_rough15(1),theta_rough175(1),
    theta_rough2(1)],T,theta)
title('Penalty mean slip angle')
xlabel('Torque [N.m/RP]')
ylabel('Slip angle[rad]')
legend('Slip angle','Deformation angle')

figure;
plot(T,theta,T,sliphom,T,slip3,T,slip5,T,slip15,T,slip30)
title('Penalty slip angle in function of stack models')
xlabel('Torque [N.m/RP]')
ylabel('Slip angle[rad]')
legend('Homogene','3 stack','5 stack','15 stack','30 stack','
    location','northwest')

% figure;
% plot(n,theta_penalty15,n,theta_rough15,n,theta_corr15)
% title('Small torque : Correction method')
% xlabel('number of stack [#] ')
% ylabel('Theta [rad]')
% legend('Penalty method','Rough method','Corrected values')
% figure;
% plot(T,thetapen_hom,'rx-',T,thetarou_30,'bx-',T,thetapen_3,'rx
    -',T,thetapen_5,'rx-',T,thetapen_15,'rx-',T,thetapen_30,'rx-',T,
    thetarou_hom,'bx-',T,thetarou_3,'bx-',T,thetarou_5,'bx-',T,
    thetarou_15,'bx-',T,thetacorr_hom,'gx-',T,thetacorr_3,'gx-',T,
    thetacorr_5,'gx-',T,thetacorr_15,'gx-',T,thetacorr_30,'gx-')
% title(' Small torque : Penalty\Rough angle')
% xlabel('Torque [N.m/RP]')
% ylabel('Theta [rad]')
% legend('Penalty method','Rough method(mu = inf)')

figure;
plot(T,thetacorr_hom,T,thetacorr_3,T,thetacorr_5,T,thetacorr_15,T,
    thetacorr_30,T,theta)
title('Small torque twist angle (corrected method)')
```

```
xlabel('Torque [N.m/RP]')
ylabel('Theta [rad]')
legend('Homogene','3 stack','5 stack','15 stack','30 stack','
    location','northwest')

% figure;
% plot(n,theta_penalty1,'b-',n,theta_rough1,'r-',n,theta_corr1,'y
    -',n,theta_penalty125,'b-',n,theta_rough125,'r-',n,theta_corr125
    ,'y-',n,theta_penalty15,'b-',n,theta_rough15,'r-',n,theta_corr15
    ,'y-',n,theta_penalty175,'b-',n,theta_rough175,'r-',n,
    theta_corr175,'y-',n,theta_penalty2,'b-',n,theta_rough2,'r-',n,
    theta_corr2,'y-')
% title('Small torque : Correction method')
% xlabel('number of stack [#] ')
% ylabel('Theta [rad]')
% legend('Penalty method','Rough method','Corrected values','
    location','northwest')
```

UNIVERSITÉ CATHOLIQUE DE LOUVAIN
École polytechnique de Louvain
Rue Archimède, 1 bte L6.11.01, 1348 Louvain-la-Neuve, Belgique | **www.uclouvain.be/epl**